

國立交通大學  
電子工程學系 電子研究所  
碩士論文

單晶片電感模型研發及射頻積體電路  
模擬與設計方面之應用



**On-chip Inductor Model  
Development and Applications in RF CMOS  
Circuit Simulation and Design**

研究生：譚登陽

指導教授：郭治群 博士

中華民國九十五年八月

單晶片電感模型研發及射頻積體電路  
模擬與設計方面之應用

**On-chip Inductor Model**

**Development and Applications in RF CMOS**

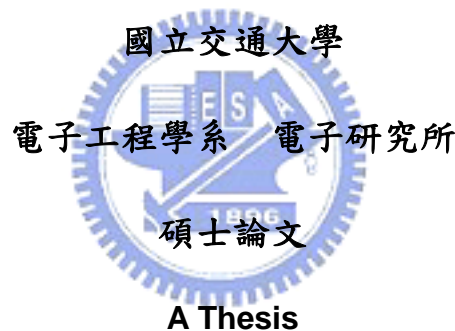
**Circuit Simulation and Design**

研究生：譚登陽

指導教授：郭治群博士

Student: Teng-Yang Tan

Adviser: Dr. Jyh-Chyurn Guo



Submitted to Department of Electronic Engineering & Institute of Electronics

College of Electrical Engineering and Computer Science

National Chiao Tung University

in partial Fulfillment of the Requirements

for the Degree of

Master

in Electronics Engineering

August 2006

Hsinchu, Taiwan, Republic of China

中華民國九十五年八月

# 單晶片電感模型研發及射頻積體電路模擬與設計方面之應用

研究生：譚登陽

指導教授：郭治群博士

國立交通大學

電子工程學系電子研究所

## 中文摘要

近十年來，深次微米 CMOS 製程技術帶動了系統晶片的快速演進。由於 CMOS 技術其本身的優勢為高整合性，低成本，高速度以低功率等，RF CMOS 已變為無線通訊系統晶片可行方案。但是，於 RF CMOS 產品發展過程中，缺乏準確和可微縮性之射頻元件模型已成為主要的障礙，射頻元件模型發展之挑戰來自於複雜的電磁耦合與半導體矽基板所引起能量損耗等效應。單晶片電感模型乃為此領域中最具挑戰的主題之一，也因此激發我們研究的動機。

本論文中，我們針對螺旋狀電感發展一個新的 T 模型之等效電路，其可以準確地模擬寬頻的特性。在寬頻的範圍下，此模型中螺旋線圈和基板之 RLC 網路電路，對導體和基板損耗之效應扮演極重要的角色。至於已存在的  $\pi$  模型則無法準確地模擬上述所提及的現象。再者，我們已成功地將簡單的 T 模型延伸至 2T 模型，以適用於對稱型和差動型電感，其於關鍵射頻電路如混頻器、壓控振盪器及低雜訊放大器應用方面相當地受歡迎，此模型的準確性於頻率高達 20 GHz 的頻寬下已與量測的 S 參數，輸入阻抗之實部及品質因素驗證，均有相當好的匹配，除了在寬頻下，其所有模型參數對圈數的變化已被驗證呈現線性的函數。透過等效電路分析，我們建立了一套參數汲取流程，可以進行參數自動汲取與最佳化。此可微縮性電感模型可成功輔助單晶片電感設計，並進行最佳化的動作，及其準確性可高達 20GHz 的頻寬，依寬頻電路設計需求可以改善射頻電路模擬之準確性。

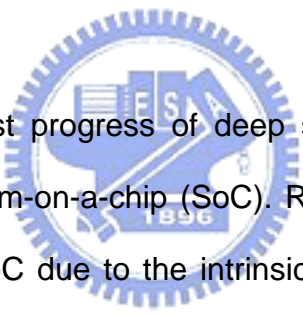
# **On-chip Inductor Model Development and Applications in RF CMOS Circuit Simulation and Design**

**Student: Teng-Yang Tan**

**Advisor: Dr. Jyh-Chyurn Guo**

**Department of Electronic Engineering and Institute of Electronics  
National Chiao Tung University**

## **Abstract**



In recent decade, the fast progress of deep submicron CMOS technology is driving the realization of system-on-a-chip (SoC). RF CMOS has become an viable solution for communication SoC due to the intrinsic advantages of high integration, low cost, high speed, and low power, etc. However, for the development of RF CMOS products, lack of accurate and scalable RF device models has been a major roadblock. The challenges of RF CMOS device model development come from the complicated electromagnetic coupling and energy loss effects originated from the semi-conducting substrate of bulk Si. On-chip inductor model is among the most challenging topics in the area and stimulates our motivation of this work.

In this work, a new equivalent circuit model named as T-model has been developed for single-end spiral inductor to accurately simulate broadband characteristics. The spiral coil and substrate RLC networks built in this model play a key role responsible for conductor loss and substrate loss effects in the wideband regime. The mentioned phenomena cannot be accurately simulated by the existing

inductor models such as  $\pi$ -model. The simple T-model has been successfully extended to 2-T model for symmetric and differential inductors, which become very popular in key RF circuits such as mixer, VCO, and LNA, etc. The model accuracy has been proven by good match with measured S-parameters,  $\text{Re}(Z_{in}(\omega))$ , and  $Q(\omega)$  over broadband of frequencies up to 20 GHz. Besides the broadband feature, scalability is justified by the good agreement with a linear function of coil numbers for all model parameters. A parameter extraction flow has been established through equivalent circuit analysis to enable automatic parameter extraction and optimization. This scalable inductor model can facilitate optimization design of on-chip inductor and the accuracy proven up to 20 GHz can improve RF circuit simulation accuracy demanded by broadband design.



## 誌謝

感謝我的家人與朋友在這兩年的研究生涯中一路上的支持和鼓勵，有他們的加油和信任，讓我倍感溫暖，讓我可以繼續下去。同時我也要特別的感謝我的父母，感謝您們從小到大辛勤的栽培我，讓我可以接受好的教育，讓我可以順利地完成碩士學位。

在此，我也要感謝林益民、葉致廷與杜珮瑩三位同學，在研究與修課上提供我許多意見，讓我在研究上有新的體認和新的想法。實驗室學弟們在我碩士生涯的這兩年中，也是伴我成長功不可沒的學習伴侶，陪同我一起作研究和運動的好夥伴。

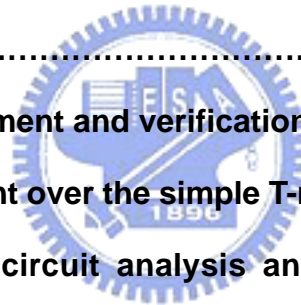
最後要感謝的是我的指導老師，郭治群教授平日的督導與鞭策，以致於我才能利地完成此篇論文，謹以這篇論文獻給所有想投入此領域研究的人，也期望學弟們能將此篇論文更加發揮其價值，延續未做完的部分。



# Contents

<b>Abstract.....</b>	<b>i</b>
<b>Contents.....</b>	<b>v</b>
<b>Figure Captions.....</b>	<b>iv</b>
<b>Chapter 1 Introduction.....</b>	<b>1</b>
1.1 Research Motivation.....	1
1.2 Thesis Organization.....	2
<b>Chapter 2 Review on Existing Inductor Models – Remaining</b>	
<b>Issues.....</b>	<b>4</b>
2.1 Requirements for inductor models for RF circuit simulation.....	4
2.2 Analysis and comparison of existing models.....	5
2.2.1 Accuracy and bandwidth of validity.....	6
2.2.2 Scalability and geometries of validity.....	14
2.2.3 Model parameter extraction flow and automation.....	15
2.3 Model enhancement strategies.....	16
2.4 Fundamental quality factor of an inductor.....	17
<b>Chapter 3 Broadband and Scalable On-chip Inductor</b>	
<b>Model.....</b>	<b>25</b>
3.1 Broadband accuracy for on-chip inductors.....	25
3.1.1 Simulation tool and simulation method.....	26
3.1.2 Conductor and substrate loss effect – model and theory.....	30

3.1.3 Varying substrate resistivity effect – model and theory.....	35
3. 2 Scalability for single – end spiral inductors.....	42
3.2.1 Layout parameter and geometry effect.....	43
3.2.2 Conductor and dielectric material properties and RF measurement.....	43
3.2.3 Varying substrate resistivity.....	45
3. 3 T-model development and verification.....	45
3.3.1 Equivalent circuit analysis.....	46
3.3.2 Model parameter extraction flow.....	48
3.3.3 Conductor loss and substrate loss effect.....	51
3.3.4 Broadband accuracy.....	55
3.3.5 Scalability.....	69
3. 4 T-model enhancement and verification.....	73
3.4.1 Enhancement over the simple T-model.....	74
3.4.2 Equivalent circuit analysis and Model parameter extraction flow.....	75
3.4.3 Conductor loss and substrate loss effect.....	79
3.4.4 Varying substrate resistivity effect.....	79
3.4.5 Broadband accuracy.....	85
3.4.6 Scalability.....	87





<b>Chapter 4 Symmetric Inductor Model Development and Verification.....</b>	<b>89</b>
4.1 Symmetric inductor design and fabrication.....	89
4.1.1 New symmetric inductor design strategy.....	89
4.1.2 EM simulation for layout optimization.....	92
4.1.3 Layout parameter and geometry analysis – taper structure.....	94
4.1.4 Comparison with conventional symmetric inductors.....	95
4.2 Symmetric inductor model development.....	96
4.2.1 Model parameter extraction flow.....	97
4.2.2 Broadband accuracy.....	102
4.2.3 Scalability.....	106
<b>Chapter 5 Future work.....</b>	<b>109</b>
<b>References.....</b>	<b>111</b>

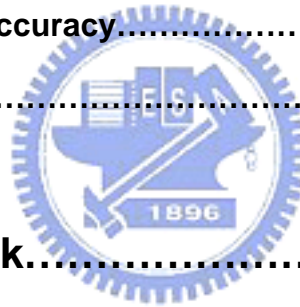


## Figure Captions

### Chapter 2

	page
Fig. 2.1 (a) Top(die photo);Middle, 3-D view (b)the lumped physical model of a spiral inductor on silicon.....	7

Fig. 2.2	Modify $\pi$ -model for on-chip spiral inductors.....	9
Fig. 2.3	Figure 2.3 Comparison of $S_{21}$ (magnitude) between $\pi$ -model simulation and measurement for spiral inductors. Coil numbers (a) $N=1.5$ , (b) $N=2.5$ , (c) $N=3.5$ , (d) $N=4.5$ .....	10
Fig. 2.4	Comparison of $S_{21}$ (phase) between $\pi$ -model simulation and measurement for spiral inductors. Coil numbers (a) $N=1.5$ , (b) $N=2.5$ , (c) $N=3.5$ , (d) $N=4.5$ .....	11
Fig. 2.5	Comparison of $S_{11}$ (magnitude) between $\pi$ -model simulation and measurement for spiral inductors. Coil numbers (a) $N=2.5$ , (b) $N=3.5$ , (c) $N=4.5$ , (d) $N=5.5$ .....	11
Fig. 2.6	Comparison of $S_{11}$ (phase) between $\pi$ -model simulation and measurement for spiral inductors. Coil numbers (a) $N=2.5$ , (b) $N=3.5$ , (c) $N=4.5$ , (d) $N=5.5$ .....	12
Fig. 2.7	Comparison of $L(\omega)$ between $\pi$ -model simulation and measurement for spiral inductors. Coil numbers (a) $N=2.5$ , (b) $N=3.5$ , (c) $N=4.5$ , (d) $N=5.5$ .....	12
Fig. 2.8	Comparison of $R_e(Z_{in}(\omega))$ between $\pi$ -model simulation and measurement for spiral inductors. Coil numbers (a) $N=2.5$ , (b) $N=3.5$ , (c) $N=4.5$ , (d) $N=5.5$ .....	13
Fig. 2.9	Comparison of $Q(\omega)$ between $\pi$ -model simulation and measurement for spiral inductors. Coil numbers (a) $N=2.5$ , (b) $N=2.5$ , (c) $N=3.5$ , (d) $N=4.5$ .....	13
Fig. 2.10	Spiral inductor geometries.....	14
Fig. 2.11	Inductor with a series resistance.....	18
Fig. 2.12	Inductor with a parallel resistance.....	19

Fig. 2.13	Parallel RLC circuit.....	21
Fig. 2.14	Alternative method for determining the Q in real inductors.....	24

## Chapter 3

		page
Fig. 3.1	Conventional $\pi$ -model.....	26
Fig. 3.2	Layer stackup simulation by HFSS.....	27
Fig. 3.3	Effective oxide dielectric constant equivalents from M1 to M2.....	28
Fig. 3.4	Ground ring setup by HFSS.....	29
Fig. 3.5	Layout of convention single-end spiral inductor.....	30
Fig. 3.6	Cross section for single-end spiral inductor coils.....	31
Fig. 3.7	Simulate eddy current on the substrate surface by HFSS.....	33
Fig. 3.8	Simulate eddy current in the interior substrate surface by HFSS.....	34
Fig. 3.9	Simplified illustration of T-model.....	35
Fig. 3.10	Measured inductor series inductance s.....	37
Fig. 3.11	Measured inductor series resistance.....	38
Fig. 3.12	Measured inductor Q.....	39
Fig. 3.13	Cut-away view of the electromagnetic fields associated with single-end spiral inductor on (a) lightly doped substrate, (b) epi substrate, and (c) epi substrate with PGS. PGS terminates the electric field but allows the magnetic field to penetrate through.....	41
Fig. 3.14	Simplified illustration of improve T-model.....	42
Fig. 3.15	RF measurement equipment.....	44

Fig. 3.16	T-model for on-chip spiral inductors. (a) Equivalent circuit schematics (b) Intermediate stage of schematic block diagrams for circuit analysis. (c) Final stage of schematic block diagrams for circuit analysis.....	47
Fig. 3.17	T-model parameter formulas and extraction flow chart.....	51
Fig. 3.18	$Q(\omega)$ calculated by equivalent circuit removing $R_p$ from original T-model and adding $R_s(\omega)$ to simulate skin effect for spiral inductors with various coil numbers (a) $N=2.5$ (b) $N=3.5$ (c) $N=4.5$ (d) $N=5.5$ ....	51
Fig. 3.19	Frequency dependent $R_s$ extracted from measurement through definition of $R_s = R_e(-1/Y_{21})$ and the comparison with $R_s(\omega)$ calculated by ideal model of equation 3.9 for spiral inductors with various coil numbers, $N=2.5, 3.5, 4.5, 5.5$ .....	53
Fig. 3.20	$L(\omega)$ calculated by equivalent circuit simulation with $R_p$ removed from original T-model for spiral inductors with various coil numbers (a) $N=2.5$ (b) $N=3.5$ (c) $N=4.5$ (d) $N=5.5$ .....	53
Fig. 3.21	$\text{Re}(Z_{in}(\omega))$ calculated by equivalent circuit simulation with $R_p$ removed from original T-model for spiral inductors with various coil numbers (a) $N=2.5$ (b) $N=3.5$ (c) $N=4.5$ (d) $N=5.5$ .....	54
Fig. 3.22	$Q(\omega)$ calculated by equivalent circuit simulation with $R_p$ removed from original T-model for spiral inductors with various coil numbers (a) $N=2.5$ (b) $N=3.5$ (c) $N=4.5$ (d) $N=5.5$ .....	55
Fig. 3.23	Comparison of $S_{21}$ (magnitude) between T-model simulation and measurement for spiral inductors. Coil numbers (a) $N=1.5$ , (b) $N=2.5$ , (c) $N=3.5$ , (d) $N=4.5$ .....	56
Fig. 3.24	Comparison of $S_{21}$ (magnitude) between T-model simulation and	

	measurement for spiral inductors. Width for N=1.5 (a) W=3 $\mu$ m, (b) W=9 $\mu$ m, (c) W=15 $\mu$ m, (d) W=30 $\mu$ m.....	56
Fig. 3.25	Comparison of S <sub>21</sub> (phase) between T-model simulation and measurement for spiral inductors. Coil numbers (a) N=1.5, (b) N=2.5, (c) N=3.5, (d) N=4.5.....	57
Fig. 3.26	Comparison of S <sub>21</sub> (phase) between T-model simulation and measurement for spiral inductors. Width for N=1.5 (a) W=3 $\mu$ m, (b) W=9 $\mu$ m, (c) W=15 $\mu$ m, (d) W=30 $\mu$ m.....	58
Fig. 3.27	Comparison of S <sub>11</sub> (magnitude) between T-model simulation and measurement for spiral inductors. Coil numbers (a) N=1.5, (b) N=2.5, (c) N=3.5, (d) N=4.5.....	59
Fig. 3.28	Comparison of S <sub>11</sub> (magnitude) between T-model simulation and measurement for spiral inductors. Width for N=1.5 (a) W=3 $\mu$ m, (b) W=9 $\mu$ m, (c) W=15 $\mu$ m, (d) W=30 $\mu$ m.....	59
Fig. 3.29	Comparison of S <sub>11</sub> (phase) between T-model simulation and measurement for spiral inductors. Coil numbers (a) N=1.5, (b) N=2.5, (c) N=3.5, (d) N=4.5.....	60
Fig. 3.30	Comparison of S <sub>11</sub> (phase) between T-model simulation and measurement for spiral inductors. Width for N=1.5 (a) W=3 $\mu$ m, (b) W=9 $\mu$ m, (c) W=15 $\mu$ m, (d) W=30 $\mu$ m.....	61
Fig. 3.31	Comparison of L( $\omega$ ) between T-model simulation and measurement for spiral inductors. Coil numbers (a) N=1.5, (b) N=2.5, (c) N=3.5, (d) N=4.5.....	62
Fig. 3.32	Comparison of L( $\omega$ ) between T-model simulation and measurement for spiral inductors. Width for N=1.5 (a) W=3 $\mu$ m, (b) W=9 $\mu$ m, (c) W=15 $\mu$ m, (d) W=30 $\mu$ m.....	63

	W=15 $\mu$ m, (d) W=30 $\mu$ m.....	
Fig. 3.33	Comparison of $R_e(Z_{in}(\omega))$ between T-model simulation and measurement for spiral inductors. Coil numbers (a) N=1.5, (b) N=2.5, (c) N=3.5, (d) N=4.5.....	63
Fig. 3.34	Comparison of $R_e(Z_{in}(\omega))$ between T-model simulation and measurement for spiral inductors. Width for N=1.5 (a) W=3 $\mu$ m, (b) W=9 $\mu$ m, (c) W=15 $\mu$ m, (d) W=30 $\mu$ m.....	64
Fig. 3.35	Comparison of $Q(\omega)$ between T-model simulation and measurement for spiral inductors. Coil numbers: N=2.5, 3.5, 4.5, 5.5.....	65
Fig. 3.36	Comparison of $Q(\omega)$ between T-model simulation and measurement for spiral inductors. Width for N=1.5 (a) W=3 $\mu$ m, (b) W=9 $\mu$ m, (c) W=15 $\mu$ m, (d) W=30 $\mu$ m.....	65
Fig. 3.37	Comparison of $Q(\omega)$ and self-resonance frequency $f_{SR}$ corresponding to $Q=0$ among T-model, reduced T-model ( $L_{sub} = R_{loss} = 0$ ) and measurement for spiral inductors with various coil numbers.	66
Fig. 3.38	(a) Self-resonance frequency $f_{SR}$ of on –chip spiral inductors with various coil numbers, N=2.5, 3.5, 4.5, 5.5 (a) comparison between measurement, ADS simulation, and analytical model. (b) $C_p$ , $C_{ox}$ , and $C_{sub}$ effect on $f_{SR}$ calculated by ADS simulation and analytical model. Comparison with measured $f_{SR}$ to indicate the $f_{SR}$ increase contributed by eliminating the parasitic capacitances, $C_p$ , $C_{ox}$ , and $C_{sub}$ respectively.....	68
Fig. 3.39	T-model RLC network parameters versus coil numbers, spiral coil's RLC network parameters (a) $L_s$ (b) $R_s$ , (c) $C_p$ and $C_{ox}$ and (d) $R_p$ .....	71
Fig. 3.40	T-model RLC network parameters versus coil numbers, lossy	

	substrate RLC network parameters (a) $C_{sub}$ (b) $1/R_{sub}$ , (c) $L_{sub}$ and (d) $R_{loss}$ .....	71
Fig. 3.41	T-model RLC network parameters versus width, spiral coil's RLC network parameters (a) $L_s$ (b) $R_s$ , (c) $C_p$ and (d) $R_p$ .....	72
Fig. 3.42	T-model RLC network parameters versus width, lo spiral coil's RLC network parameters (a) $C_{ox1}$ (b) $C_{ox2}$ .....	72
Fig. 3.43	T-model RLC network parameters versus width, lossy substrate RLC network parameters (a) $C_{sub}$ (b) $1/R_{sub}$ , (c) $L_{sub}$ and (d) $R_{loss}$ .....	73
Fig. 3.44	Magnetic field in the single-end spiral inductor.....	74
Fig. 3.45	Improved T-model (a) equivalent circuit schematics, (b) and (c) schematic block diagram for circuit analysis.....	76
Fig. 3.46	Improved T-model parameter formulas and extraction flow chart.....	78
Fig. 3.47	Comparison between ADS momentum simulation, measurement, and improved T-model for on-chip inductor (a) $S_{11}$ (mag, phase) (b) $S_{21}$ (mag, phase) (c) $L(\omega)$ , $R_e(Z_{in}(\omega))$ (d) $Q(\omega)$ .....	80
Fig. 3.48	(a) $Q_m$ (b) $f_m$ (c) $f_{Lmax}$ (d) $f_{SR}$ under varying $\rho_{si}$ (0.01 ~ 1K $\Omega$ -cm) predicted by ADS Momentum simulation.....	81
Fig. 3.49	Improved T-model parameters under varying $\rho_{si}$ (a) $R_{sub}$ , $R_p$ (b) $L_{sub}$ , $L_{sub1,2}$ , $R_{loss}$ , $R_{loss1,2}$ (c) $C_p$ (d) $C_{ox1,2}$ $C_{sub}$ .....	83
Fig. 3.50	$Q_m$ vs. Improved T-model parameters under varying $\rho_{si}$ (a) $R_p$ (b) $R_{sub}$ , (c) $L_{sub}$ , $L_{sub1,2}$ (d) $R_{loss}$ , $R_{loss1,2}$ .....	83
Fig. 3.51	$f_{SR}$ vs. Improved T-model parameters under varying $\rho_{si}$ (a) $C_p$ (b) $C_{sub}$ , (c) $C_{ox1}$ (d) $C_{ox2}$ .....	84
Fig. 3.52	Comparison of improved T-model and measured $S_{11}$ , $S_{21}$ (mag, phase) for inductors. Coil numbers (a) N=2.5 (b) N=3.5 (c) N=4.5 (d)	85

	N5.5.....	
Fig. 3.53	Comparison of improved T-model and measured $L(\omega)$ , $\text{Re}(Z_{in}(\omega))$ for inductors. Coil numbers (a) $N=2.5$ (b) $N=3.5$ (c) $N=4.5$ (d) $N=5.5$ .....	86
Fig. 3.54	Improved T-model parameters vs. coil number (a) $L_s$ , $C_p$ , $C_{ox1,2}$ (b) $R_s$ , $R_p$ (c) $C_{sub}$ , $L_{sub}$ , $L_{sub1,2}$ (d) $1/R_{sub}$ , $R_{loss}$ , $R_{loss1,2}$ .....	87
Fig. 3.55	Improved T-model parameters vs. coil number (a) $L_s$ , $C_p$ , $C_{ox1,2}$ (b) $R_s$ , $R_p$ (c) $C_{sub}$ , $L_{sub}$ , $L_{sub1,2}$ (d) $1/R_{sub}$ , $R_{loss}$ , $R_{loss1,2}$ .....	88

## Chapter 4

		page
Fig. 4.1	Top view of a conventional differential inductor.....	90
Fig. 4.2	Top view of a fully symmetrical inductor.....	91
Fig. 4.3	$Q_{max}$ and $f_{max}$ vs. $L_{max}$ calculated by ADS momentum for taper inductor optimization design.....	93
Fig. 4.4	Fully taper symmetry inductor layout.....	94
Fig. 4.5	2T model for fully taper symmetric inductor (a) equivalent circuit schematics (b) intermediate stage (c) final stage of block diagram for circuit analysis.....	99
Fig. 4.6	2T-model parameter derivation formulas and extraction flow chart.....	99
	.	
Fig. 4.7	Comparison of 2T-model and measurement for $R=30, 60, 90 \mu\text{m}$ (a) $\text{Mag}(S_{11})$ (b) $\text{Phase}(S_{11})$ (c) $\text{Mag}(S_{21})$ (d) $\text{Phase}(S_{21})$ .....	104
Fig. 4.8	Comparison of 2T-model and measurement under single-ended excitation for $R=30, 60, 90\mu\text{m}$ (a) $L(\omega)$ (b) $\text{Re}(Z_{in}(\omega))$ .....	104



Fig. 4.9	Comparison of 2T-model and measurement under differential excitation for $R=30, 60, 90\mu\text{m}$ (a) $R_e(S_d)$ (b) $I_m(S_d)$ (c) $L_d(\omega)$ (d) $R_e(Z_d(\omega))$ .....	105
Fig. 4.10	Comparison of 2T-model and measurement for $R=30, 60, 90\text{ m}$ (a) $R_e(Z_{\text{dut1}}(\omega))$ (b) $I_m(Z_{\text{dut1}}(\omega))$ (c) $R_e(Z_{\text{dut2}}(\omega))$ (d) $I_m(Z_{\text{dut2}}(\omega))$ .....	105
Fig. 4.11	Comparison of $Q(\omega)$ between 2T-model simulation and measurement for fully taper symmetry inductor with various radiuses: $R=30, 60, 90\mu\text{m}$ .....	106
Fig. 4.12	2T-model RLC network parameters versus inner radius, fully taper symmetry coil's RLC network parameters (a) $L_{s1,2}$ (b) $R_{s1,2}$ (c) $C_{p1,2}$ (d) $C_{\text{ox}1,2,3}$ .....	107
Fig. 4.13	2T-model RLC network parameters versus inner radius, fully taper symmetry coil's RLC network parameters (a) $L_{\text{sk}1,2}$ (b) $R_{\text{sk}1,2}$ (c) $R_{\text{p}1,2}$ .....	108
Fig. 4.14	2T-model RLC network parameters versus inner radius, lossy substrate RLC network parameters (a) $C_{\text{sub}}$ (b) $1/R_{\text{sub}}$ (c) $L_{\text{sub}}$ (d) $R_{\text{loss}}$ .....	108

# Chapter 1

## Introduction

### 1.1 Research Motivation

Wireless communication has been one of major driving force for accelerated semiconductor technology progress in the current electronic industry. High frequency IC product developed for the demand of mobile communication, wireless data/voice transmission is an even more important application for global semiconductor manufacturers. Moreover, it fueled larger demand for low cost, high competitive, portable products for current market.

Monolithic inductors have been commonly used in radio frequency integrated circuits (RFICs) for wireless communication systems such as wireless local area networks, personal handsets, and global position systems. The inductor is a critical device for RF circuits such as voltage-controlled oscillators (VCO), Impedance matching networks and RF amplifiers. Its characteristics generally crucially affect the overall circuit performance. However, to meet the increasingly stringent requirements driven by advancement of wireless communication systems, the characteristic of conventional monolithic inductive components is too poor to be used. In order to conform market requirement and achieve system-on-a chip (SoC), the CMOS, BiCMOS, and SiGe technologies are inevitable and passive components must be integrated. Even though SiGe or BiCMOS technologies may offer better performance, lower power, and lower noise, the much higher process complexity and fabrication cost limit their applications in consumer and communication products, which are very

cost sensitive. Therefore, we focus our research on CMOS due to its higher integration and lower cost.

Besides, the circuit designers generally have critical concern about the accuracy of simulation models for active and passive components. As a result, an accurate RF device model suitable for various manufacturing technologies is strongly demanded. The mentioned requirement triggers our motivation of this work to build an accurate and scalable model for on-chip spiral inductors in RF circuit applications. Besides the accuracy and scalability, a reliable de-embedding method and an efficient model parameter extraction flow are the primary goals of this work. The accurate extraction of intrinsic device characteristics is prerequisite to accurate modeling while the challenges become tougher for miniaturized devices. An efficient model parameter extraction flow can be automated through commercial extraction tool to expedite the model extraction and optimization.



## 1.2 Thesis Organization

The theme of this thesis is the development of an accurate and scalable on-chip inductor model applicable for RF circuit simulation and design over broadband up to 20 GHz and beyond. In Chapter 2, I will discuss the existing issues for current inductor models, e.g.  $\pi$ -model. Also, I will introduce briefly the application of pi-model which is used to build in passive model.

In Chapter 3 and Chapter 4, I will focus on the development of a broadband and scalable model for on-chip Inductor. Both single-end and symmetric inductors have been covered in this work. A new symmetric inductor of fully symmetric layout as well as taper metal line have been fabricated and a new de-embedding method has been

derived to realize accurate extraction of the intrinsic device parameters. A parameter extraction flow has been established through equivalent circuit analysis to enable automatic parameter extraction and optimization. The equivalent circuit, physics phenomenon that is observation from 3D EM simulation, and analysis of extracted parameters will all be explained in these chapters. According to above concepts, we will design new model to present different inductor at the high frequency characteristics. We also improve asymmetry structures for spiral and conventional symmetry inductor between the  $S_{11}$  and  $S_{22}$ . But it can decrease the quality factor (Q) and self-resonant frequency ( $f_{SR}$ ). So we will design taper inductor to increase quality factor. For the above reason, how to improve the characteristics of passive devices and achieve low cost and high competition simultaneously is worth trying.

In Chapter5, the lump-element equivalent circuit verified and analyzed by ADS circuit simulator is to simulate circuit level for different inductor modification.

Chapter7 is discussed the future work and Appendixes related to analytical formula for lump-element equivalent circuit. Our analysis and inference will be verified through ADS simulation result for equivalent circuit. And we gives the conclusions to this work and its development in the future.

# Chapter 2

## Review on Existing Inductor Models

### – Remaining Issues

#### 2.1 Requirements for inductor models for RF circuit simulation

The rapid growth of the wireless communication market has fueled a large demand for low cost, high competitive, portable products. Traditionally, radio systems are implemented on the board level incorporating a lot of discrete components. Recently, compared with discrete and hybrid designs, the monolithic approach offers improved reliability, lower cost and smaller size, broadband performance, and design flexibility. In conventional design, bonding wires having a relatively high Q were used to replace on-chip inductors. However, the bonding wires generally suffer worse variations in inductance value because that they cannot be as tightly controlled as the on-chip inductors implemented by integrated circuit process. Recent advancement in silicon based RF CMOS technology can provide RF passive components such as inductors with fair performance suitable for analog and RF IC design up to several giga-hertz, then it can be integrated on a chip to match market demands. Therefore, an accurate on-chip RF passive device model applicable for circuit simulation and design becomes indispensable and the mentioned requirement triggers our motivation of this work.

Extensive research work has been done to investigate inductors of various layouts and topologies such as spiral inductor, conventional symmetric inductor, and fully

symmetric inductors of single-end and differential configuration. All the mentioned inductors have been fabricated on semi-conducting Si substrate for measurement, characterization as well as model parameter extraction for circuit simulation model development. In this chapter, we will introduce existing inductor models targeted for Si based RF circuit simulation. Comparison will be done for various models in terms of accuracy and bandwidth of validity, scalability and geometry of validity as well as model parameter extraction methodologies, etc.

## 2.2 Analysis and comparison of existing models

Monolithic inductors have drawn increasing interest for applications in radio frequency integrated circuit (RF ICs), such as low noise amplifier (LNA), voltage controlled oscillator (VCO), Mixer, input and output match network. It is believed that SoC approach can provide benefit of lower cost, higher integration, and better system performance. However, some inherent limitations originated from the low resistivity substrate of bulk Si should be overcome through effort in process technology and layout or new configurations in circuit operation, e.g. differentially driven instead of single end operation. To facilitate the RF circuit simulation accuracy and prediction capability, the physical limitation coming from substrate loss, conductor loss, and the mutual interaction should be carefully considered and implemented in the circuit level models. The physical mechanisms, which are well recognized for on Si chip inductors include eddy currents on spiral metal coils and semiconducting substrate due to instantaneous electromagnetic field coupling, crossover capacitance between the spiral coils and under-pass, coupling capacitance between monolithic inductor and substrate, substrate capacitance and substrate ohmic loss, etc. In the following, the

discussion on mentioned model features will be provided.

## 2.2.1 Accuracy and bandwidth of validity

The lack of accurate model for on-chip inductors presents one of the most challenging problems for silicon-based RF IC design. In conventional IC technologies, inductors are not considered as standard components like transistors, resistors, or capacitors, whose equivalent circuit models are usually included in the Spice model for circuit simulation. However, this situation is rapidly changing as the demand for RF IC's continues to grow. Various approaches for modeling inductors on silicon have been reported in past decade. Most of these models are based on numerical techniques, curve fitting or empirical formulae and therefore are relatively inaccurate for higher frequencies. For monolithic inductor design and optimization, a compact physical model is required. The difficulty of physical modeling stems from the complexity of high frequency phenomena such as the eddy currents in the coil conductor and semiconducting substrate as well as the substrate loss in the silicon. The key to accurate physical modeling is firstly to identify all the parasitic and loss effects and then to implement a physics based model for simulating the identified parasitic and loss effects. Since an inductor is intended for storing magnetic energy, the inevitable resistance and capacitance in a real inductor are counter-productive and thus are considered parasitic effects. The parasitic resistances dissipate energy through ohmic loss while the parasitic capacitances store electric energy. A traditional equivalent circuit model of an inductor generally called  $\pi$ -model is shown in Fig. 2.1

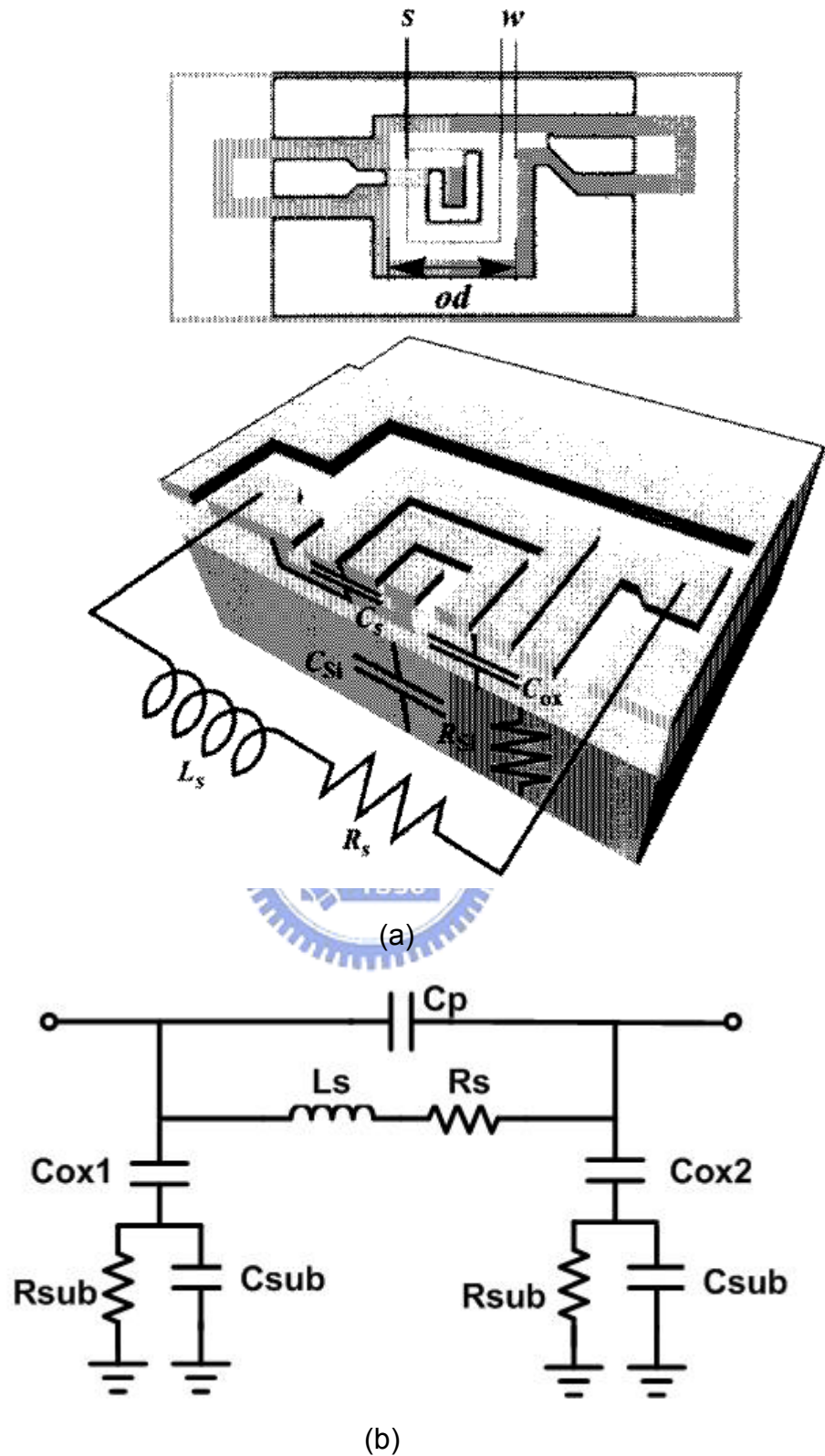


Figure 2.1 (a) Top (die photo);Middle, 3-D view (b)the lumped physical model of a spiral inductor on silicon



The inductance and resistance of the spiral and underpass is represented by the series inductance,  $L_s$ , and the series resistance,  $R_s$ , respectively. The overlap between the spiral and the underpass allows direct capacitive coupling between the two terminals of the inductor. The feed-through path is modeled by the parallel capacitance,  $C_p$ . The oxide capacitance between the spiral and the silicon substrate is modeled by  $C_{ox}$ . The silicon substrate capacitance and resistance are modeled by  $C_{si}$  and  $R_{si}$ . There are several sources of loss in a monolithic inductor. One relatively obvious loss comes from the series winding resistance. This is because the interconnect metal used in most CMOS processes. The DC resistance of the inductor is easily calculated as the product of this sheet resistance and the number of squares in the metal strip. However, at high frequencies the resistance of the strip increases due to skin effect, proximity effect and current crowding. The substrate loss will increase with frequency due to the dissipative currents that flow in the silicon substrate. In fact, there are two different physical mechanisms that cause the induction of these currents and opposition flux.

Although physical considerations are included in such a structure, the original  $\pi$ -model lacks the following important feature:

1. Strong frequency dependence of series inductance and resistance as a result of the current crowding in the crowding
2. Frequency-independent circuit structure that is compatible with transient analysis and broadband design
3. It is difficult to match high frequency behaviors, especially for thick metal case where metal-line-coupling capacitance is not negligible and substrate loss.

According to above theory and original  $\pi$ -model, we modify  $\pi$ -model for on-chip spiral

inductors over again to fit measurement data. Moreover, we add two new element  $R_p$  and  $L_{sub}$  to improve above third item, as shown figure 2.2. A parallel  $R_p$  is to simulate current crowding in coil's RLC network and series  $L_{sub1,2}$  are placed under the  $C_{ox1,2}$  to be represent eddy effect in the substrate RLC network. In order to verify the accuracy of the modify  $\pi$ -model, spiral inductors with various geometrical configurations were fabricated using  $0.13 \mu\text{m}$  eight-metal CMOS technology. To assess the model validity, we compare difference with model and measurement.

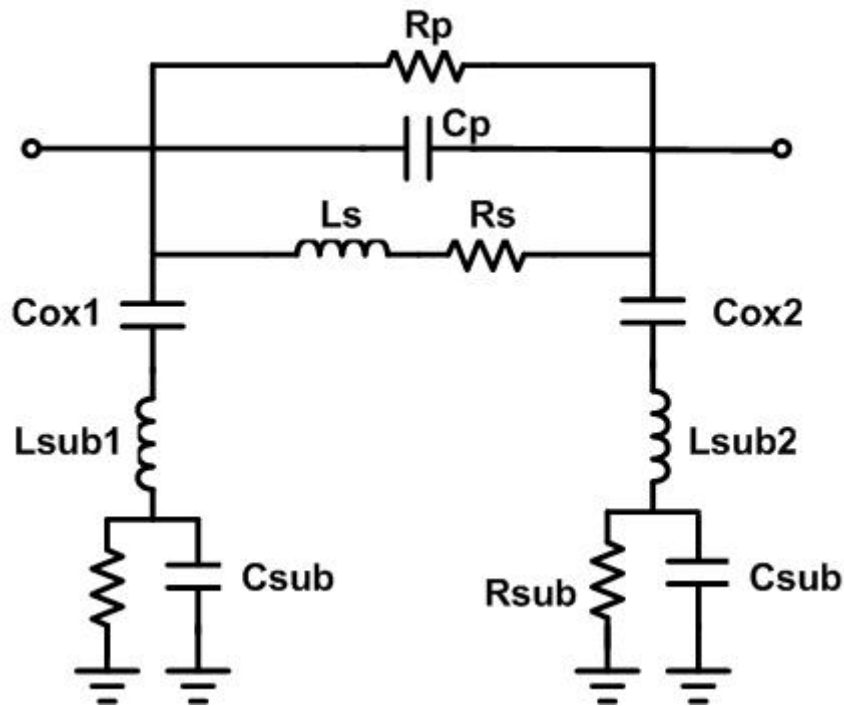


Figure 2.2 Modify  $\pi$ -model for on-chip spiral inductors.

Figure 2.3 and 2.4 show the measured and modeled S-parameters,  $\text{mag}(S_{21})$  and  $\text{phase}(S_{21})$  for a varying coil number of turns. As can be seen from these figures, the S-parameters of model match the measured data worst, especially a larger turn ( $N=3.5, 4.5, 5.5$ ) at the high frequency. Figure 2.5 (a) ~ (d) reveal the exact match of  $\text{Mag}(S_{11})$

for smaller coils ( $N= 2.5, 3.5$ ) over full frequency range up to 20GHz, but the other figure 2.6 shows enormous error of phase( $S_{11}$ ). Due to above match condition, modify  $\pi$ -model may be not suit to simulate measured S-parameters for spiral inductors. Besides, we also make comparison with performance parameters for spiral inductor, i.e.,  $L(\omega)$ ,  $R_e(Z_{in}(\omega))$ , and  $Q(\omega)$ . From figure 2.7 ~ 2.9 illustrates, we find that the modify  $\pi$ -model provides very good match with the measurement for  $L(\omega)$ ,  $R_e(Z_{in}(\omega))$ , and  $Q(\omega)$  before self-resonance frequency. According to above comparison, modify  $\pi$ -model may be not simulate all parameters of spiral inductors and maybe can simulate certain specific parameters, especially  $L(\omega)$ ,  $R_e(Z_{in}(\omega))$ , and  $Q(\omega)$ . Hence, in the following chapter, we will change equivalent circuit structure over again. We use 3D EM simulation by Ansoft HFSS to simulate on-chip inductor and discover truly conforms to the physics significance parameter to establish new equivalent circuit.

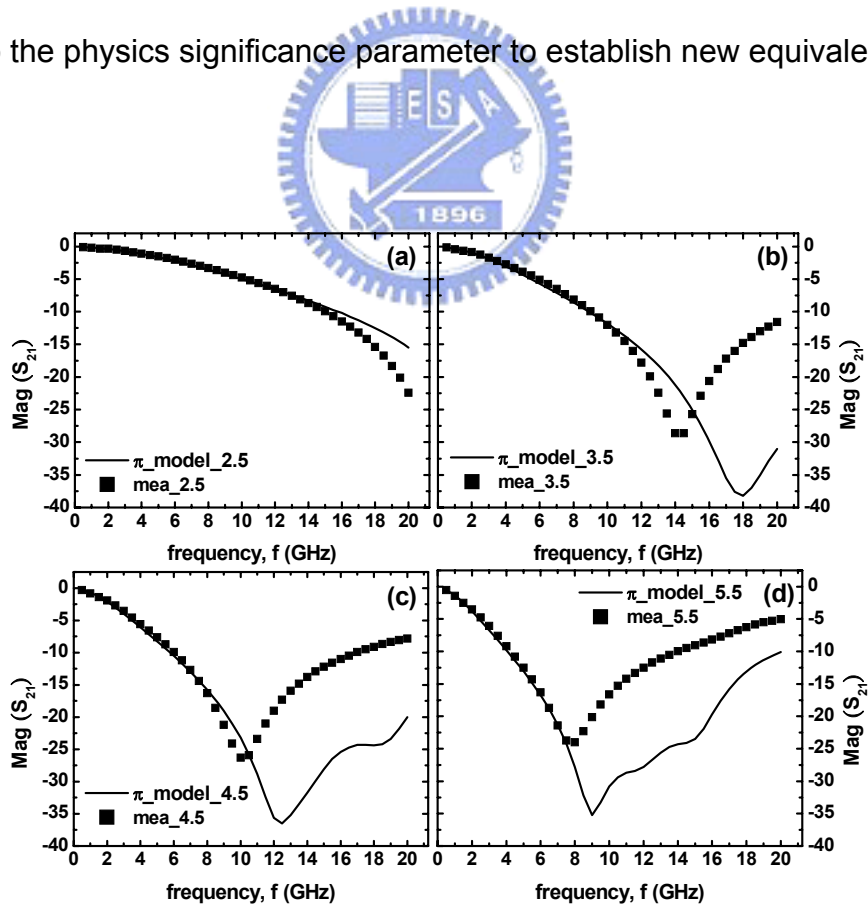


Figure 2.3 Comparison of  $S_{21}$  (magnitude) between  $\pi$ -model simulation and measurement for spiral inductors. Coil numbers (a)  $N=1.5$ , (b)  $N=2.5$ , (c)  $N=3.5$ , (d)

N=4.5

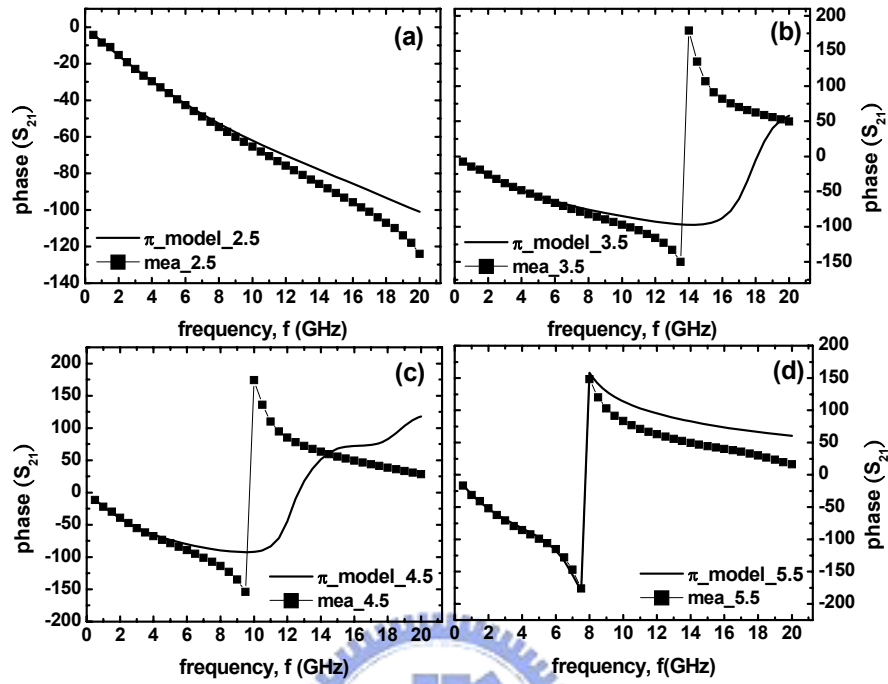


Figure 2.4 Comparison of  $S_{21}$  (phase) between  $\pi$ -model simulation and measurement for spiral inductors. Coil numbers (a) N=1.5, (b) N=2.5, (c) N=3.5, (d) N=4.5

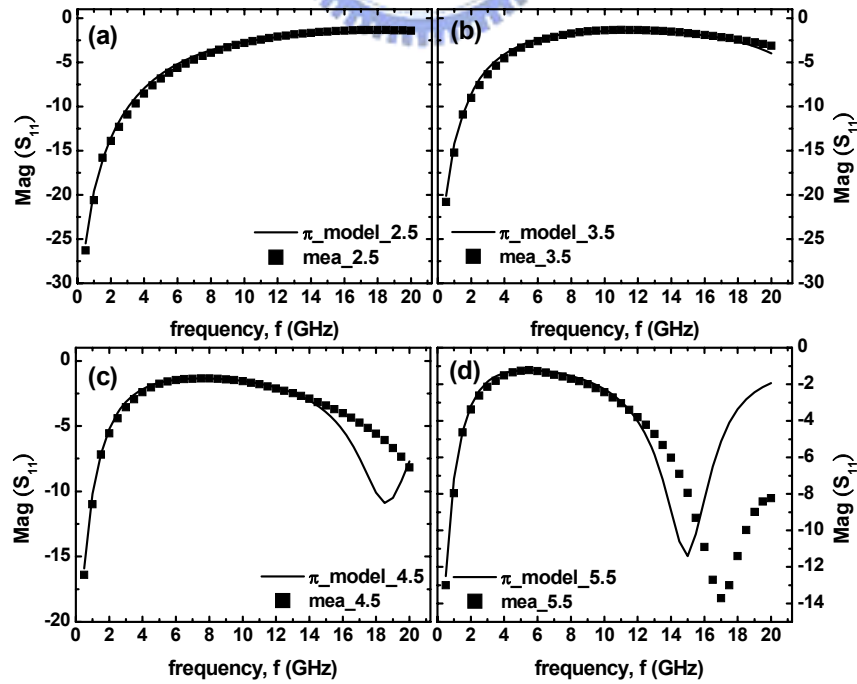


Figure 2.5 Comparison of  $S_{11}$  (magnitude) between  $\pi$ -model simulation and measurement for spiral inductors. Coil numbers (a) N=2.5, (b) N=3.5, (c) N=4.5, (d) N=5.5

N=5.5

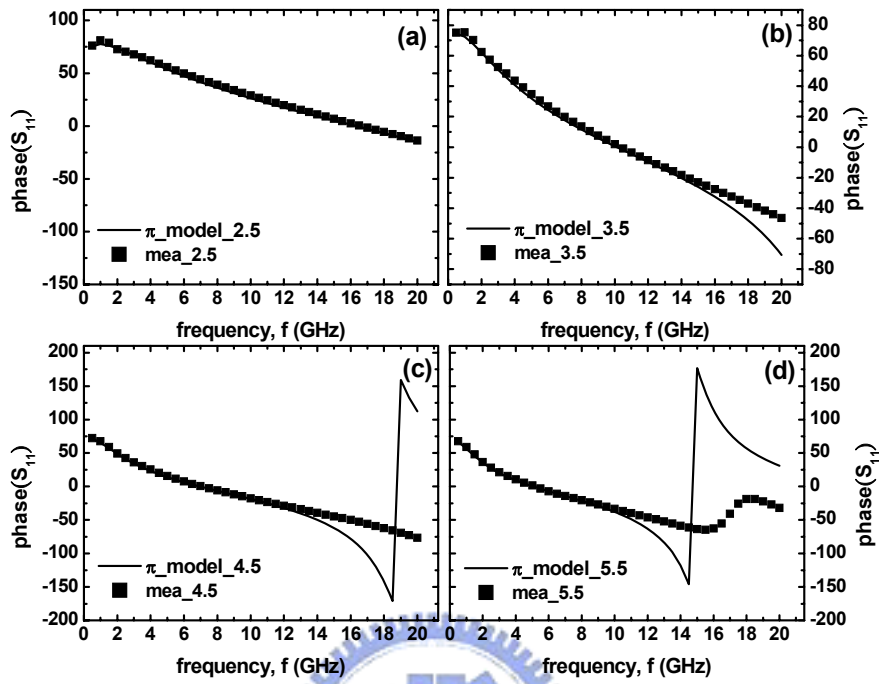


Figure 2.6 Comparison of  $S_{11}$  (phase) between  $\pi$ -model simulation and measurement for spiral inductors. Coil numbers (a) N=2.5, (b) N=3.5, (c) N=4.5, (d) N=5.5

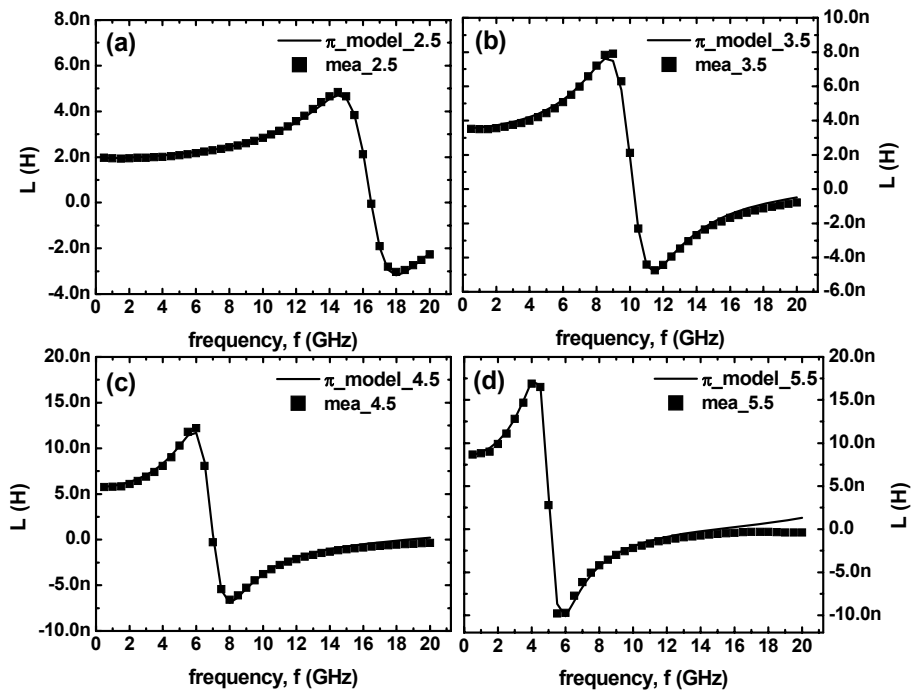


Figure 2.7 Comparison of  $L(\omega)$  between  $\pi$ -model simulation and measurement for

spiral inductors. Coil numbers (a) N=2.5, (b) N=3.5, (c) N=4.5, (d) N=5.5

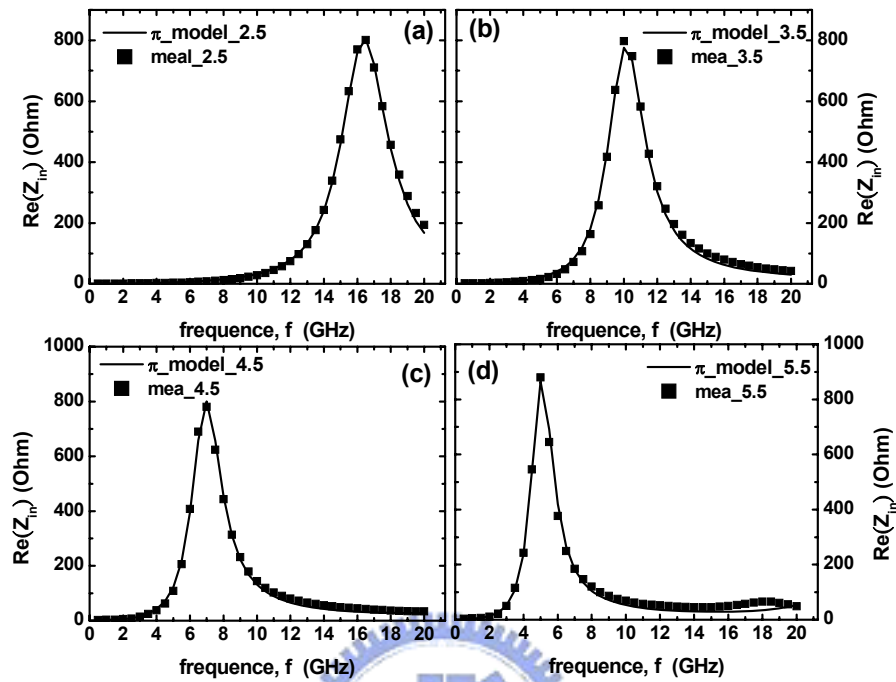


Figure 2.8 Comparison of  $Re(Z_{in}(\omega))$  between  $\pi$ -model simulation and measurement for spiral inductors. Coil numbers (a) N=2.5, (b) N=3.5, (c) N=4.5, (d) N=5.5

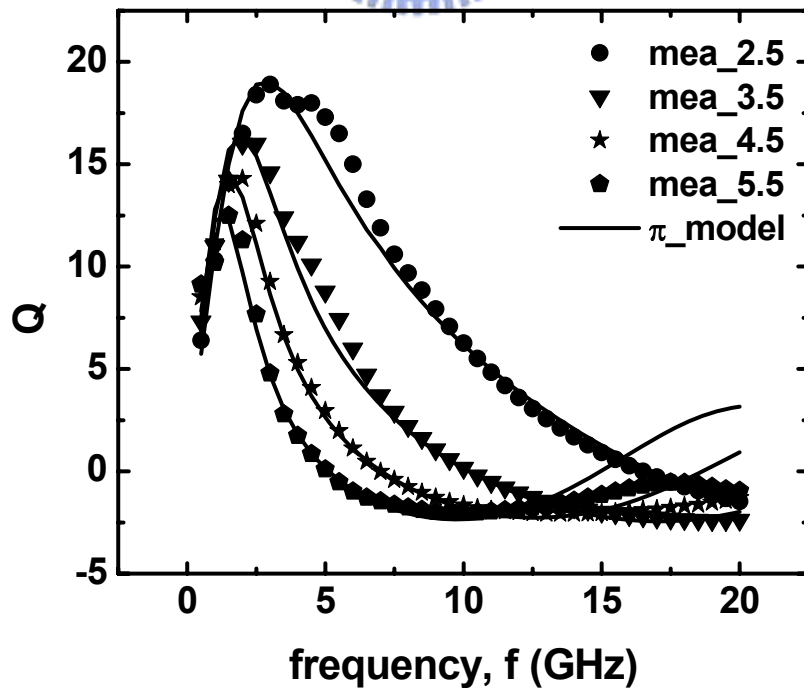


Figure 2.9 Comparison of  $Q(\omega)$  between  $\pi$ -model simulation and measurement for

spiral inductors. Coil numbers (a)  $N=2.5$ , (b)  $N=2.5$ , (c)  $N=3.5$ , (d)  $N=4.5$

## 2.2.2 Scalability and geometries of validity

There are various geometries available for a monolithic inductor to be implemented, e.g. rectangular, hexagonal, octagonal, and circular as shown in figure 2.10.

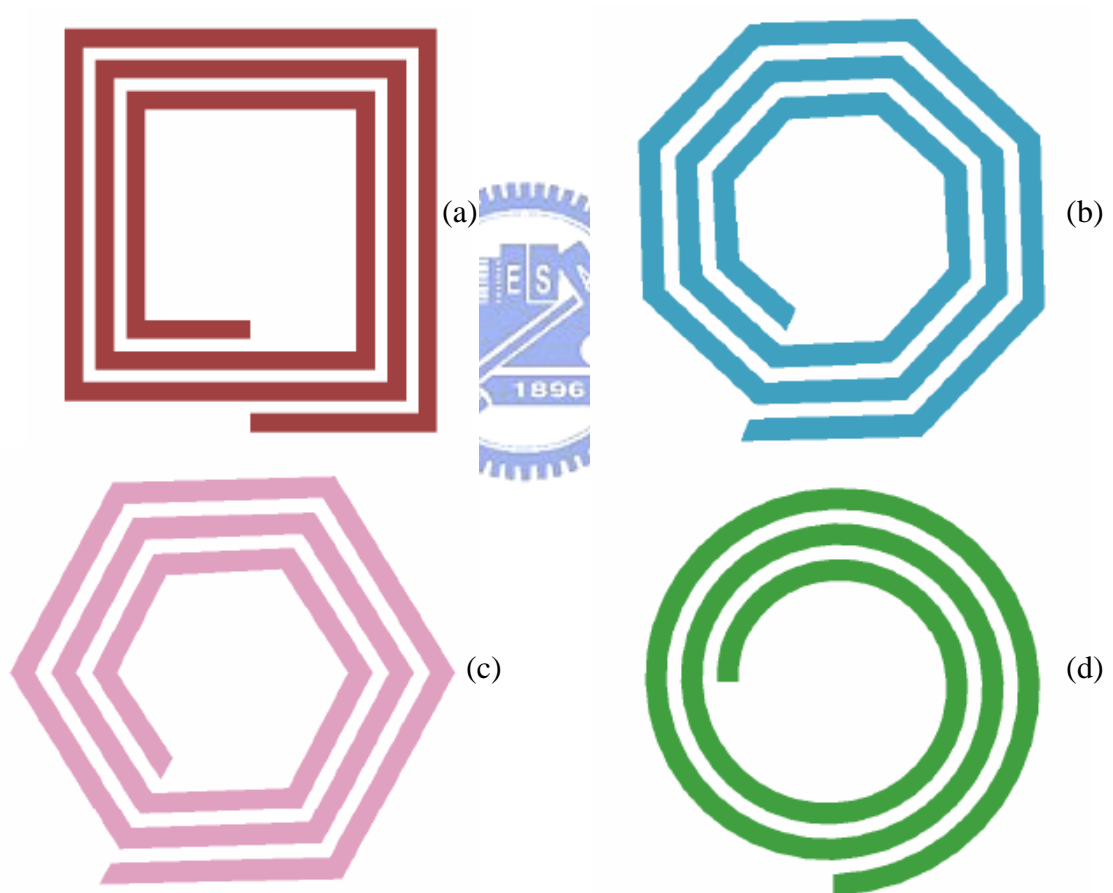
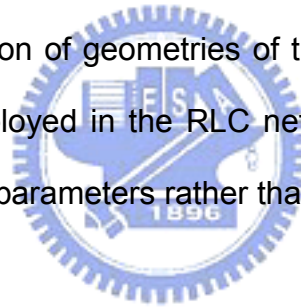


Figure 2.10 Spiral inductor geometries.

Electromagnetic (EM) simulation can help to verify the layout geometry effect on inductors and the results suggest that circular spiral can provide the best performance

in terms of higher quality factor and smaller chip area. The mechanism responsible for the improved performance realized by circular spiral comes from the reduced current crowding effect. The circular inductor as shown in figure 2.2 (d) can place the largest amount of conductor in the smallest possible area, reducing the series resistance and parasitic capacitance of the spiral inductors. However, one major drawback of the circular structure is its layout complexity. It is because that its metal line consists of many cells rotated with different angles. In general, specific coding is required to generate this structure by layout tools.

In fact, a good model is developed to accurately simulate the broadband characteristics of on-Si-chip for different geometries of the inductive passive components, up to 20GHz. Besides the broadband feature, scalability is justified by good match with a liner function of geometries of the inductive passive components for all model parameters employed in the RLC network. The satisfactory scalability manifest themselves physical parameters rather than curve fitting.



### **2.2.3 Model parameter extraction flow and automation**

Which a new model or a conventional model has been developed to accurately simulate the broadband characteristics, its all the unknown R, L,C parameters haven't been determined initial value. So we must establish a parameter extraction flow through equivalent circuit analysis to determine initial guess value and to enable automatic parameter extraction and optimization. All the unknown R,L,C parameters are extracted from analytical equations derived from different equivalent circuit analysis. We can use Z-matrix and /or Y-matrix to extract all parameters. Above extraction and optimization principle, we use some principle to define a set of



analytical equation from measurement and to generate all unknown parameters at the equivalent circuits. Due to the necessary approximation, the extracted R,L,C parameters in the first run of low are generally not the exactly correct solution but just serve as the initial guess or further optimization through best fitting to the measured S-parameters,  $L(\omega)$ ,  $\text{Re}(\omega)$ , and  $Q(\omega)$ .

## 2.3 Model enhancement strategies

The lack of an accurate and scalable model for on-chip inductors becomes one of the most challenging problems for Si-based RF IC design. The existing models suffer two major drawbacks in terms of accuracy for limited bandwidth and poor scalability.

Many reference publications reported improvement on the commonly adopted  $\pi$ -model by modification on the equivalent circuit schematics. However, limited bandwidth to few gigahertz remains an issue for most of the modified  $\pi$ -models. A two  $\pi$ -model was proposed to improve the accuracy of  $R(\omega)$  and  $L(\omega)$  beyond self-resonance frequency. Unfortunately, this two  $\pi$ -model suffers a singular point above resonance. Besides, the complicated circuit topology with double element number will lead to difficulty in parameter extraction and greater time consumption in circuit simulation. Recent work using modified T-model demonstrated promising improvement in broadband accuracy and suggested the advantage of T-model over  $\pi$ -model. However, the scalability of model's major concern was not presented. To solve the mentioned issues, a new T-model was proposed and developed in this work. This T-model is proposed to realize two primary features, i.e., broadband accuracy and scalability. The T-model is composed of two RLC networks to account for spiral coils, lossy substrate, and their mutual interaction. Four physical elements,  $R_s$ ,  $L_s$ ,  $R_p$  and  $C_p$  are incorporated to describe the spiral coils above Si substrate and other elements. All the physical elements are constants independent of frequencies and can

be expressed by a close form circuit analysis on the proposed T-model. Parameter extraction and optimization can be conducted with an initial guess extracted by approximation valid for specified frequency range.

All the model parameters manifest themselves with predictable scalability w.r.t. coil numbers and physical nature. A parameter extraction flow has been established to enable automatic parameter extraction and optimization that is easy to be adopted by existing circuit simulators like Agilent ADS or parameter extractor such as Agilent IC-Cap. The model accuracy over broadband is validated by good agreement with the measured S-parameters,  $L(W)$ ,  $\text{Re}(Z_{in}(W))$ , and  $Q(W)$  up to 20GHz that this scalable inductor model can effectively improve RF circuit simulation accuracy in broad bandwidth and facilitate the design optimization using on-chip inductors.



## 2.4 Fundamental of quality factor for an inductor

For an ideal inductor free from energy loss due to parasitic resistance and substrate coupling effect, the magnetic energy stored can be given by (2.1),

$$E_L = \frac{1}{2} L i_L^2 \quad (2.1)$$

Where  $i_L$  is the instantaneous current through the inductor.

From (2.1), the peak magnetic energy stored in an inductor in sinusoidal steady state is given by,

$$E_{peak \text{ inductor}} = \frac{1}{2} L |I_L|^2 = \frac{|V_L|^2}{2\omega^2 L} \quad (2.2)$$

Where  $|I_L|$  and  $|V_L|$  correspond to the peak current through and the peak voltage across the inductor.

The quality factor ( $Q$ ) of an inductor is a measure of the performance of the elements defined for a sinusoidal excitation and given by,

$$Q = 2\pi \frac{\text{energy stored}}{\text{energy loss per cycle}} = \omega \frac{\text{energy stored}}{\text{average power loss}} \quad (2.3)$$

The above definition is quite general which causes some confusion. However, in the case of an inductor, energy stored refers to the net peak magnetic energy.

To illustrate the determination of  $Q$ , consider an ideal inductor in series with a resistor in Figure 2.11. This models an inductor with resistance in the winding.

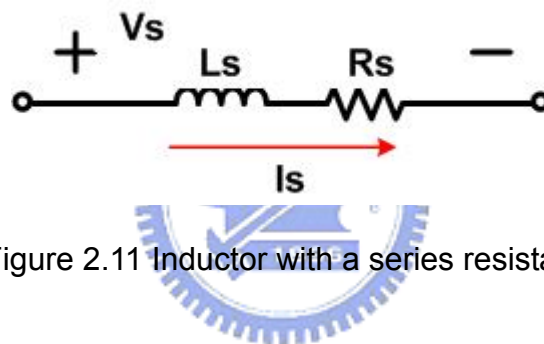


Figure 2.11 Inductor with a series resistance

Since the current in both elements is equal, we use the equation for the peak magnetic energy in terms of current given in (2.2) to write,

$$\begin{aligned} Q &= 2\pi \frac{\text{peak magnetic energy stored}}{\text{energy loss per cycle}} \\ &= 2\pi \frac{\frac{1}{2} |I_s|^2 L_s}{\frac{1}{2} |I_s|^2 R_s \tau} = \frac{\omega L_s}{R_s} \end{aligned} \quad (2.4)$$

where

$$\frac{2\pi}{\tau} = \omega$$

Where  $\tau$  is the period of the sinusoidal excitation

Note that the quality factor of an inductor with a lossy winding increases with frequency. Also note that as the resistance in the inductor decreases, the quality of the inductor increases and in the limit  $Q$  becomes infinite since there is no loss. Using the above procedure, the quality factor of another pure lossy inductor can be determined. We repeat the detail in the following.

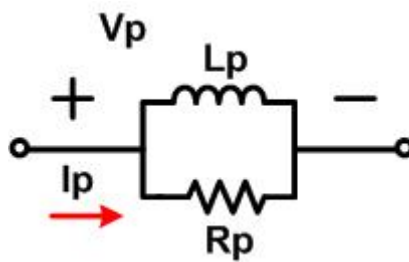


Figure 2.12 Inductor with a parallel resistance.

Since the voltage in both elements is equal, we use the equation for the peak magnetic energy in terms of voltage given in (2.2) to write,

$$\begin{aligned}
 Q &= 2\pi \frac{\text{peak magnetic energy stored}}{\text{energy loss per cycle}} \\
 &= 2\pi \frac{\frac{|V_p|^2}{2\omega^2 L_p}}{\frac{|V_p|^2}{2\omega^2 R_p} \tau} \\
 &= \frac{R_p}{\omega L_p}
 \end{aligned} \tag{2.5}$$

Where  $\tau$  is the period of the sinusoidal excitation

The definition of quality factor is general in the sense that it does not specify what stores or dissipates the energy. The subtle distinction between an inductor and an LC tank Q lies in the intended form of energy storage. For example, only the magnetic energy stored is of interest and any electric energy stored because of some inevitable parasitic capacitance in a real inductor is counterproductive. Therefore, the Q of an inductor is proportional to the net magnetic energy stored and is given by,

$$\begin{aligned}
 Q_{inductor} &= 2\pi \frac{\text{peak magnetic energy stored}}{\text{energy loss per cycle}} \\
 &= 2\pi \frac{\text{peak magnetic energy stored} - \text{peak electric energy}}{\text{energy loss per cycle}} \quad (2.6)
 \end{aligned}$$

An inductor is said to be self-resonant when the peak magnetic and electric energies are equal. Therefore, Q of an inductor vanishes to zero at the self-resonant frequency. At frequencies above the self-resonant, no net magnetic energy is available from an inductor to any external circuit. In contrast, for an LC tank, the Q is defined at the resonant frequency  $\omega_o$ , and the energy stored term in the expression for Q given by (2.3) is the sum of the average magnetic and electric energy. Since at resonance the average magnetic and electric energies are equal, so we have,

$$\begin{aligned}
 Q_{inductor} &= 2\pi \frac{\text{average magnetic energy} + \text{average electric energy}}{\text{energy loss per cycle}} \Bigg|_{\omega=\omega_o} \\
 &= 2\pi \frac{\text{peak magnetic energy}}{\text{energy loss per cycle}} \Bigg|_{\omega=\omega_o} = 2\pi \frac{\text{peak electric energy}}{\text{energy loss per cycle}} \Bigg|_{\omega=\omega_o} \quad (2.7)
 \end{aligned}$$

The average magnetic or electric energy at resonance for sinusoidal excitation is

$\frac{1}{4}L|I_L|^2 = \frac{1}{4}C|V_c|^2$  which are half the peak magnetic energy given by (2.2) Lets

look at the parallel RLC circuit of figure 2.5 to clarify its inductor and tank Q.

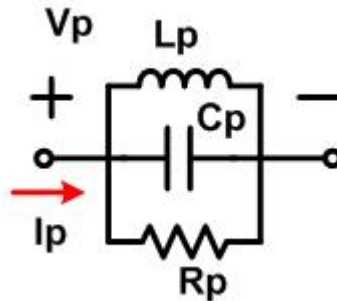


Figure 2.13 Parallel RLC circuit.

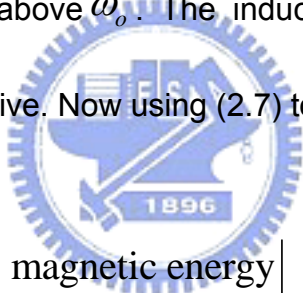
The quality factor of the inductor is calculated as follows,

$$\begin{aligned}
 Q_{inductor} &= 2\pi \frac{\text{peak magnetic energy} - \text{peak electric energy}}{\text{energy loss per cycle}} \\
 &= 2\pi \frac{\frac{|V_p|^2}{2\omega^2 L_p} - \frac{1}{2} C_p |V_p|^2}{\frac{|V_p|^2}{2R_p} T} = \frac{1}{\omega L_p - \omega C_p} \\
 &= \frac{R_p}{\omega L_p} \left\{ 1 - \left( \frac{\omega}{\omega_0} \right)^2 \right\}
 \end{aligned} \tag{2.8}$$

where the resonant frequency  $\omega_0 = \frac{1}{\sqrt{L_p C_p}}$ .

Here  $\frac{R_p}{\omega L_p}$  accounts for the magnetic energy stored and ohmic loss of the parallel resistance in figure 2.4. The second term in equation 2.8 is the self-resonance factor describing the reduction in Q due to the increase in the peak electric energy with

frequency and the vanishing of Q at the self-resonant frequency. In the parallel RLC circuit,  $V_L = V_C = V_P$  which is depicted in the figure 2.5. Note that in each quarter cycle, when energy is being stored in the inductor, it is being released from the capacitor and vice versa. As  $\omega$  increases, the magnitude of  $I_L$  decreases while the magnitude of  $I_C$  increases until they become equal at the resonant-frequency  $\omega_0$ , so that an equal amount of energy is being transferred back and forth between the inductor and capacitor. At this frequency,  $Q_{inductor}$  given by equation 2.8 is zero. As  $\omega$  increases above  $\omega_0$ , the magnitude of  $I_L$  becomes increasingly more negative. That is, as the previous mention, no net magnetic energy is available from an inductor to any external circuit at frequency above  $\omega_0$ . The inductor is capacitive in nature, and  $Q_{inductor}$  given by (2.8) is negative. Now using (2.7) to calculate the tank Q we have



$$\begin{aligned}
 Q_{\text{tank}} &= 2\pi \frac{\text{peak magnetic energy}}{\text{energy loss per cycle}} \Bigg|_{\omega=\omega_0} \\
 &= 2\pi \frac{\frac{|V_p|^2}{2\omega^2 L_p}}{\frac{|V_p|^2}{2R_p} T} \Bigg|_{\omega=\frac{1}{\sqrt{L_p C_p}}} = \frac{R_p}{\sqrt{\frac{L_p}{C_p}}} = \omega_0 R_p C_p \quad (2.9)
 \end{aligned}$$

Note that the tank Q isn't zero unlike the inductor Q which is zero at resonance. Also, note that the same result can be derived using the ratio of the resonant-frequency to -3 dB bandwidth as follows,

$$\begin{aligned}
 Q_{\text{tank}} &= \left. \frac{f}{BW_{-3dB}} \right|_{f=f_o} \\
 &= \left. \frac{f}{\frac{1}{2\pi R_p C_p}} \right|_{f=\frac{1}{2\pi\sqrt{L_p C_p}}} = \frac{R_p}{\sqrt{\frac{L_p}{C_p}}} \omega_0 R_p C_p \quad (2.10)
 \end{aligned}$$

(2.9) and (2.10) are the same as we expect.

Both Q definitions discussed above are important, and their applications are determined by the intended function in a circuit. While evaluating the quality of on-chip inductors as a single element, the definition of inductor quality given by (2.6) is more appropriate. However, if the inductor is being used in a tank, the definition given by (2.7) is more appropriate.

Figure 2.6 shows a real inductor can be replaced by a parallel RLC circuit of  $\pi$ -model.

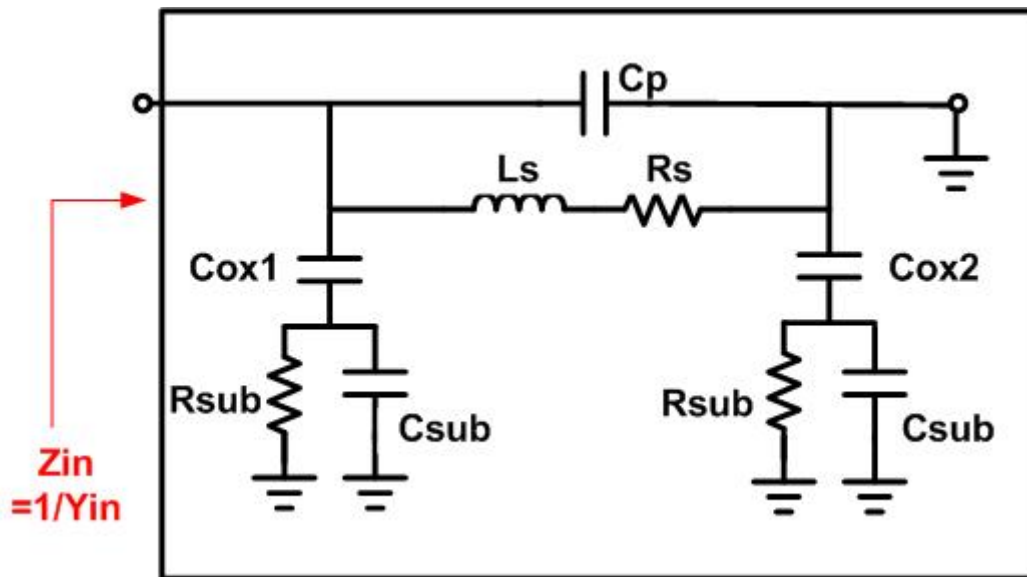


Figure 2.14 Alternative method for determining the Q in real inductors.

In contrast with (2.8), it can be easily determined that the real inductor quality



factor of a parallel RLC circuit is given by the negative of the ratio of the imaginary part to the real part of the input admittance, namely the ratio of the imaginary part to the real part of the input impedance. The above statements are summarized in (2.11) and are appropriate for determining the Q of inductors from simulation or measurement results.

$$Q_{\text{tank}} = \frac{\text{Im}\{Z_{in}\}}{\text{Re}\{Z_{in}\}} = -\frac{\text{Im}\{Y_{in}\}}{\text{Re}\{Y_{in}\}} \quad (2.11)$$



# Chapter 3

## Broadband and Scalable On-chip Inductor Model

### 3.1 Broadband accuracy for on-chip inductors

In silicon-based radio-frequency (RF) integrated circuits (ICs), on chip spiral inductor are widely used due to their low cost and ease of process integration. As a necessary tool for circuit design, equivalent circuit models of spiral inductors, using lumped RLC elements, efficiently represent their electrical performance for circuit simulation with other design components. Compared with the generic 3D electromagnetic field solver (e.g., HFSS) or other 2.5D electromagnetic field solver (e.g., ADS Momentum), a lumped equivalent-circuit model dramatically reduces computation time and supports rapid performance optimization. On the other hand, model inaccuracy, which stems from the complexity of on-chip inductor structures and high-frequency phenomena, presents one of the most challenging problems for RF IC designers.

Current equivalent-circuit approaches simply represent the inductor as a lumped circuit and  $\pi$ -model is one of examples.  $\pi$ -model includes series metal resistance and inductance, feedthrough capacitance, dielectric isolation, and substrate effects. A physical model is proposed to capture the high-frequency behavior as shown in Fig. 3.1. Herein, the spiral inductor was built on Si substrate where the high-frequency behavior is complicated due to semi-conducting substrate nature. The conventional  $\pi$ -model reveals limitation in broadband accuracy due to some neglected effects such as eddy current on substrate. In order to overcome this disadvantage, 3D EM

simulation was done using HFSS to investigate the lossy substrate effect. Following the HFSS simulation results, a new T-model has been developed to accurately simulate the broadband characteristics of on-Si-chip spiral inductors, up to 20 GHz.

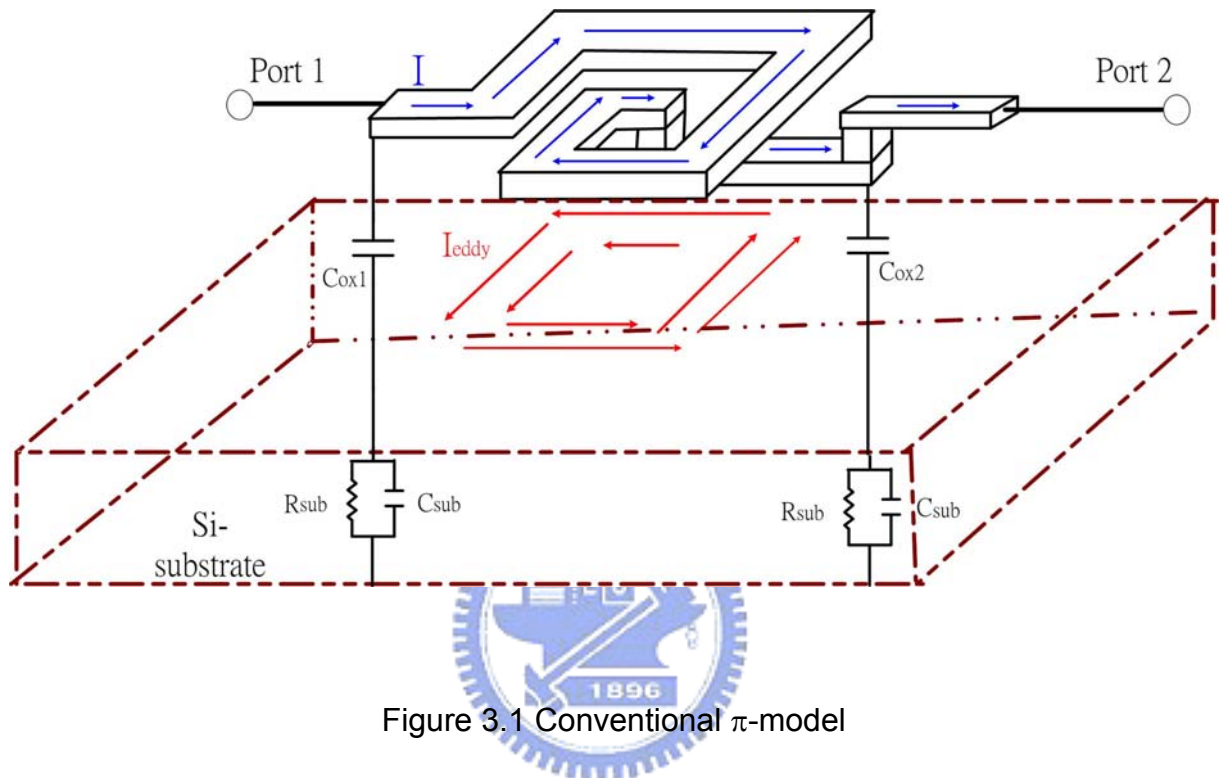


Figure 3.1 Conventional  $\pi$ -model

### 3.1.1 Simulation tool and simulation method

Some electromagnetic (EM) field simulators are used, like sonnet, microwave office, HFSS and ADS Momentum to predict the component characteristics such as S-parametera, quality factor, and self-resonant frequency. However, we found that the simulation time of HFSS for 3D is slower than the others. Because it can estimate the magnetic substrate eddy current effect, we can obtain more accurate S-parameter. ADS Momentum EM simulation is a planar full-wave EM solver that can calculate the fields in the substrate and the dielectric and spend less time, but this simulation tools for 2.5D is less accurate than HFSS. Thus, the capacitance between the spiral windings and the eddy current in the windings are not modeled. The advantage of

these EM simulators is that they can report their simulation results in S-parameters. These results can then be numerically fitted to the circuit model. But in general, it is desirable to simulate circuits with these components by directly using the S-parameters extracted from the EM simulator or measured from the instruments. This is because a number of the component values in this circuit model vary with frequency due to the skin effect, substrate loss and so on.

For the mentioned reason, the fast and adequately accurate simulation program is strongly demanded. In order to predict the frequencies corresponding to  $Q_{\max}$  and self-resonance ( $f_{SR}$ ), the amount of the parasitic capacitance should be predicted accurately. Due to the requirement, we select HFSS for EM simulation and analysis in this work.

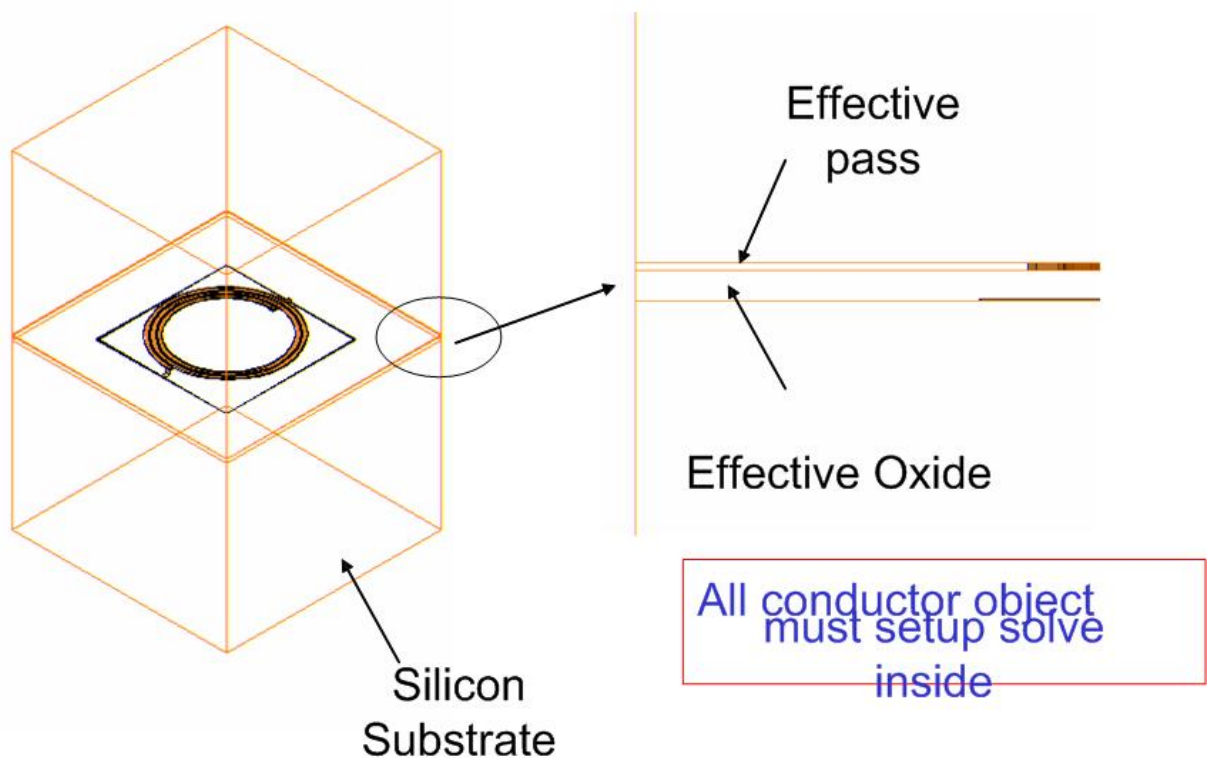


Figure 3.2 layer stackup simulation by HFSS

Spiral inductors were fabricated by 0.13 $\mu\text{m}$  back end technology with eight layers of Cu and low-k inter-metal dielectric ( $k=3.0$ ). The top metal of 3 $\mu\text{m}$  Cu was used to implement the spiral coils of width fixed at 15 $\mu\text{m}$  and inter-coil space at 2 $\mu\text{m}$ . The inner radius is 60 $\mu\text{m}$  and outer radius is determined by different coil numbers  $N=2.5, 3.5, 4.5, 5.5$  for this topic. The physical inductance achieved at sufficiently low frequency are around 1.96~8.66nH corresponding to coil numbers  $N=2.5\sim 5.5$ . S-parameters were measured by using Agilent network analyzer up to 20 GHz and de-embedding was carefully done to extract the truly intrinsic characteristics for model parameter extraction and scalable model build up. In Figure 3.2, it is clear that HFSS simulation environment is a solid structure. In HFSS simulation window, it can't simulate 0.13 $\mu\text{m}$  back end technology with eight layers of Cu and low-k inter-metal dielectric ( $k=3.0$ ), so we must make some modifications for simulation setup.

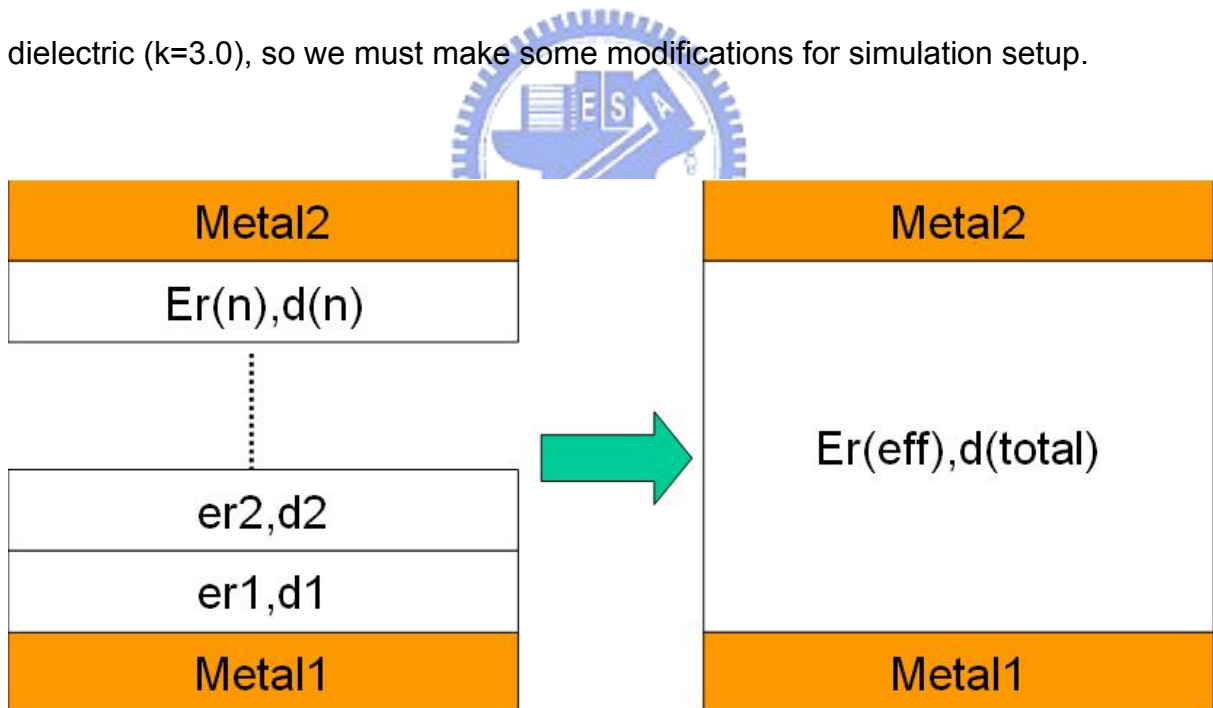


Figure 3.3 effective oxide dielectric constant equivalents from M1 to M2

From Figure 3.3, we give an example for dielectric constant equivalent from Metal-1 to Metal-2. In 0.13 $\mu\text{m}$  back end technology, the inter-metal dielectrics is a complex layer structure of various dielectric constants. In order to simplify these layers, we make two

series capacitances be equal to one capacitance. We use above theory to extend complex type and show the formula as follows

$$D_{eff} = \sum_{i=1}^n d_i \quad (3.1)$$

$$\epsilon_{r,eff} = D_{eff} \times \left( \sum_{i=1}^n \frac{d_i}{\epsilon_{ri}} \right)^{-1} \quad (3.2)$$

Where  $\epsilon_r$  is relative permittivity and  $d_i$  is thickness

In the layout of the inductor, to prevent flux radiation to cause flux degradation in the center area, we generally plot ground ring to protect flux radiation. As shown in Fig 3.4, in order to simulate ground ring by HFSS, we could setup ground ring material for PEC to decrease the loss. Adopting the described simulation method, we will discuss T-model build-up for single-end spiral inductor in the next section.

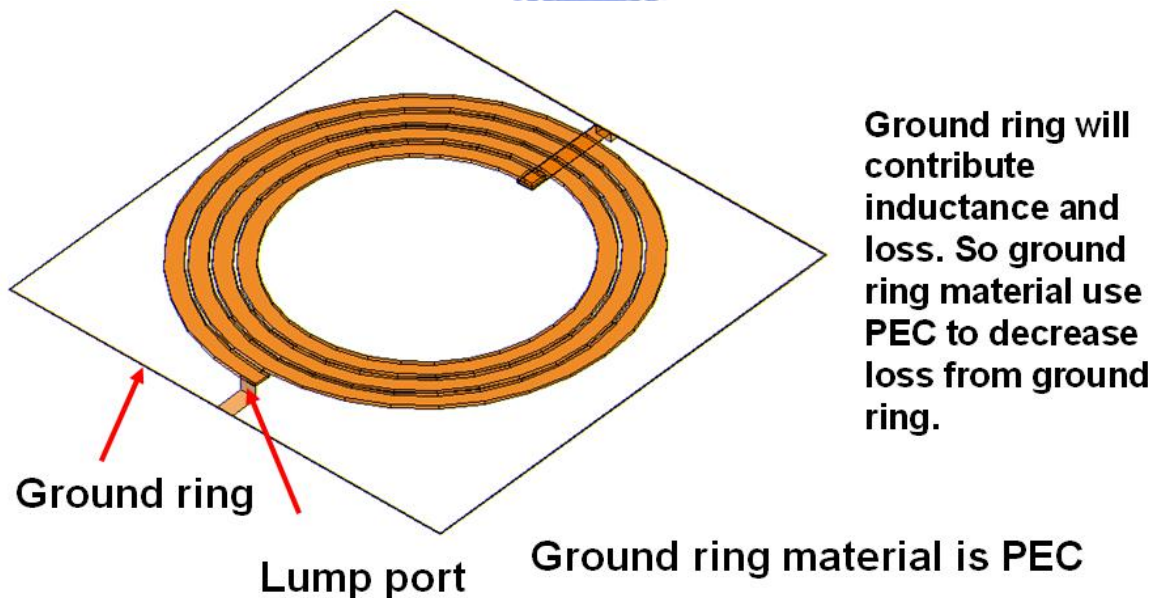


Figure 3.4 Ground ring setup by HFSS

### 3.1.2 Conductor and substrate loss effect – model and theory

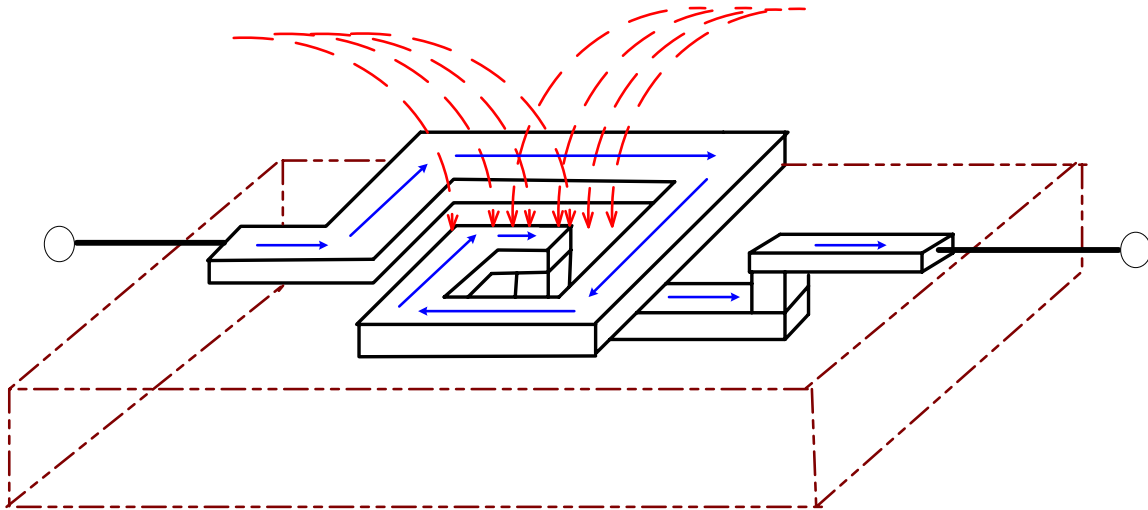


Figure 3.5 Layout of convention single-end spiral inductor

There are several sources of loss in a single-end inductor. The DC resistance of single-end inductor is easily calculated as the product of this sheet resistance and the number of squares in the strip. However, at higher frequencies the resistance of the strip increases due to the skin effect and current crowding. Moreover, substrate losses increase with frequency due to the dissipative currents that flow in the silicon substrate. According to Maxwell equation, there are two different mechanisms that cause the induction of these loss effects. One is the capacitive coupling between the strip and the substrate induces displacement current, namely electric substrate losses. The other is the magnetic is the magnetic coupling caused by the time varying magnetic field linked to the strip induces eddy currents under the strip and in the inner turns of the strip, namely magnetic substrate losses. From (3.3) and (3.4) of Maxwell equation, we can show above theory.

Port 1

$$\nabla \times \vec{E} = -\frac{\partial \vec{B}}{\partial t} \quad (3.3)$$

$$\iint \nabla \times \vec{E} \cdot d\vec{S} = -\frac{\partial}{\partial t} \iint \vec{B} \cdot d\vec{S} \quad (3.4)$$

$$\oint_c \vec{E} \cdot d\vec{\ell} = -\frac{\partial \Phi}{\partial t}$$

Figure 3.5 show the electric and magnetic substrate losses of single-end spiral inductor. The magnetic field  $\vec{B}(t)$  extends around the windings and into the substrate. Faraday's Law states that this time-varying magnetic field will induce an electric field in the substrate. This field will force an image current to flow in the substrate in opposite direction of the current in the winding directly above it. The magnetic field will not only penetrate into the substrate but also into the other windings of the coil. The effect causes the inner turns of the strip to contribute much more loss to the inductor while having a minimal impact on the actual inductance. This phenomenon is sometimes referred to as current crowding.

For on-chip single-end spiral inductors, the line segments can be treated as microstrip transmission lines. In this case, the high frequency current recedes to the bottom surface of the wire, which is above the ground plane. Please see figure 3.6.

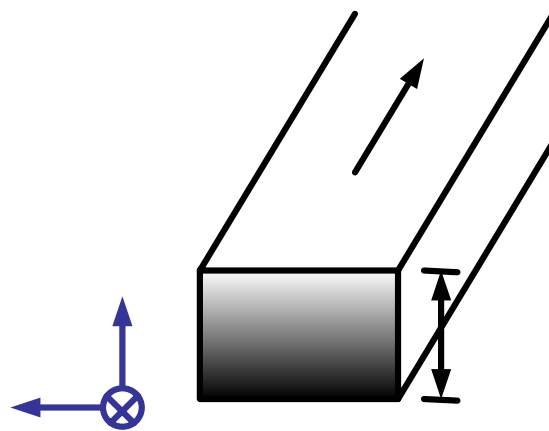


Figure 3.6 cross section for single-end spiral inductor coils



The attenuation of the current density ( $J$  in  $A/m^2$ ) as a function of distance ( $y$ ) away from the bottom surface can be represented by the function

$$J = J_o \times e^{-\frac{y}{\delta}} \quad (3.5)$$

The skin depth ( $\delta$ ) shows below equation 3.6

$$\delta = \sqrt{\frac{2}{\omega\mu\sigma}} \quad (3.6)$$

The current ( $I$  in A) is obtained by integrating  $J$  over the wire cross-sectional area. Since  $J$  only varies in the  $y$  direction,  $I$  can be calculated as

$$\begin{aligned} i &= \int_s \vec{J} \cdot d\vec{S} \\ &= \int_0^d J_o \times e^{-\frac{y}{\delta}} \times w \cdot dy \\ &= J_o w \delta (1 - e^{-\frac{d}{\delta}}) \end{aligned} \quad (3.7)$$

Where  $d$  is the physical thickness of the wire. The last term in equation 3.6 can be defined as an effective thickness

$$d_{eff} = \delta (1 - e^{-\frac{d}{\delta}}) \quad (3.8)$$

The dc series resistance,  $R_{DC}$ , can be expressed as

$$R_{DC} = R_{sh} \frac{l}{w} \quad (3.9)$$

The series resistance,  $R_s$ , can be expressed as

$$R_s = \frac{l}{\sigma w \delta (1 - e^{-\frac{d}{\delta}})} \quad (3.10)$$

We can use Taylor's expansion, so we can obtain  $R_s = R_{DC}$  at the low frequencies. At the higher frequencies, we will include skin effect depended on

frequency in the (3.10).

Regarding to substrate effect, we use 3D simulation tools, for example, HFSS to simulate current flow direction on the substrate surface to verify above theory. The simulated current flow expressed by vectors is shown in figure 3.7

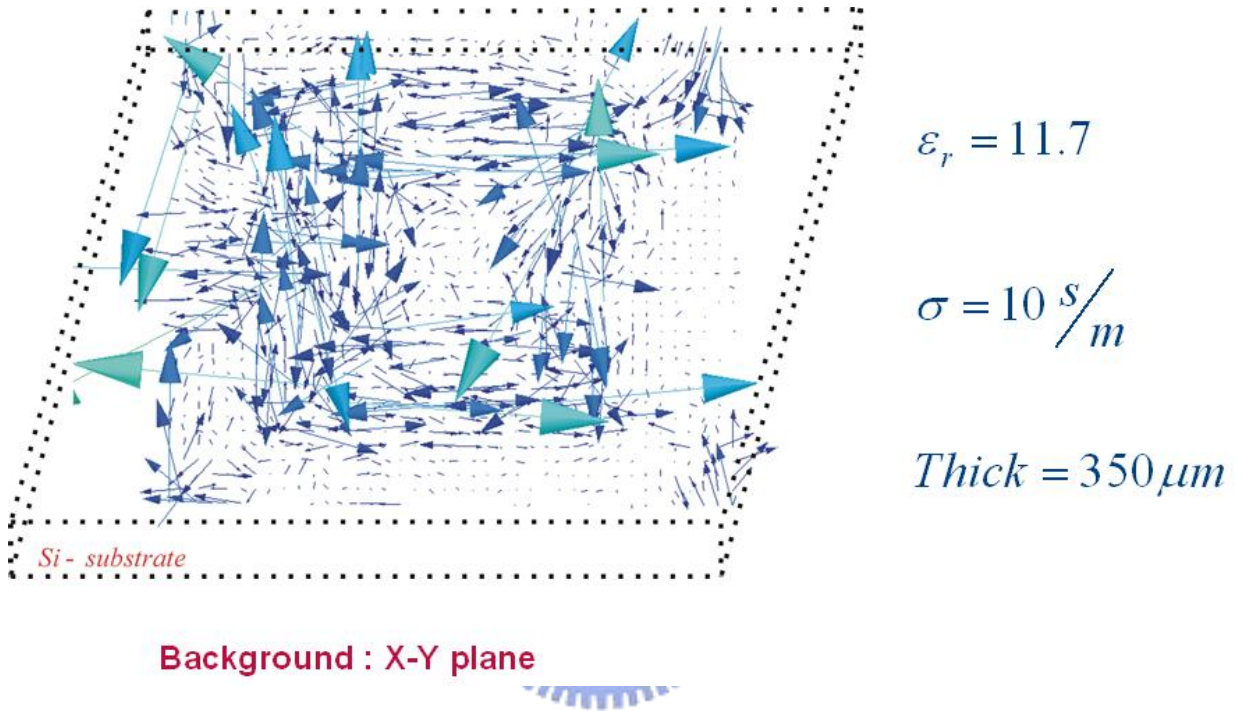


Figure 3.7 simulate eddy current on the substrate surface by HFSS

Figure 3.7 indicates that the eddy current on the Si substrate flows in the opposite direction w.r.t that of spiral coils. According to Faraday's Law states that this time-varying magnetic field will induce an electric field in the substrate and generate a current on the substrate surface. But in the interior substrate also is generated, we also obtain result from 3D simulation tools by HFSS. From figure 3.8, we find current generated in the interior substrate. This effect also causes Q degeneration of the single-end spiral inductors. In order to decrease magnetic field coupling to substrate, we usually use pattern ground shield at the lower metal and increase Q value.

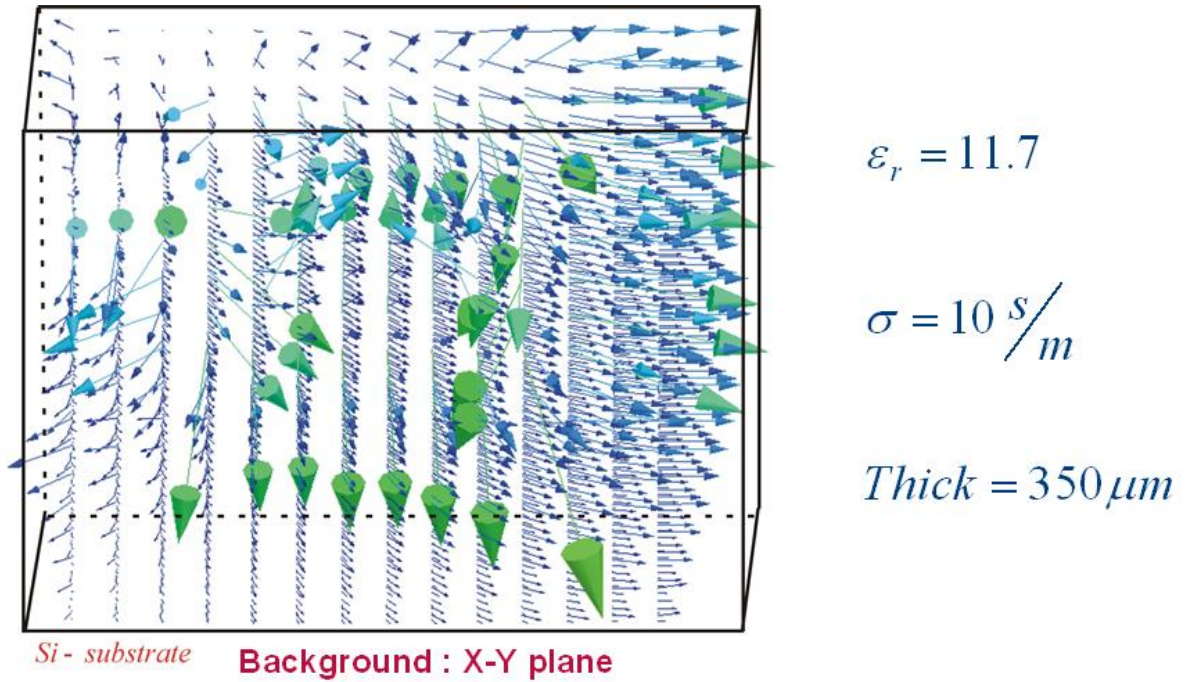


Figure 3.8 simulate eddy current in the interior substrate surface by HFSS



According to above method, we will present a new T-model developed to accurately simulate the broadband characteristics of single-end spiral inductors. In figure 3.9, we integrate all physic parameters and obtain a compact model. Please see figure 3.9, and we will use equivalent circuit to analysis in the next section.

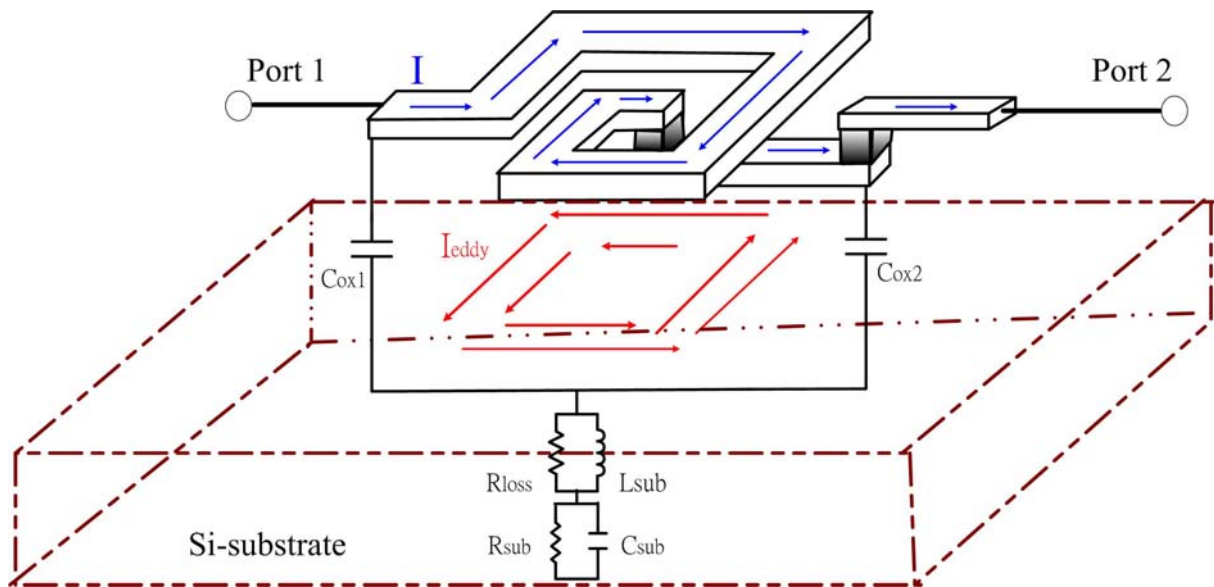
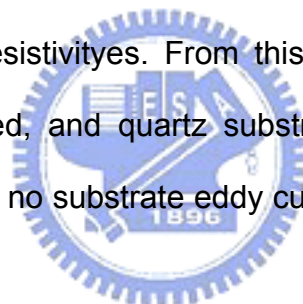


Figure 3.9 Simplified illustration of T-model

### 3.1.3 Varying substrate resistivity effect – model and theory

On-chip passive components are imperative for silicon-based RF IC's. The detrimental effects of the semi-conducting substrate parasitics on metal-insulator-metal capacitors, bond pad single spiral inductors. However, the basic understanding of the physics behind these effects is still not well known. In the current process technology, heavily doped substrates, also known as “epi” substrates, are routinely employed in CMOS and BICMOS processes while lightly doped ( $1\text{-}30\ \Omega\text{-cm}$ ) substrate are commonly used in bipolar and some CMOS technologies. Typical epi substrate consist of a lightly doped ( $1\text{-}30\ \Omega\text{-cm}$ ) epitaxial layer grown on a degenerately doped ( $10\text{-}20\ \text{m}\Omega\text{-cm}$ ) bulk substrate. The substrate effects on the performance of single-end spiral inductors are critical to silicon RF IC's. Based on ADS Momentum simulation results and physical modeling, we present an extensive study on the substrate parasitic. So we will create a broadband and scalable model developed to accurately simulate on-chip inductors of various dimensions and substrate resistivities. The 3D eddy current is identified as key element essential to accurately simulate

broadband characteristics. EM simulation using ADS Momentum is conducted to predict the on-chip inductor performance corresponding to wide range of substrate resistivity ( $\rho_{si} = 0.05 \sim 1K\Omega$ ). Three operation models such as TEM, slow wave, and eddy current are presented. The model parameters manifest themselves physics-base through relevant correlation with  $\rho_{si}$  over three operation modes. The onset of slow-wave mode can be consistently explained by a key element introduced in improve T-model, which accounts for the conductor loss due to eddy current arising from magnetic field coupling through substrate return path. It can facilitate optimization design of on-chip inductors through physics-based model parameters relevant to varying substrate resistivities. We find one reference to explain physic behind, but it is based on measurement result and presented. We use above result to research varying substrate resistivities. From this reference, the single-end spiral inductors on epi, lightly doped, and quartz substrates are presented. The quartz sample serves as a control for no substrate eddy current can be induced in dielectric.



In Table

<b>Sample</b>	$L_{LF}$	$R_{dc}$	<b>Substrate Description</b>
<b>Epi5nH</b>	5.3 nH	3.0 $\Omega$	4.1 $\mu\text{m}$ ox. on epi on p+ Si
<b>Epi10nH</b>	10.5 nH	7.0 $\Omega$	4.1 $\mu\text{m}$ ox. on epi on p+ Si
<b>Ld8nH</b>	8.1 nH	5.0 $\Omega$	5.6 $\mu\text{m}$ ox. on 19 $\Omega\text{-cm}$ Si
<b>Gp8nH</b>	7.9 nH	5.0 $\Omega$	5.2 $\mu\text{m}$ ox. on ground plane
<b>Qz8nH</b>	7.9 nH	5.0 $\Omega$	2.1 $\mu\text{m}$ ox. on quartz

Table Summary of spiral inductors from reference paper

From reference paper, inductor Gp8nH is fabricated with a 0.32- $\Omega$ /sq aluminum

solid ground plane (SGP) underneath the inductor to deliberately create eddy current. The SGP sheet resistance is adjusted to be similar to that of the  $p^+$  bulk comparing the inductors on epi substrate to the ones on quartz and SGP, the significance of the substrate eddy current in the  $p^+$  bulk can be evaluated. For comparison purposes, the inductors are designed to have similar low-frequency L/R ratio ( $L_{LF}/R_{dc}$ ) of approximately 1.6nH/ $\Omega$ . Inductance, parasitic resistances and capacitances, and Q are extracted from measured two-port S parameters using the techniques. We list reference paper data in Figure 3.9 and 3.10. We find Ld8nH and Qz8nH have the same series inductance and resistance indicating that the substrate eddy current is insignificant for the lightly doped substrate as expected.

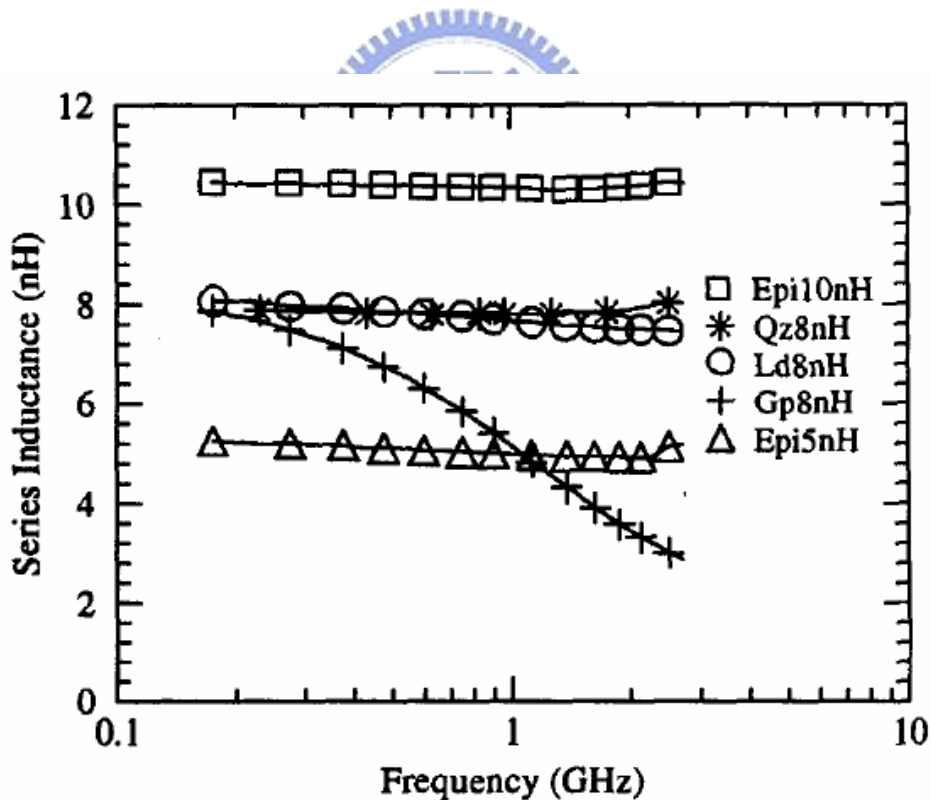


Figure 3.9 Measured inductor series inductance.

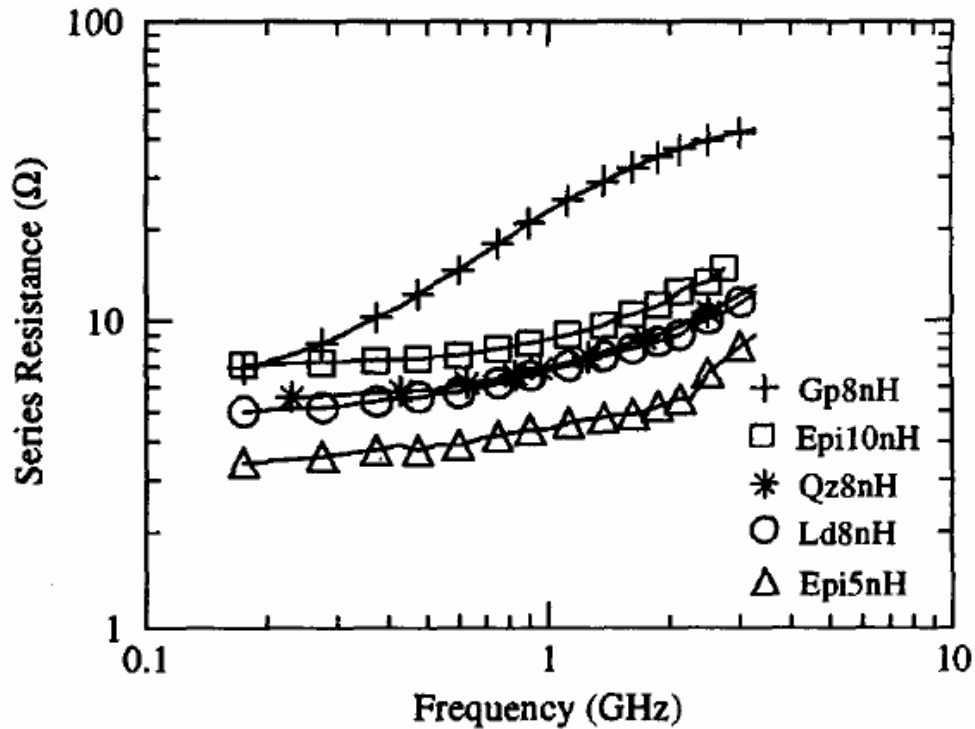


Figure 3.10 Measured inductor series resistance.

Gp8nH exhibits much lower inductance and higher resistance owing to the eddy current in the SGP. For the inductors on epi substrates, Epi5nH and Epi10nH manifest the same kind of frequency behavior for the inductance and resistance as those on lightly doped and quartz substrate, proving that eddy current in the epi substrate is negligible up to several giga-hertz. Although the  $p^+$  bulk are distributed over a much larger volume and hence they are effectively much farther away from the inductor. As a result, no significant eddy current can be induced. In this reference, it provides about different measurement Q of the substrate in Figure 3.11.

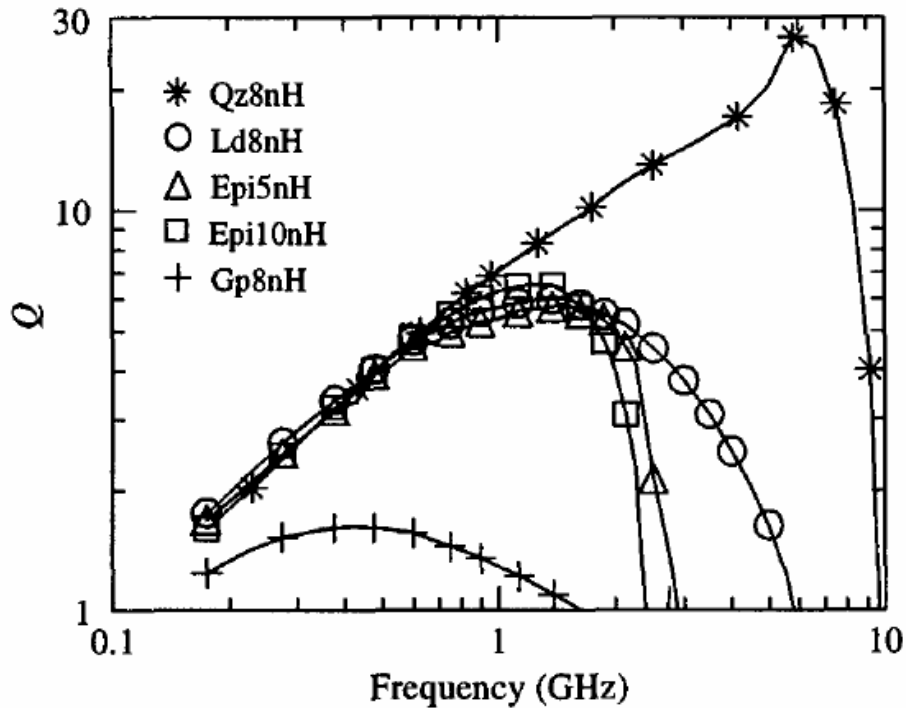
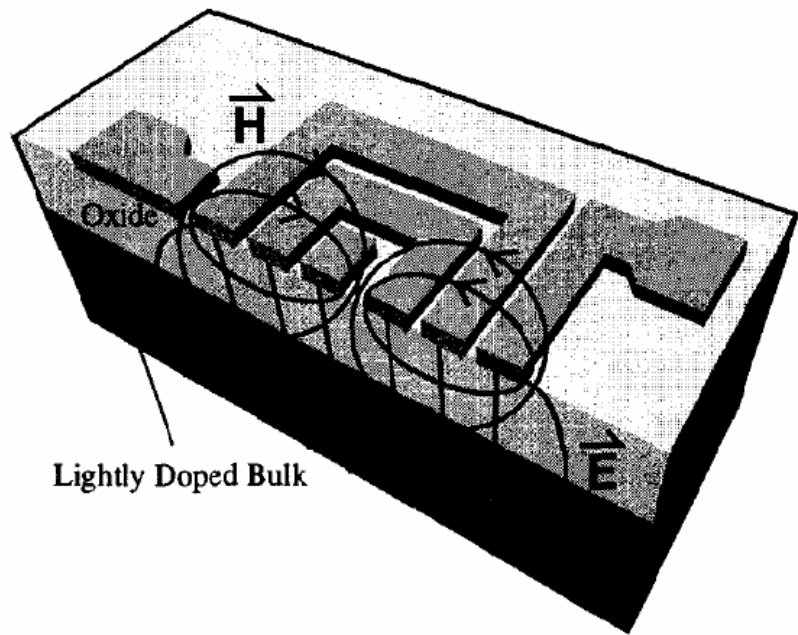


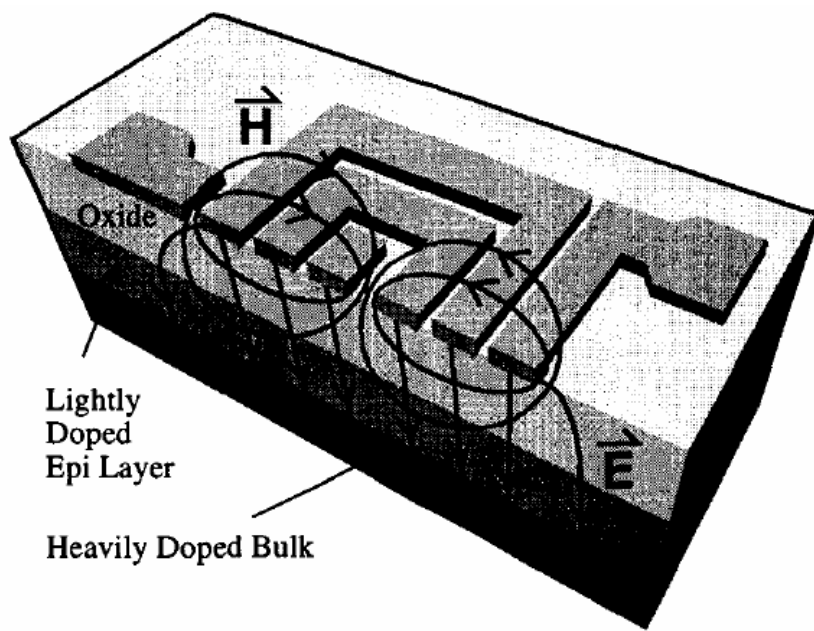
Figure 3.11 Measured inductor Q

As a result, no significant eddy current can be induced. Qz8nH has the highest Q because it has the lowest substrate loss and the smallest parasitic capacitance. Gp8nH has the worst Q due to the eddy current which leads to decrease in inductance and increase in resistance. The maximum Q for inductors on lightly doped and epi substrates are similar; however, the epi causes have a lower self-resonant frequency because of a larger substrate capacitance. While eddy current of the substrate is insignificant, ohmic loss in the resistive epi layer caused by electric field penetration is presented. In this reference paper, the loss can be eliminated by using a patterned ground shield (PGS) as depicted in Figure 3.12.

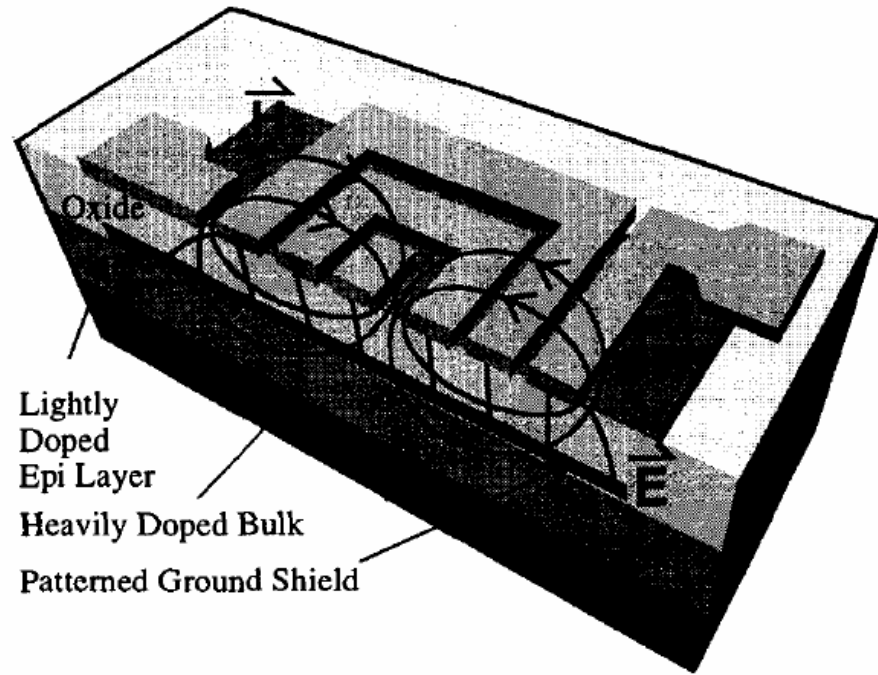




(a)



(b)



(c)

Figure 3.12 Cut-away view of the electromagnetic fields associated with single-end spiral inductor on (a) lightly doped substrate, (b) epi substrate, and (c) epi substrate with PGS. PGS terminates the electric field but allows the magnetic field to penetrate through.

Substrate effects pertaining to on-chip passive components are investigated experimentally. The results demonstrate that energy dissipation, which degrades  $Q$ , occurs predominately in epitaxial layer for epi substrates and in the bulk for lightly doped substrates. For inductive components, substrate eddy currents are shown to be negligible even in high resistivity substrate up to several giga-hertz. We will use above concepts, and simulate varying substrate resistivities to verify this section. In order to verify them, we extract all parameters to compare different substrate resistivities causing result. In the next, we will list different discusses to verify it. We will create a broadband and scalable model developed to accurately simulate on-chip inductors of various dimensions and substrate resistivities. We show the broadband

accuracy proven over frequencies up to 20 GHz, beyond resonance. In figure 3.13, it is presented my equivalent circuit model.

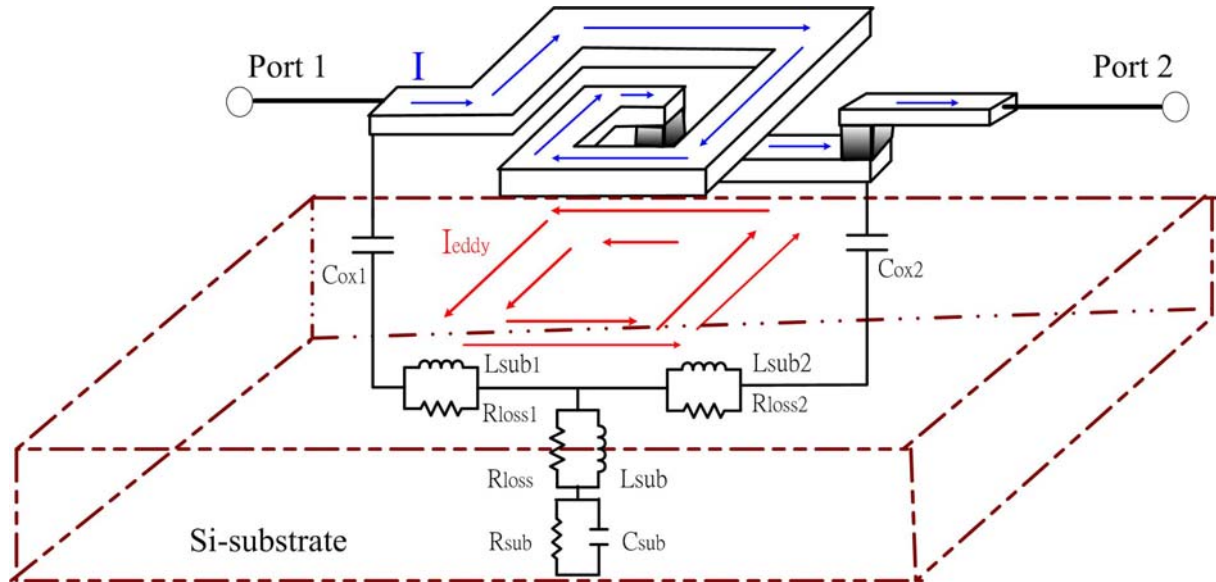


Figure 3.13 Simplified illustration of improve T-model



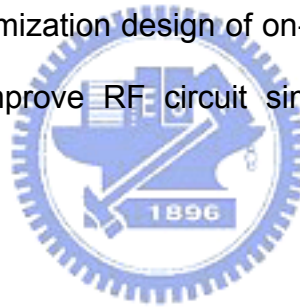
### 3. 2 Scalability for single – end spiral inductors

The rapid growth of the wireless communication market has fueled the demand for low-cost radio systems on a chip. Traditionally, radio systems are implemented a large number of discrete components. In RF circuit design, the designers need accuracy model to simulate different RF circuit for example RFMOS or passive components. In order to satisfy above necessary, the process foundry provides model and layout. But the designers usually need smaller inductances to generate broadband circuit and to achieve circuit performance. Besides, we will create scalable inductor model facilitating optimization design of on-chip spiral inductor and accuracy proven up to 20GHz can improve RF circuit simulation accuracy demanded by

broadband design.

### **3.2.1 Layout parameter and geometry effect**

The rapid growth of the wireless communication market has fueled the demand for low-cost radio systems on a chip. Traditionally, radio systems are implemented a large number of discrete components. In RF circuit design, the designers need accuracy model to simulate different RF circuit for example RFMOS or passive components. In order to satisfy above necessary, the process foundry provides model and layout. But the designers usually need smaller inductances to generate broadband circuit and to achieve circuit performance. Besides, we will create scalable inductor model facilitating optimization design of on-chip spiral inductor and accuracy proven up to 20GHz can improve RF circuit simulation accuracy demanded by broadband design.



### **3.2.2 Conductor and dielectric material properties and RF measurement**

Spiral inductors of square coils were fabricated by 0.13 $\mu\text{m}$  back end technology with eight layers of Cu and low-k inter-metal-dielectric (IMD) ( $k=3.0$ ). The top metal of 3 $\mu\text{m}$  Cu was used to implement the single-end spiral coils of width fixed at 15  $\mu\text{m}$  and inter coil space at 2  $\mu\text{m}$ . The inner radius is 60  $\mu\text{m}$  and outer radius is determined by different coil numbers,  $N=2.5, 3.5, 4.5, 5.5$  for single-end spiral inductors. The inductances are extracted from measurement data. The physical inductance ( $L_{DC}$ ) achieved at sufficiently low frequency are around 1.96 ~8.66nH corresponding to coil

numbers  $N=2.5 \sim 5.5$ . S parameters were measured by using Agilent network analyzer up to 20 GHz and de-embedding was carefully done to extract the truly intrinsic characteristics for model parameter extraction and scalable model build up.

Moreover, in this section, we introduce RF measurement equipment for our research. In figure 3.4, it showed below illustrates our setup of RF measurement system for on-wafer RF measurement. ICCAP is the control center. ICCAP is used to send the commands to instruments (Agilent E8364B PNA, and HP4142B) and probing station is to perform the measurement for a specific DUT and to gather the measured data for extraction at different extraction flow. In inductor measurements, we only need S-parameters to extract and analysis. So HP4142B parameter analyzer isn't used for inductor measurements.

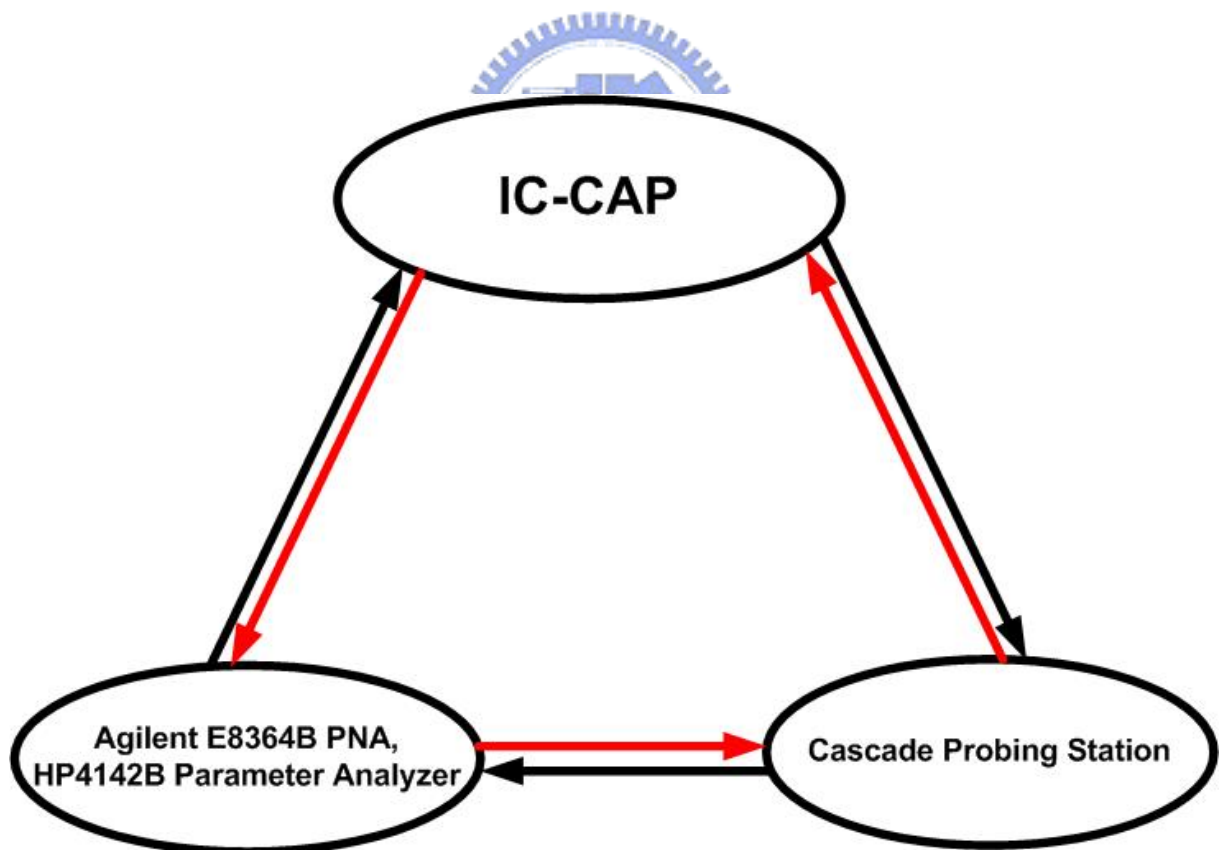


Figure 3.14 RF measurement equipment

### 3.2.3 Varying substrate resistivity

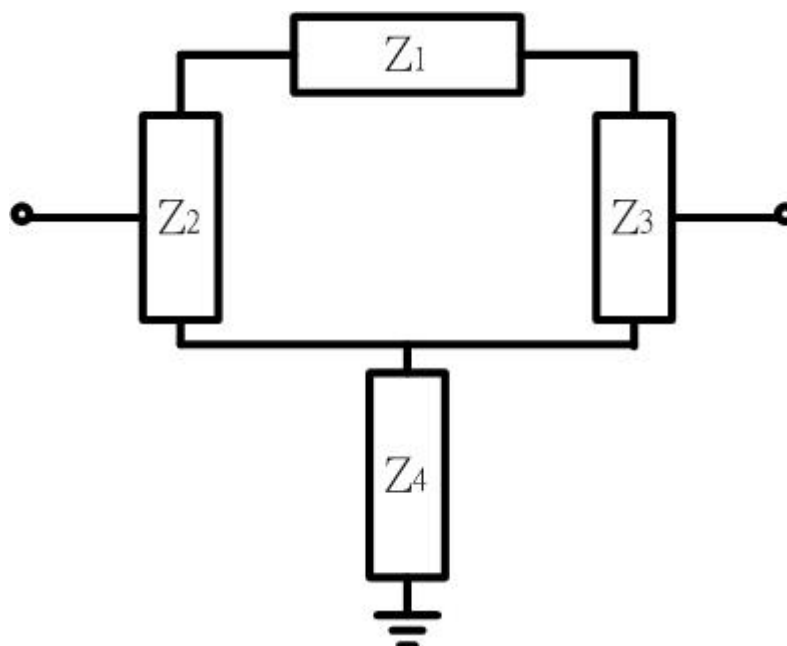
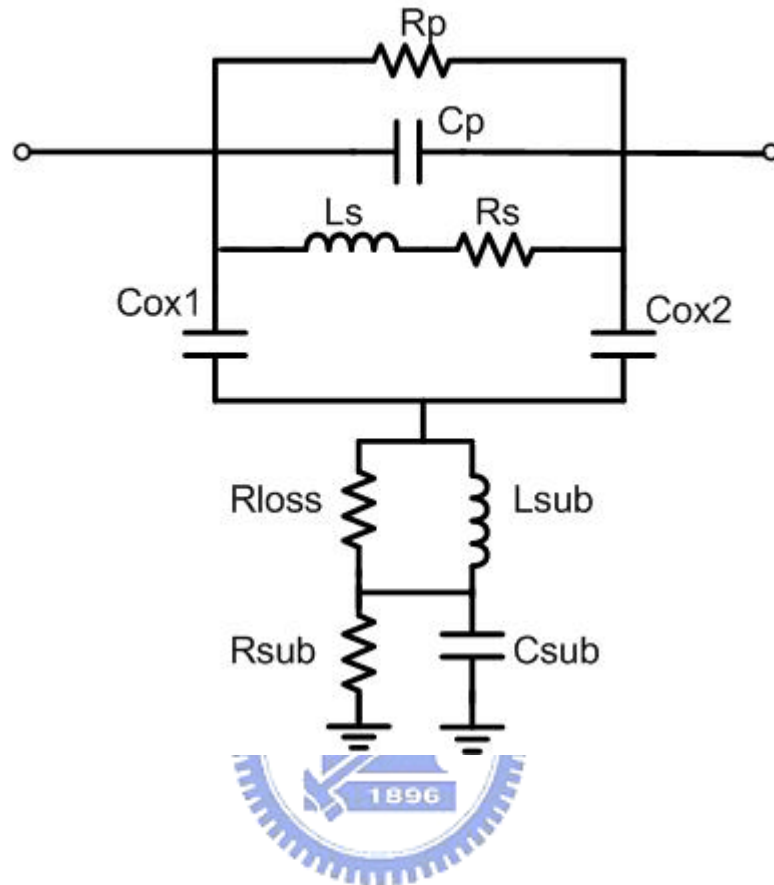
In varying substrate resistivity research, we use inductor devices, for example, single-end spiral inductors,  $N=2.5, 3.5, 4.5, 5.5$ . These were fabricated by 0.13 back end technology with eight layers of Cu and low k IMD ( $k=3.0$ ). The top metal is also  $3\mu\text{m}$  Cu used to implement the spiral coils of width fixed at  $15\mu\text{m}$  and inter-coil space at  $2\mu\text{m}$ . The inner radius is  $60\mu\text{m}$ . we will use above inductor devices to study varying substrate resistivity effect at  $Q$ ,  $f_{SR}$ , and  $f_{max}$  etc.... We major use simulation tools, for example, ADS Momentum. ADS Momentum simulation with extensive calibration is conducted to predict the broadband characteristics under varying substrate resistivity. We will discuss in the next section. Before discussing these section, we must built an equivalent circuit model to analysis above structures.



### 3. 3 T-model development and verification

After above section discussion and theory, a new T-model has been developed to accurately simulate the broadband characteristics of on-Si-chip spiral inductors, up to 20 GHz. The spiral coil and substrate RLC networks built in the model play a key role responsible for conductor loss and substrate loss in the wideband regime, which cannot math with the measured S-parameters,  $L(\omega)$ ,  $\text{Re}(\omega)$  and  $Q(\omega)$  proves the proposed T-model. In the next sections, we major analysis T-model structure.

### 3.3.1 Equivalent circuit analysis



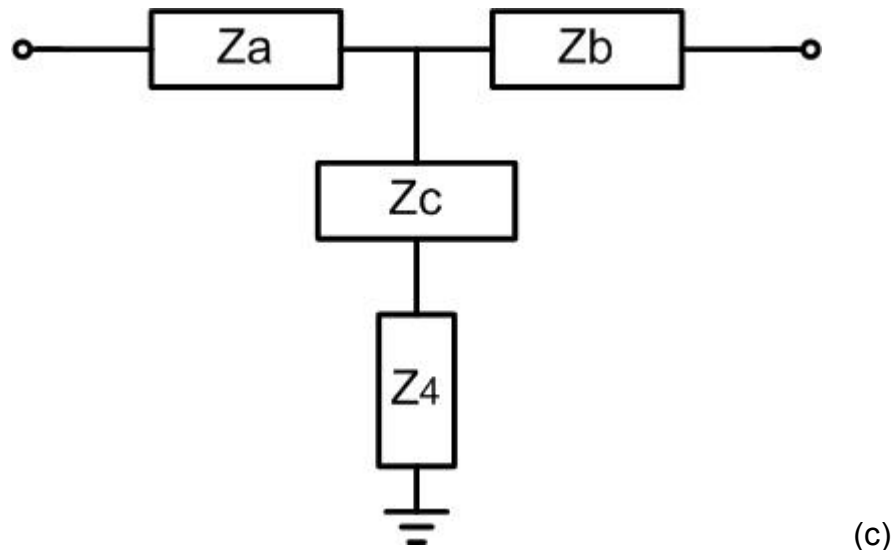


Figure 3.15 T-model for on-chip spiral inductors. (a) Equivalent circuit schematics. (b) Intermediate stage of schematic block diagrams for circuit analysis. (c) Final stage of schematic block diagrams for circuit analysis

In figure 3.15(a), it illustrates the circuit schematics of the proposed T-model for on-chip inductors in which two RLC networks of four physical elements for each part are linked through  $C_{ox}$  to account for the coupling between the spiral inductors and lossy substrate underneath. The physical property is defined for each element in the equivalent circuit.  $R_s$  and  $L_s$  represent the spiral metal coil's series resistance and inductance respectively.  $R_p$  is a new parameter created in T-model to account for spiral coil's conductor loss originated from lossy substrate return path.  $C_p$  indicates the inter-coil and under-pass capacitance and  $C_{ox}$  accounts for the spiral coil to substrate coupling capacitance.  $R_{sub}$  and  $C_{sub}$  represent the lossy substrate resistance and capacitance.  $L_{sub}$  and  $R_{loss}$  are two more new elements created in T-model to describe the eddy current induced substrate loss.  $L_{sub}$  accounts for the reactive power loss crossing the substrate and  $R_{loss}$  responsible for the resistive loss or joule heat dissipation. Figure 3.15(b) indicates the schematic block diagrams derived by circuit analysis theory to extract the physical circuit elements as proposed.  $Z_1$  represents the



RLC network for spiral inductor and  $Z_4$  is another one represents lossy substrate.  $Z_2 = Z_3 = 1/(j\omega C_{ox})$  acts as the coupling path between  $Z_1$  and  $Z_4$ . The circuit scheme is further transformed to figure 3.15(c) to correlate with Y-parameters from 2-port measurement.

### 3.3.2 Model parameter extraction flow

In this section, we begin to analysis equivalent circuit and extraction flow. All the unknown R, L, C parameters are extracted from analytical equations derived from equivalent circuit analysis as shown in Figure 3.15. The analytical equations are composed of Z-and/or Y-parameters listed in the first block of extraction flow illustrated in figure 3.16, which can be easily transformed from the measured S-parameter after appropriate de-embedding. Under the condition that the number of unknown elements is larger than the number of equations (for most of complicated problems like this condition), the approximation valid under very low or very high frequency is generally made to remove some unknown elements and extract the remaining ones as the first step, and then to extract the others at the second step. Due to the necessary approximation, the extracted R,L,C parameters in the first run of flow (figure 3.16) are generally not the exactly correct solutions but just serve as the initial guess for further optimization through best fitting to the measured S-parameters,  $L(\omega)$ ,  $\text{Re}(Z_{in}(\omega))$ , and  $Q(\omega)$ .

As a result, all the physical elements composing the model can be extracted through the flow shown in figure 3.17. At the first step,  $R_s$  and  $L_s$  representing the physical inductor under very low frequency can be extracted. The ideal quality factor

free from conductor and substrate losses, denoted as  $Q_s$  is given by  $Q_s = \omega L_s / R_s$ .

After that,  $R_p$  and  $C_p$  can be extracted by close forms as a function of  $(R_s, L_s, Q_s)$  and

measured  $-Y_{21}(=1/Z_1)$ .  $C_p$  represents the inter-coil and underpass coupling

capacitance, which is one of major elements to determine the frequency response, particularly the correct self-resonance frequency ( $f_{SR}$ ) and the phase near resonance.

$R_p$  is a new element introduced in our research to model the spiral conductor loss and Q degradation before resonance ( $f < f_{SR}$ ). Eddy current in the coil metal arising from the

magnetic field generated through substrate return path under high frequency is

proposed as the origin responsible for the additional spiral conductor loss represented

by  $R_p$ .  $C_{ox}$  is one more major element besides  $C_p$  to determine self-resonance

frequency ( $f_{SR}$ ) and can be derived by the equation of Z-parameters shown in the flow

chart. Then,  $L_{sub}$  and  $R_{sub}$  can be extracted easily from  $Z_4$  under very low frequency

provided that  $R_{loss}$  and  $1/\omega C_{sub}$  are relatively high impedances compared to  $\omega L_{sub}$

and  $R_{sub}$  and can be approximated as an open path. To the end,  $C_{sub}$  and  $R_{loss}$  can

be extracted by the formulas shown in the last stage of flow chart based on all the

known parameters and measured  $Z_4$ .  $R_{sub}$  is generally used to account for substrate

resistance and the associated energy loss.  $L_{sub}$  is another new element introduced in

T-model to simulate the eddy current generated on the Si substrate, which is expected

in opposite direction against the current flow in the spiral coils according to the Lenz'

law. In figure 3.9, we describe characterization clearly.  $L_{sub}$  is required to accurately

model frequency response of  $L$  and  $\text{Re}(Z_{in})$  near resonance but its effect on peak Q is

negligible. On the other hand,  $R_{sub}$  has quite obvious effect on Q degradation over

wide band.  $L_{sub}$ ,  $R_{sub}$  and  $R_p$  are required simultaneously to describe the substrate

loss precisely in terms of  $L(\omega)$ ,  $\text{Re}(Z_{in}(\omega))$ ,  $Q(\omega)$  and phase angle at different

frequencies.  $C_{sub}$  has been generally used in conventional p-model and it is justified

as necessary for T-model to account for the degradation of  $f_{SR}$  and  $Q$ .  $R_{loss}$  is the last one in total 3 new elements ( $R_p$ ,  $L_{sub}$ , and  $R_{loss}$ ) introduced in T-model.  $R_{loss}$  plays its role apparent near or beyond resonance. Lack of  $R_{loss}$  will leave  $L_{sub}$  alone and lead to abnormal double hump in S-parameters,  $L(\omega)$ ,  $Re(Z_{in}(\omega))$  and  $Q(\omega)$  beyond resonance.

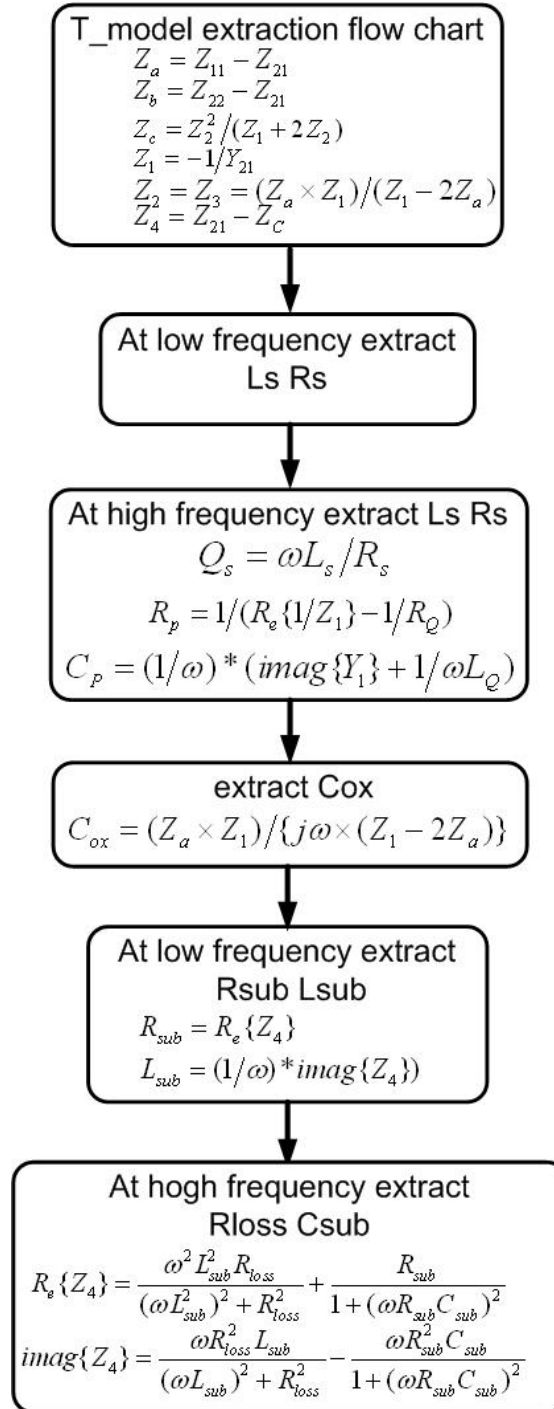


Figure 3.17 T-model parameter formulas and extraction flow chart.

### 3.3.3 Conductor loss and substrate loss effect

Regarding the conductor loss, that is the skin and current crowding effects, and substrate loss effect, which are considered playing an important role on  $Q$ , a frequency dependent  $R_s$  is generally proposed to fit the frequency response of  $Q$  over wide band. Through our research, the frequency dependent  $R_s$ , i.e.,  $R_s(\omega)$  formulated by the ideal model given by equation 3.9 is adopted and implemented to T-model in which  $R_p$  was removed to manifest  $R_s(\omega)$  effect alone. The simulated  $Q(\omega)$  shown in figure 3.18 reveals obvious deviation from measured one over frequencies beyond that of peak  $Q$  and suggests that  $R_s(\omega)$  alone cannot simulate the frequency response accurately even in narrow band around the peak  $Q$ .

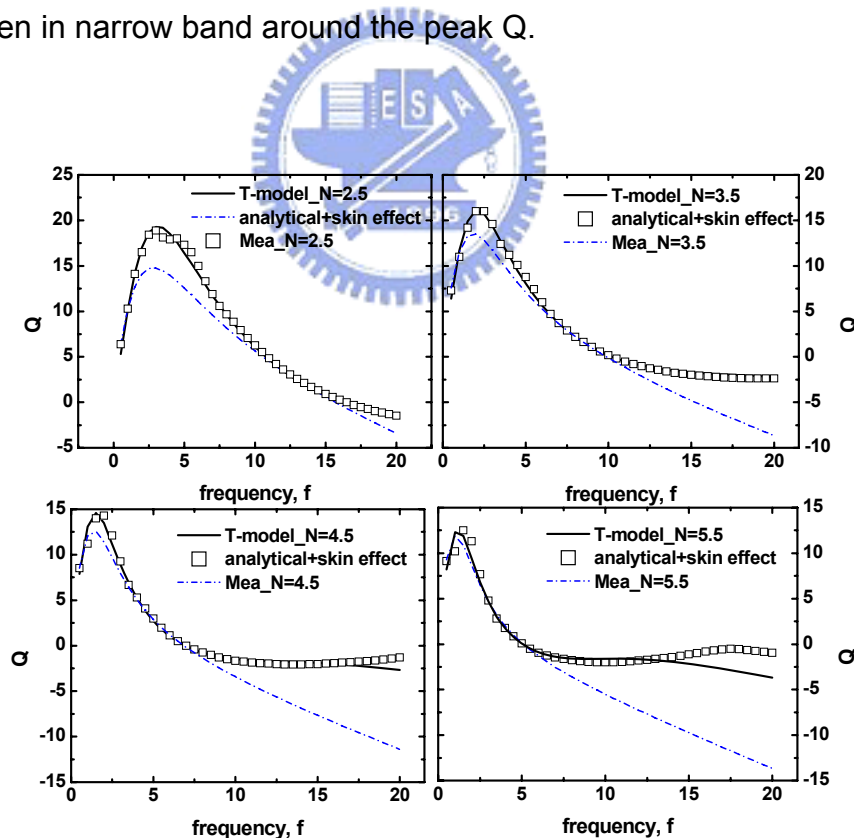


Figure 3.18  $Q(\omega)$  calculated by equivalent circuit removing  $R_p$  from original T-model and adding  $R_s(\omega)$  to simulate skin effect for spiral inductors with various coil numbers (a)  $N=2.5$  (b)  $N=3.5$  (c)  $N=4.5$  (d)  $N=5.5$

Besides, the frequency dependent elements are generally difficult to be implemented in time-domain simulators such as SPICE. To verify the origin responsible for the deviation,  $R_s(\omega)$  calculated by ideal model equation 3.9 is compared with the measured  $R_s = R_e(-1/Y_{21})$ . The result shown in figure 3.19 indicates that the ideal model can accurately fit  $R_s$  at very low frequencies ( $f < 2\text{GHz}$ ), but overestimates  $R_s$  at frequencies beyond 2GHz for all inductors of different coil numbers. The roll-off of  $R_s(\omega)$  revealed at higher frequency is proposed to stem from lateral substrate coupling effect. So it is to note that the dramatic increase of  $R_s(\omega)$  predicted by skin-effect model at higher frequency is actually an over-estimation compared to the measured one but cannot help to accurately reproduce Q degradation at frequencies near or beyond the peak Q. In T-model,  $R_p$  has been introduced as a new element to account for the spiral conductor loss and Q degradation over wide band. To justify the role played by  $R_p$ , simulation was done by removing  $R_p$  from the original T-model to verify the impact on  $L(\omega)$ ,  $\text{Re}(Z_{in}(\omega))$  and  $Q(\omega)$  as shown in figure 3.20, 3.21, 3.22 respectively. We see that  $R_p$  in this model has obvious on  $L(\omega)$  and  $\text{Re}(Z_{in}(\omega))$  at high frequency near resonance and significant impact on Q over wide band. The physical property and origin as defined previously for  $R_p$ , i.e., eddy current in the coil metal arising from the magnetic field generated through substrate return path is believed an appropriate mechanism to account for the broadband characteristics in terms of  $L(\omega)$ ,  $\text{Re}(Z_{in}(\omega))$  and  $Q(\omega)$  as demonstrated.

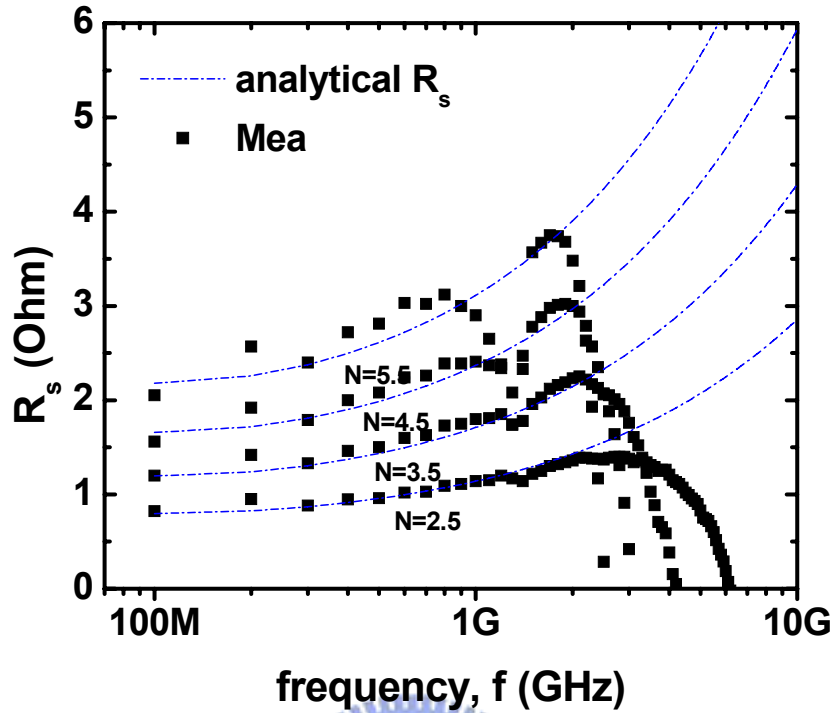


Figure 3.19 Frequency dependent  $R_s$  extracted from measurement through definition of  $R_s = R_e(-1/Y_{21})$  and the comparison with  $R_s(w)$  calculated by ideal model of equation 3.9 for spiral inductors with various coil numbers,  $N=2.5, 3.5, 4.5, 5.5$

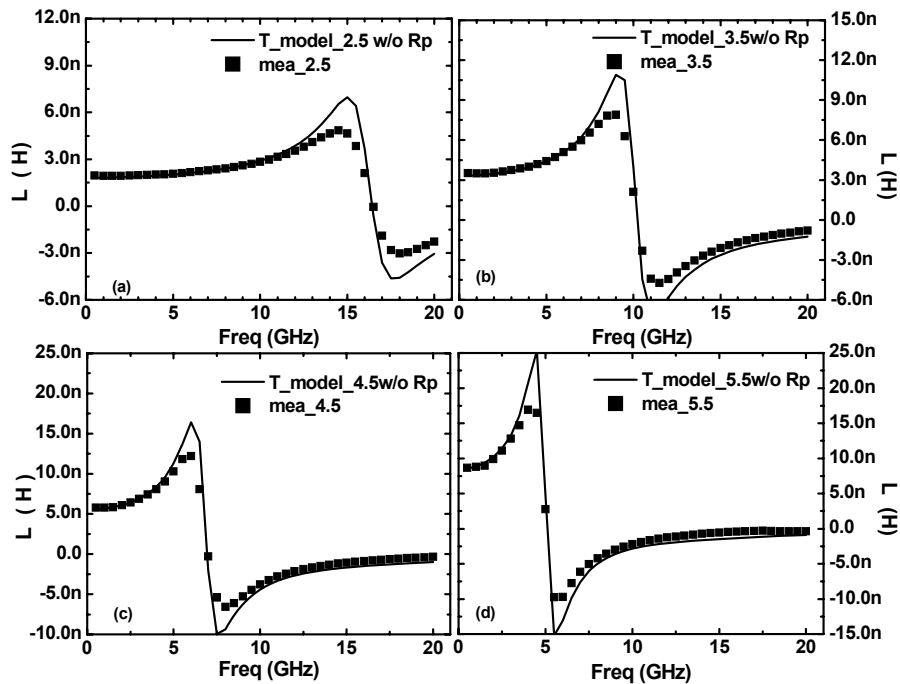


Figure 3.20  $L(\omega)$  calculated by equivalent circuit simulation with  $R_p$  removed from original T-model for spiral inductors with various coil numbers (a)  $N=2.5$  (b)  $N=3.5$  (c)  $N=4.5$  (d)  $N=5.5$

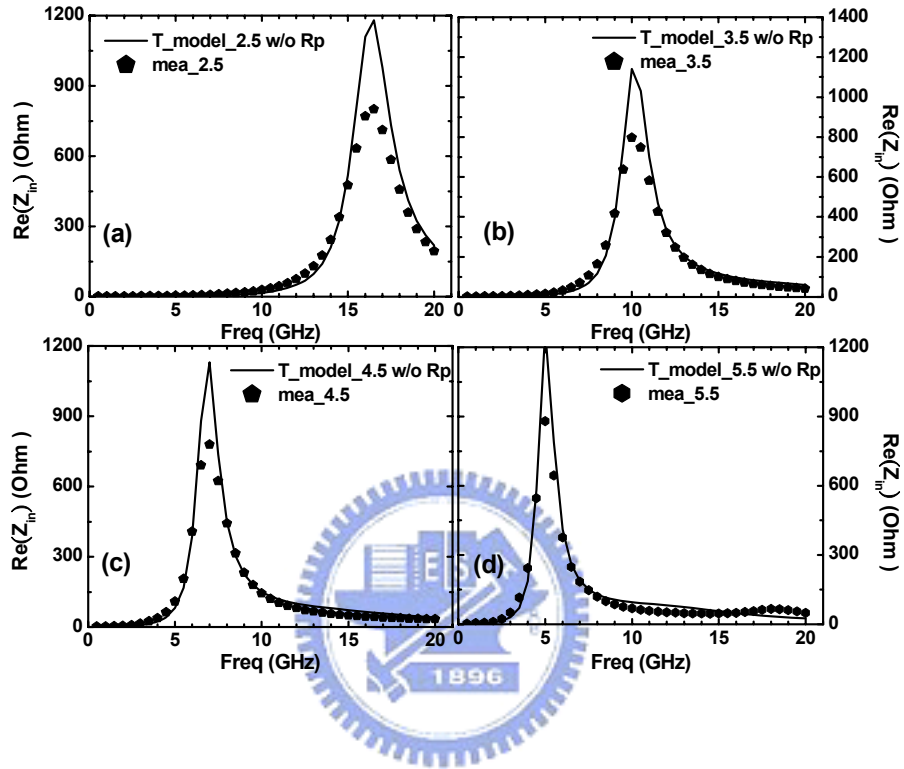


Figure 3.21  $\text{Re}(Z_{in}(\omega))$  calculated by equivalent circuit simulation with  $R_p$  removed from original T-model for spiral inductors with various coil numbers (a)  $N=2.5$  (b)  $N=3.5$  (c)  $N=4.5$  (d)  $N=5.5$

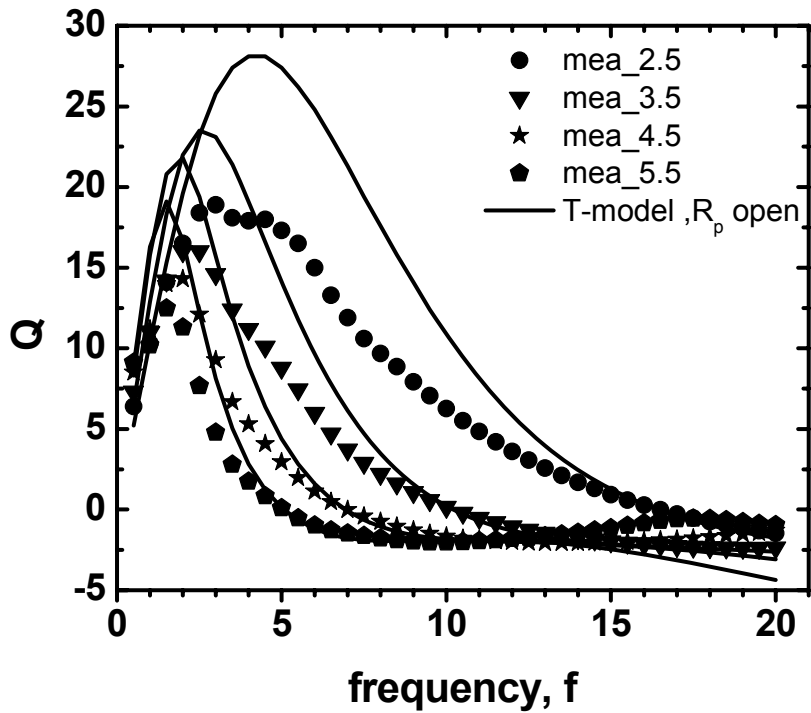
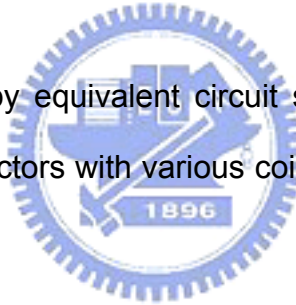


Figure 3.22  $Q(\omega)$  calculated by equivalent circuit simulation with  $R_p$  removed from original T-model for spiral inductors with various coil numbers (a)  $N=2.5$  (b)  $N=3.5$  (c)  $N=4.5$  (d)  $N=5.5$



### 3.3.4 Broadband accuracy

The proposed T-model has been extensively verified by comparison with measurement in terms of S-parameter ( $S_{11}$ ,  $S_{22}$ ),  $L(\omega)$ ,  $R_e(Z_{in}(\omega))$ , and  $Q(\omega)$  over broad bandwidth up to 20 GHz. The scalability is validated by various geometries with split of coil numbers,  $N=2.5$ , 3.5, 4.5, and 5.5, and width,  $W=3, 9, 15, 30\mu\text{m}$  for  $N=1.5$ . Broadband accuracy is justified by good match with measurement in terms of the mentioned key performance parameters. Figure 3.23 (a)-(d) and figure 3.24 (a)-(d) indicate the comparison for magnitude of  $S_{21}$  ( $\text{Mag}(S_{21})$ ) between the T-model and



measurement.

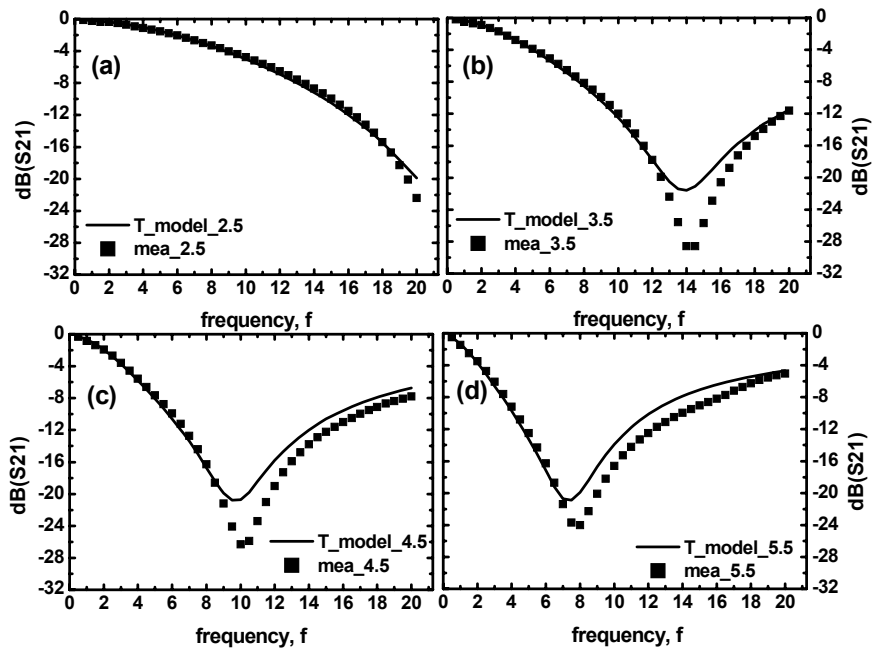


Figure 3.23 Comparison of  $S_{21}$  (magnitude) between T-model simulation and measurement for spiral inductors. Coil numbers (a)  $N=1.5$ , (b)  $N=2.5$ , (c)  $N=3.5$ , (d)  $N=4.5$

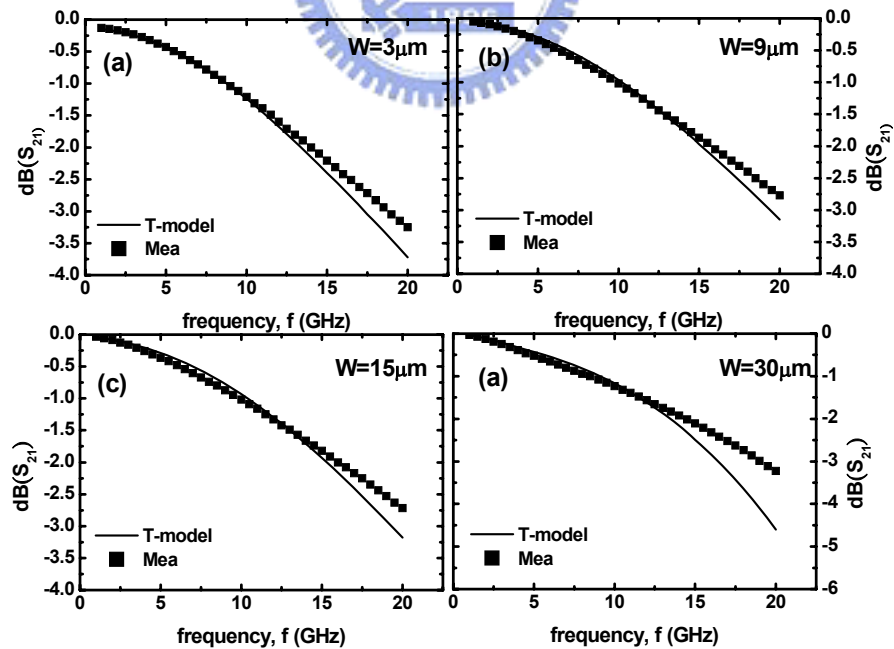


Figure 3.24 Comparison of  $S_{21}$  (magnitude) between T-model simulation and measurement for spiral inductors. Width for  $N=1.5$  (a)  $W=3\mu\text{m}$ , (b)  $W=9\mu\text{m}$ , (c)

W=15 $\mu$ m, (d) W=30 $\mu$ m

Excellent match is achieved for all coil numbers before resonance and agreement of curvature in maintained beyond resonance, which happened at  $f_{SR} \ll 20$ GHz for larger coil numbers (N=4.5 and 5.5). We will explain above condition in the next section. Figure 3.25 (a)-(d) and figure 3.26(a)-(d) show the good agreement in terms of phase ( $S_{21}$ ) in which precise match of resonance frequency ( $f_{SR}$ ) is demonstrated for all coil numbers and width for N=1.5.

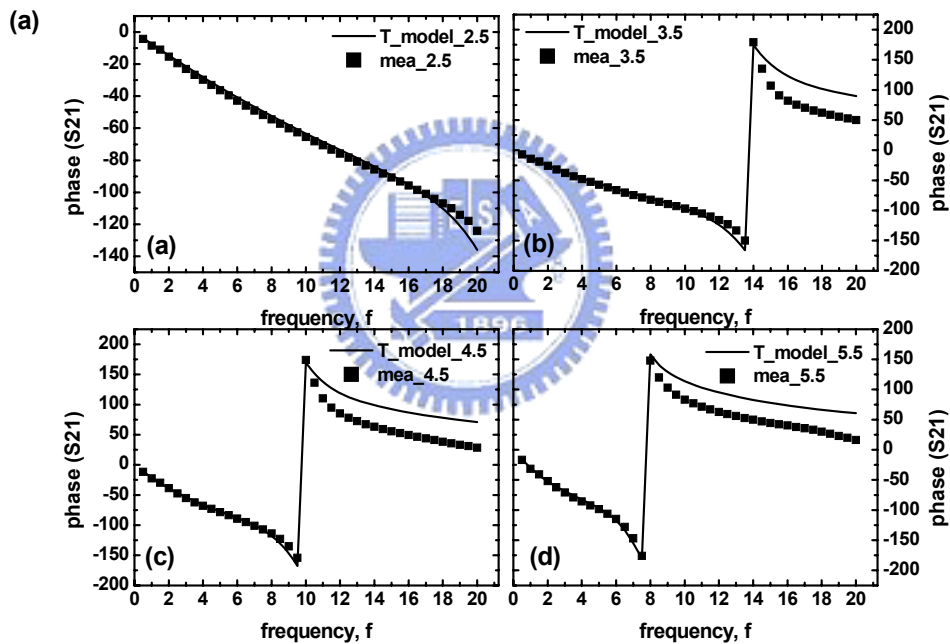


Figure 3.25 Comparison of  $S_{21}$  (phase) between T-model simulation and measurement for spiral inductors. Coil numbers (a) N=1.5, (b) N=2.5, (c) N=3.5, (d) N=4.5

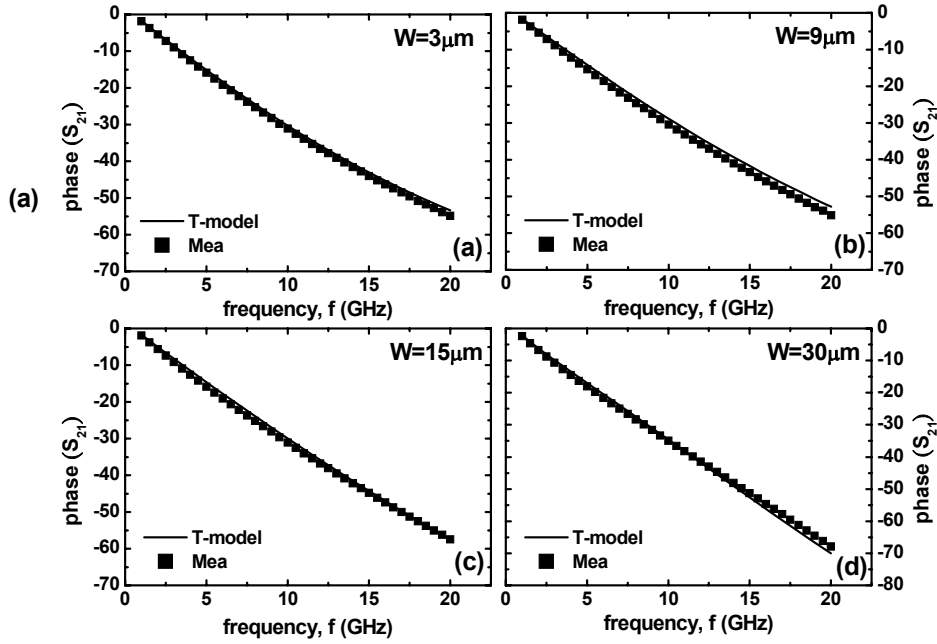


Figure 3.26 Comparison of  $S_{21}$  (phase) between T-model simulation and measurement for spiral inductors. Width for  $N=1.5$  (a)  $W=3\mu\text{m}$ , (b)  $W=9\mu\text{m}$ , (c)  $W=15\mu\text{m}$ , (d)  $W=30\mu\text{m}$



Figure 3.27 and 3.28 reveals the exact match of  $\text{Mag}(S_{11})$  for smaller coils ( $N=2.5, 3.5$ ) and various width for  $N=1.5$  over full frequency range up to 20GHz, which is well beyond resonance for larger coils ( $N=4.5, 5.5$ ) with  $f_{\text{SR}} = 6.9, 5.1$  GHz, i.e., far below 20GHz, it happened to be a common issue suffered by EM simulation. Fortunately, this deviation didn't make effect on the accuracy of  $L(\omega)$ ,  $\text{Re}(Z_{\text{in}}(\omega))$ , and  $Q(\omega)$  beyond resonance. Moreover, figure 3.29 and 3.30 confirms the model accuracy in terms of phase ( $S_{11}$ ) over broadband beyond resonance for each coil number and width for  $N=1.5$

More extensive verification has been done by comparison of four key performance parameters for spiral inductors, i.e.,  $L(\omega)$ ,  $\text{Re}(Z_{\text{in}}(\omega))$ ,  $Q(\omega)$ , and  $f_{\text{SR}}$ .  $L(\omega)$  is the imaginary part of input impedance  $Z_{\text{in}}(\omega)$ , i.e.,  $\omega L(\omega) = \text{Im}(Z_{\text{in}}(\omega))$  while  $\text{Re}(Z_{\text{in}}(\omega))$

represents the real part of  $Z_{in}(\omega)$ .

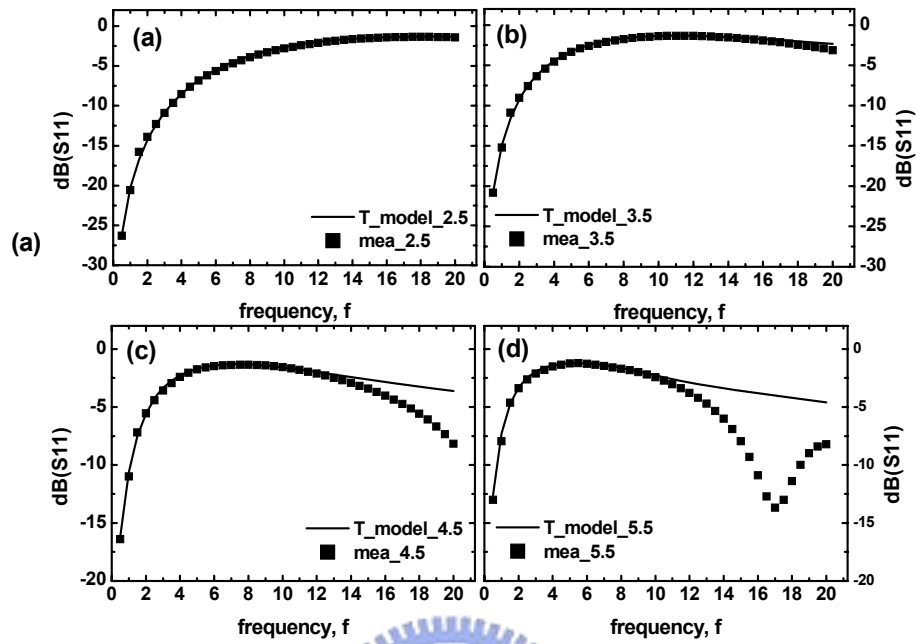


Figure 3.27 Comparison of  $S_{11}$  (magnitude) between T-model simulation and measurement for spiral inductors. Coil numbers (a)  $N=1.5$ , (b)  $N=2.5$ , (c)  $N=3.5$ , (d)  $N=4.5$

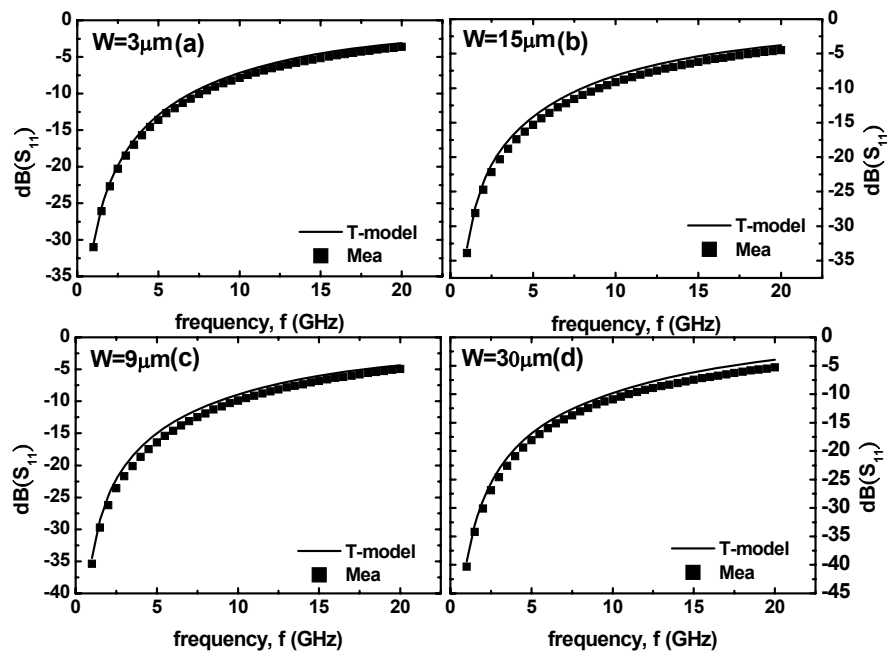


Figure 3.28 Comparison of  $S_{11}$  (magnitude) between T-model simulation and measurement for spiral inductors. Width for  $N=1.5$  (a)  $W=3\mu\text{m}$ , (b)  $W=9\mu\text{m}$ , (c)  $W=15\mu\text{m}$ , (d)  $W=30\mu\text{m}$

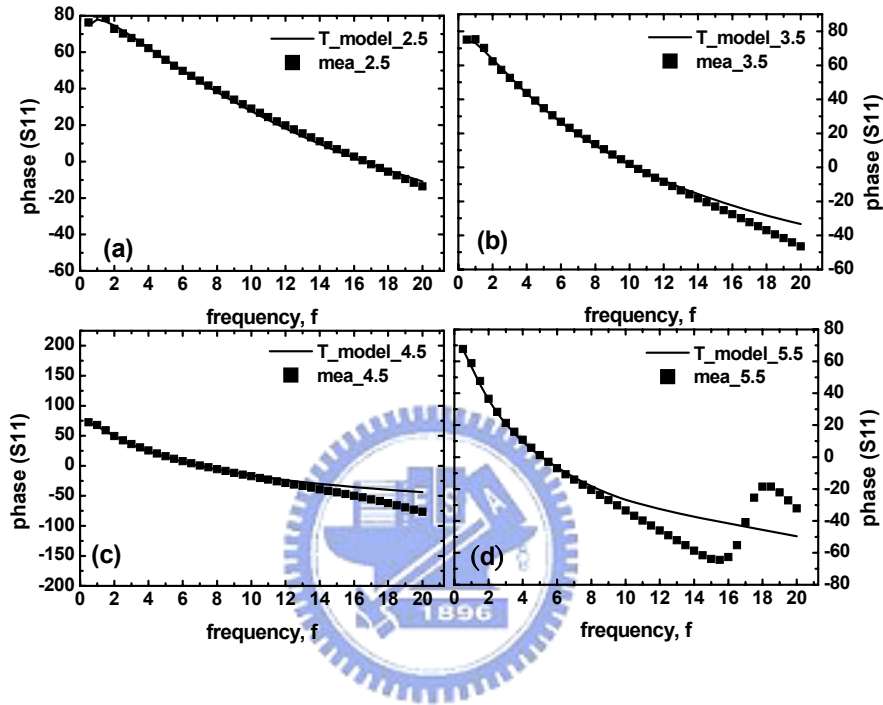


Figure 3.29 Comparison of  $S_{11}$  (phase) between T-model simulation and measurement for spiral inductors. Coil numbers (a)  $N=1.5$ , (b)  $N=2.5$ , (c)  $N=3.5$ , (d)  $N=4.5$

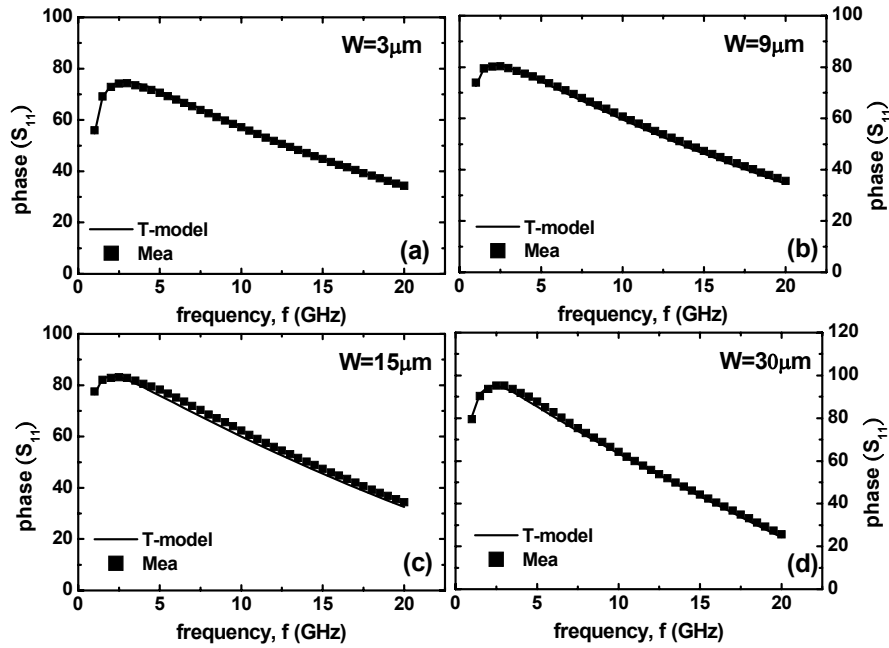


Figure 3.30 Comparison of  $S_{11}$  (phase) between T-model simulation and measurement for spiral inductors. Width for  $N=1.5$  (a)  $W=3\mu\text{m}$ , (b)  $W=9\mu\text{m}$ , (c)  $W=15\mu\text{m}$ , (d)  $W=30\mu\text{m}$

In this chapter,  $Q(\omega)$  is the quality factor defined by  $I_m(Z_{in}(\omega)) / R_e(Z_{in}(\omega))$ . All three parameters are frequency dependent that is critically related to the spiral conductor loss and Si substrate loss. In fact, accurate simulation to predict  $L(\omega)$ ,  $\text{Re}(Z_{in}(\omega))$  and  $Q(\omega)$  is the major goal of inductor models for physical element design. In our research, the proposed T-model can provide very good match with the measurement for the three parameters. Figure 3.31 and 3.32 illustrates the excellent fit to the measured  $L(\omega)$  by T-model for all spiral inductors operating up 20GHz. The transition from inductive to capacitive model evoked by increasing frequency beyond  $f_{SR}$  is accurately reproduced by the model. Regarding  $R_e(Z_{in}(\omega))$ , good match between the T-model and measurement are shown in figure 3.33 and 3.34. The T-model can exactly capture the full band behavior of  $R_e(Z_{in}(\omega))$  even beyond resonance such as

the dramatic increase prior to resonance, peak at resonance, and then sharp drop after the peak. Moreover,  $Q(\omega)$  is also good match.  $Q(\omega)$  is for the primary concern for inductor design and the first key parameter governing RFIC performance such as power, gain, and noise figure, etc. Figure 3.35 and 3.36 reveals the excellent match with the measured  $Q(\omega)$  over the broad bandwidth of 20GHz. Self-resonance frequency  $f_{SR}$  is a key parameter accompanying with  $Q(\omega)$  to quantify the useful bandwidth. In T-model,  $f_{SR}$  can be accurately predicted by both full equivalent circuit simulation and analytical model of closed form given by equation 3.10

$$f_{SR} = \frac{1}{2\pi} \sqrt{\frac{1}{L_s} \times \left( \frac{C_{ox1} + C_{ox2} + C_{sub}}{C_s(C_{ox1} + C_{ox2} + C_{sub}) + C_{ox1}(C_{sub} + C_{ox2})} \right)} \quad (3.10)$$

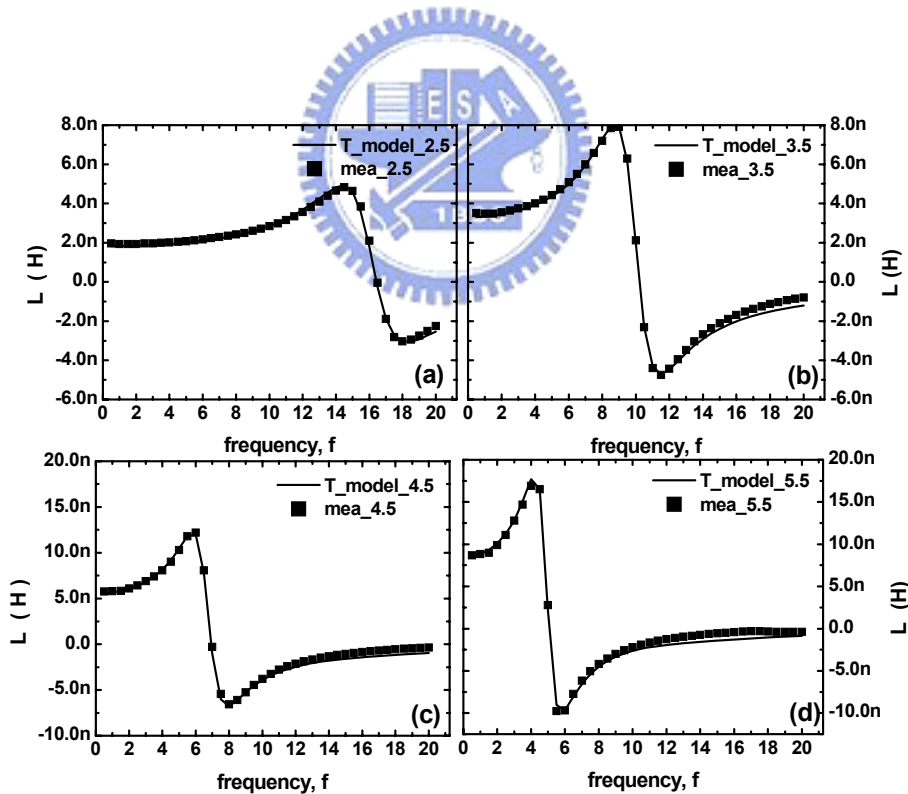


Figure 3.31 Comparison of  $L(\omega)$  between T-model simulation and measurement for spiral inductors. Coil numbers (a)  $N=1.5$ , (b)  $N=2.5$ , (c)  $N=3.5$ , (d)  $N=4.5$

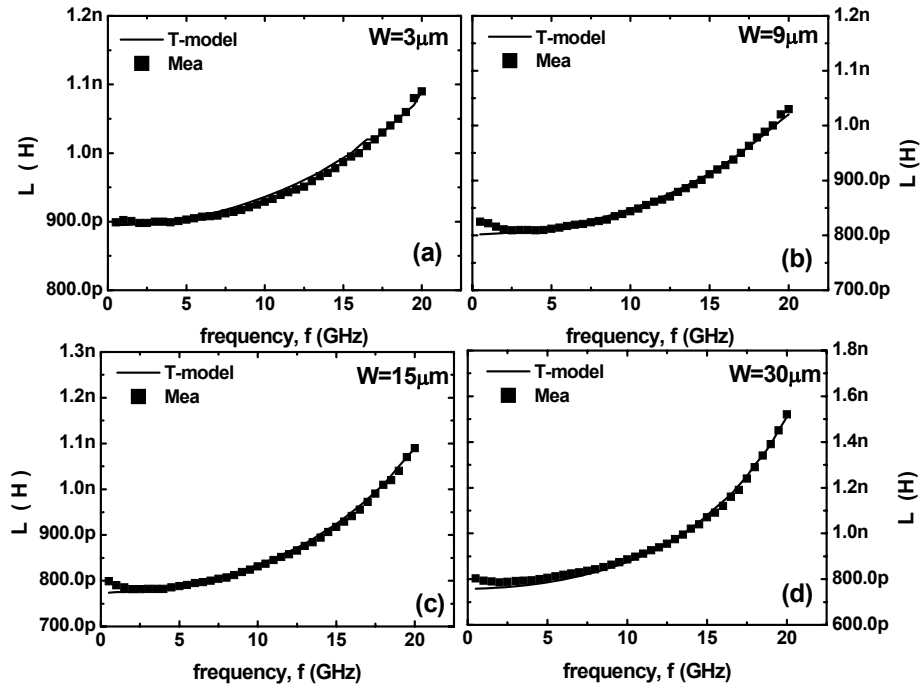


Figure 3.32 Comparison of  $L(\omega)$  between T-model simulation and measurement for spiral inductors. Width for  $N=1.5$  (a)  $W=3\mu\text{m}$ , (b)  $W=9\mu\text{m}$ , (c)  $W=15\mu\text{m}$ , (d)  $W=30\mu\text{m}$

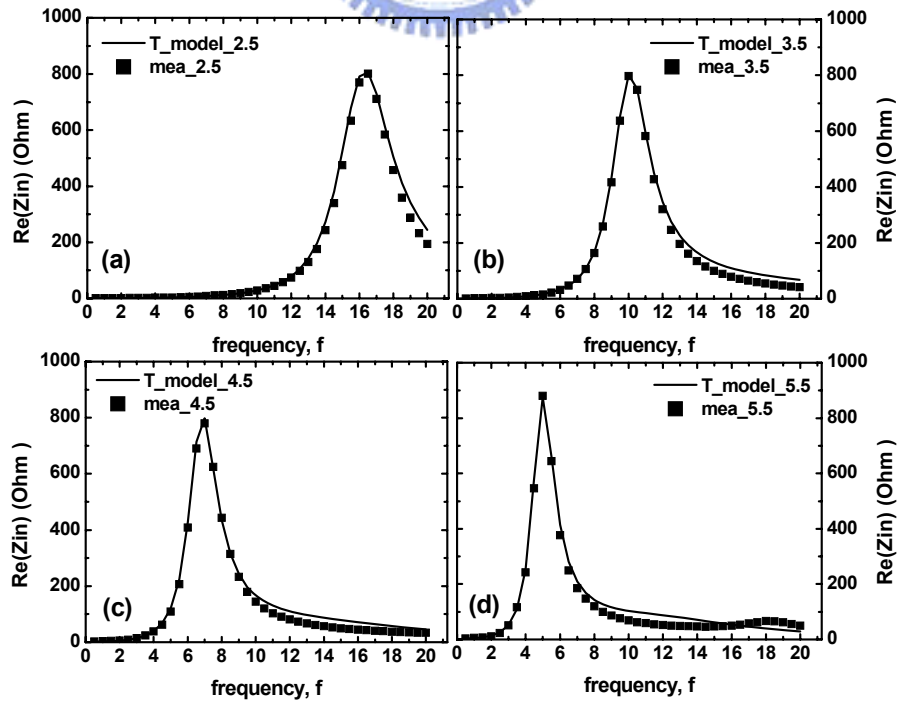




Figure 3.33 Comparison of  $\text{Re}(Z_{in}(\omega))$  between T-model simulation and measurement for spiral inductors. Coil numbers (a)  $N=1.5$ , (b)  $N=2.5$ , (c)  $N=3.5$ , (d)  $N=4.5$

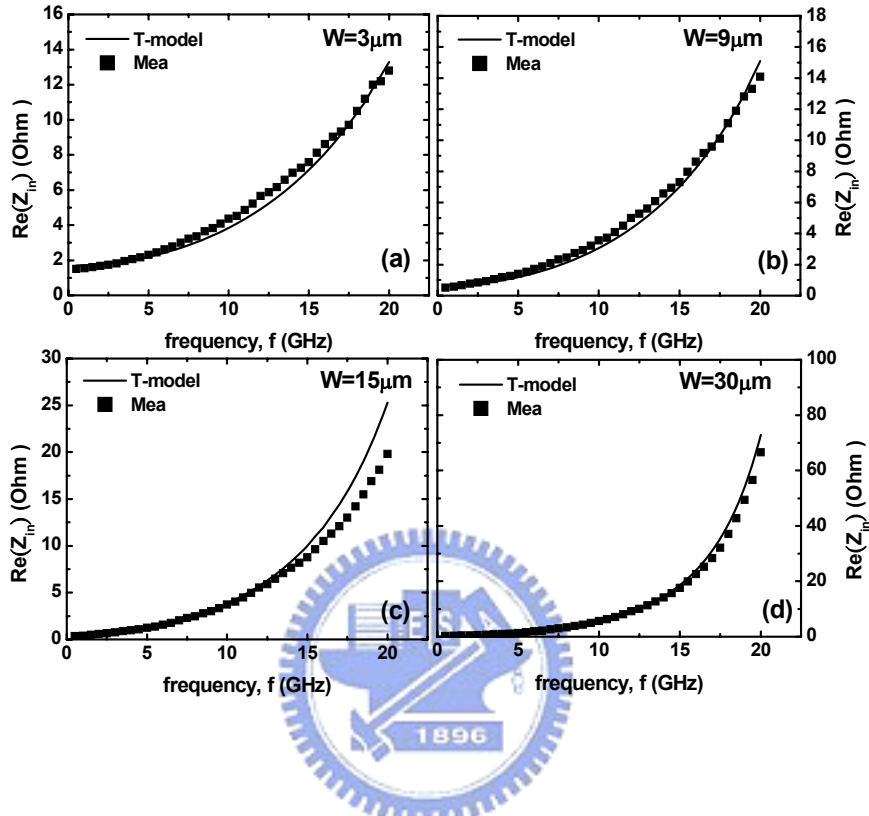


Figure 3.34 Comparison of  $\text{Re}(Z_{in}(\omega))$  between T-model simulation and measurement for spiral inductors. Width for  $N=1.5$  (a)  $W=3\mu\text{m}$ , (b)  $W=9\mu\text{m}$ , (c)  $W=15\mu\text{m}$ , (d)  $W=30\mu\text{m}$

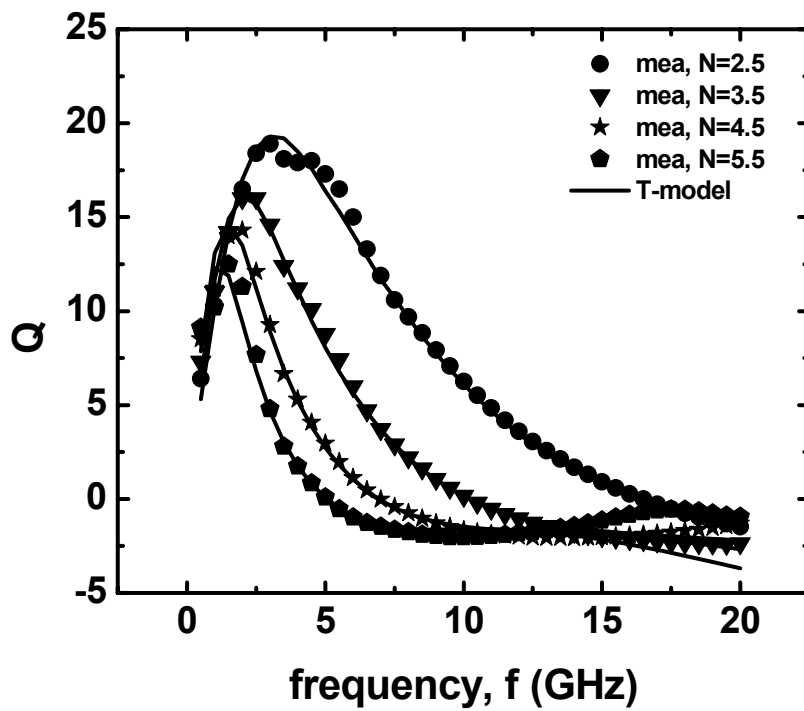


Figure 3.35 Comparison of  $Q(\omega)$  between T-model simulation and measurement for spiral inductors. Coil numbers:  $N=2.5, 3.5, 4.5, 5.5$

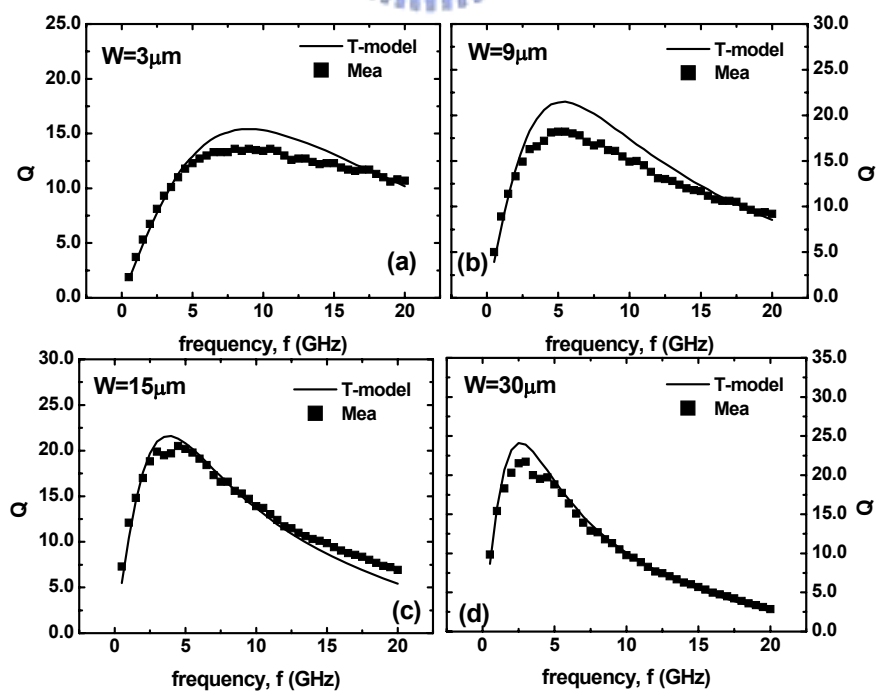


Figure 3.36 Comparison of  $Q(\omega)$  between T-model simulation and measurement for spiral inductors with different widths.

spiral inductors. Width for  $N=1.5$  (a)  $W=3\mu\text{m}$ , (b)  $W=9\mu\text{m}$ , (c)  $W=15\mu\text{m}$ , (d)  $W=30\mu\text{m}$

According to equation 3.10, the analytical model is readily derived under appropriate approximation. The details of model equation derivation can be referred to the Appendix. The major approximation made by removing  $L_{\text{sub}}$  and  $R_{\text{loss}}$  (i.e. neglect eddy current effect.) was justified by impedance analysis and equivalent circuit simulation. Figure 3.37 presents  $Q(\omega)$  calculated by reduced T-model without  $L_{\text{sub}}$  and  $R_{\text{loss}}$  and the comparison with original T-model with  $L_{\text{sub}}$  and  $R_{\text{loss}}$ .

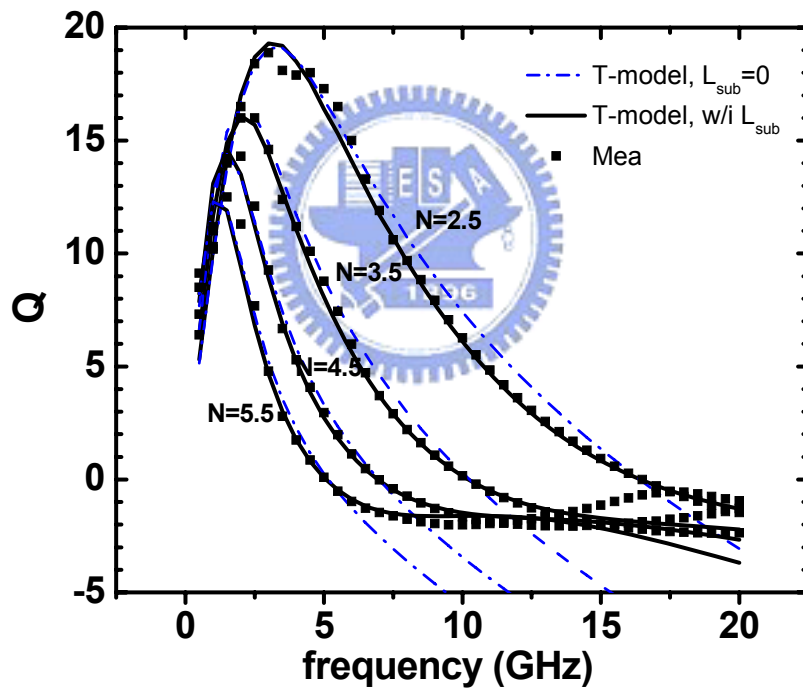


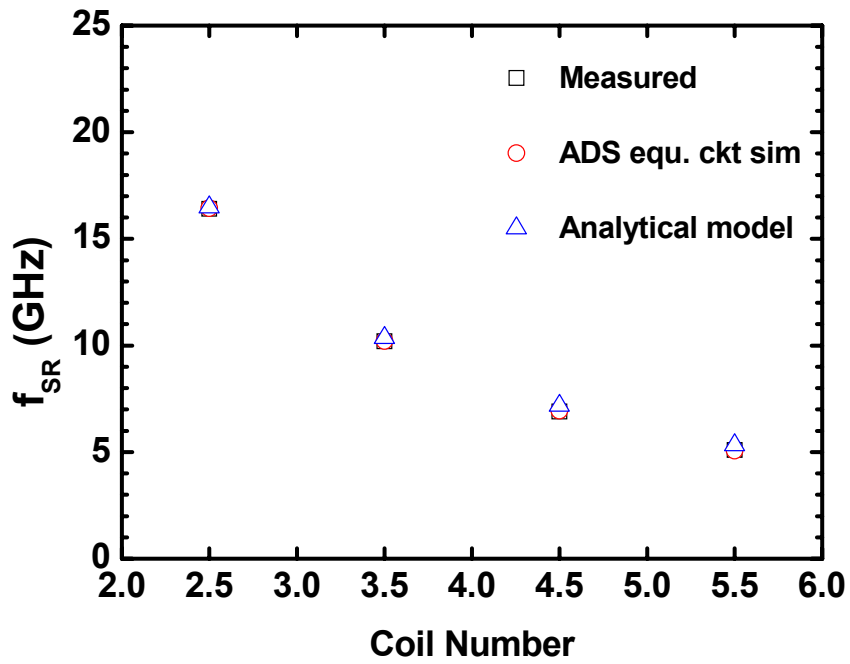
Figure 3.37 Comparison of  $Q(\omega)$  and self-resonance frequency  $f_{\text{SR}}$  corresponding to  $Q=0$  among T-model, reduced T-model ( $L_{\text{sub}} = R_{\text{loss}} = 0$ ) and measurement for spiral inductors with various coil numbers.

N	$f_{SR}$ , Measured	$f_{SR}$ ,ADS equ. ckt sim	$f_{SR}$ , Analytical model $L_{sub}=0$	$f_{SR}$ , T-model simulation $L_{sub}=0$
2.5	16.4	16.43	16.474	<b>17.15</b>
3.5	10.2	10.214	10.362	<b>10.92</b>
4.5	6.9	6.944	7.18	<b>7.64</b>
5.5	5.1	5.071	5.326	<b>5.73</b>

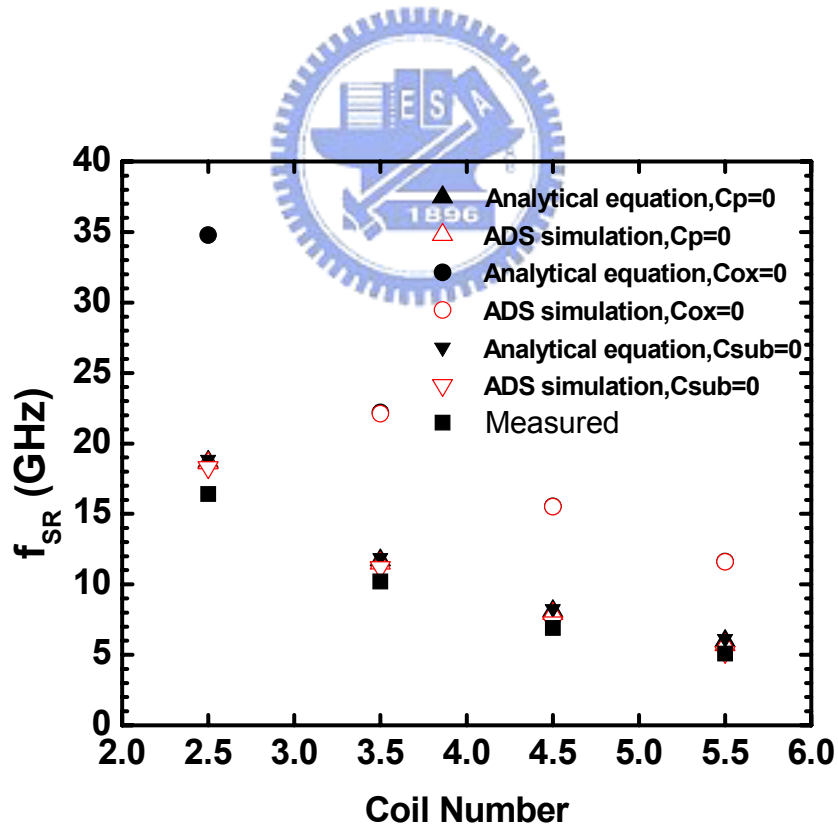
**Table**

Comparison of self-resonance ( $f_{SR}$ ) among measurement, simulation by original T-model and reduced T-model, and calculation by analytical model

The major difference is revealed in higher frequency region beyond the peak Q but the intercept point corresponding to  $Q=0$ . In next table, we will lists the exact values of  $f_{SR}$  for comparison among measurement, simulation by original T-model and reduced T-model, and calculation by analytical model of equation 3.10. According to above table, the good agreement to each other in terms of deviation below 0.2 GHz justifies the approximation for reduced T-model and derived analytical model for  $f_{SR}$ . The accuracy of  $f_{SR}$  calculated by the equivalent circuit simulation and analytical model is further validated by good match with the measured result shown in figure 3.38 (a)



(a)



(b)

Figure 3.38 (a) Self-resonance frequency  $f_{SR}$  of on-chip spiral inductors with various coil numbers,  $N=2.5, 3.5, 4.5, 5.5$  (a) comparison between measurement, ADS

simulation, and analytical model. (b)  $C_p$ ,  $C_{ox}$ , and  $C_{sub}$  effect on  $f_{SR}$  calculated by ADS simulation and analytical model. Comparison with measured  $f_{SR}$  to indicate the  $f_{SR}$  increase contributed by eliminating the parasitic capacitances,  $C_p$ ,  $C_{ox}$ , and  $C_{sub}$  respectively.

Regarding the parasitic capacitance effect on  $f_{SR}$  as mentioned previously, Figure 3.38 (b) indicates the  $C_p$ ,  $C_{ox}$ , and  $C_{sub}$  effect on  $f_{SR}$  predicted by ADS simulation using full equivalent circuit and analytical model given by equation 3.10. The results from ADS simulation and analytical model show very good consistency. We see that the elimination of  $C_p$  or  $C_{sub}$  can help to increase  $f_{SR}$  by around 15~20% corresponding to  $N = 2.5, 3.5, 4.5, 5.5$  while the elimination of  $C_{ox}$  can dramatically boost  $f_{SR}$  by more than 100%, i.e., more than double the existing performance for all coil numbers. The prediction from our T-model suggests that  $C_{ox}$  plays a dominant role in determining  $f_{SR}$  and spiral inductor on package is a potential solution to minimize  $C_{ox}$  and achieve maximum  $f_{SR}$ .

### 3.3.5 Scalability

Besides the broadband accuracy as presented, another important feature realized by this T-model is the good scalability w.r.t. geometry for all model parameters. Figure 3.39 reveals good match with a linear function of coil number for each model parameter in the spiral coil's RLC network, i.e.,  $R_s$ ,  $L_s$ ,  $R_p$ ,  $C_p$  and  $C_{ox}$ . All five elements present monotonically increasing function of coil number in which coefficient of first order derivative has been extracted for every parameter. In reality, the inductance  $L$  follows a curve more complicated than linear function. As shown in

figure 3.39 (a),  $L$  can be precisely fitted by a parabolic function of  $N$  (coil number). Figure 3.41 indicate the excellent fit by linear function for substrate RLC network involved model parameters,  $1/R_{\text{sub}}$ ,  $C_{\text{sub}}$ ,  $L_{\text{sub}}$  and  $R_{\text{loss}}$ . The decrease of  $R_{\text{sub}}$  or increase of  $1/R_{\text{sub}}$  corresponding to larger coil number accounts for the worse substrate loss caused by increasing spiral coil size. Regarding  $C_{\text{sub}}$ ,  $L_{\text{sub}}$ , and  $R_{\text{loss}}$ , all three terms follow linearly increasing function of  $N$ . The scaling behavior revealed by the four parameters is physically derivable and sufficiently accurate to calculate substrate loss effect on  $L(\omega)$ ,  $Q(\omega)$  and  $f_{\text{SR}}$ , ect. for inductor of various spiral coil sizes. Regarding interest in more extensive scope of layout geometries such as coil metal width or inner radius, a preliminary work has been done to validate the model over wide range of widths (3, 9, 15, and 30  $\mu\text{m}$ ). Good fit to all measured parameters as mentioned can be maintained and model scalability is presented as a parabolic function instead of a linear function. Please see figure 3.41 and 3.42 A minor modification to the original T-model by adding an inductor element ( $L_p$ ) in series with  $R_p$  to account for proximity effect can further improve the fitting accuracy. The promisingly good scalability proven for full set of model parameters as demonstrated suggests that this T-model is useful in pre-layout simulation and optimization for physical design. The nature of easy link with standard circuit simulator makes this T-model useful in circuit element tuning and optimization for RF circuit design.

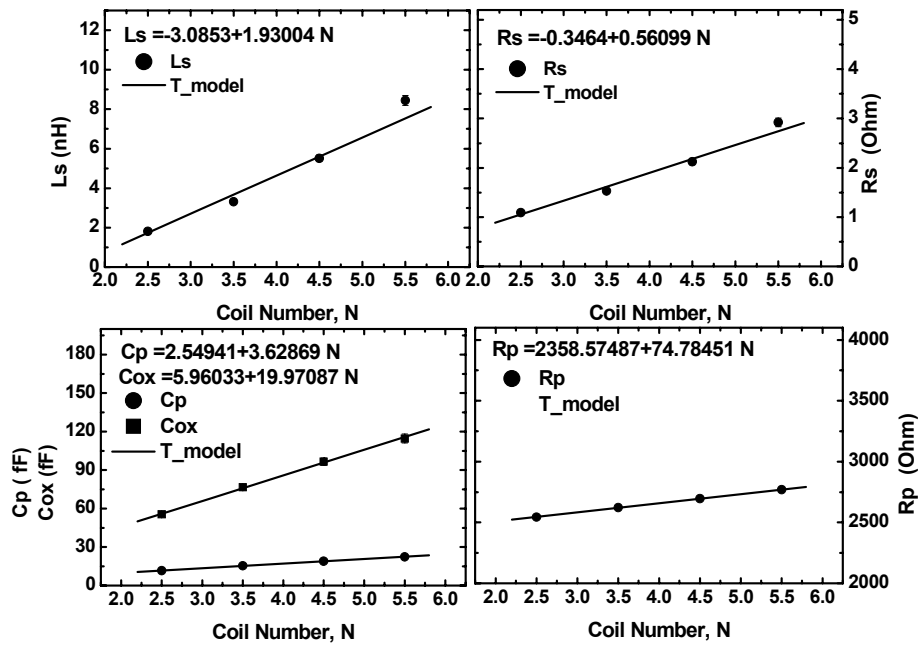


Figure 3.39 T-model RLC network parameters versus coil numbers, spiral coil's RLC network parameters (a)  $L_s$  (b)  $R_s$ , (c)  $C_p$  and  $C_{ox}$  and (d)  $R_p$

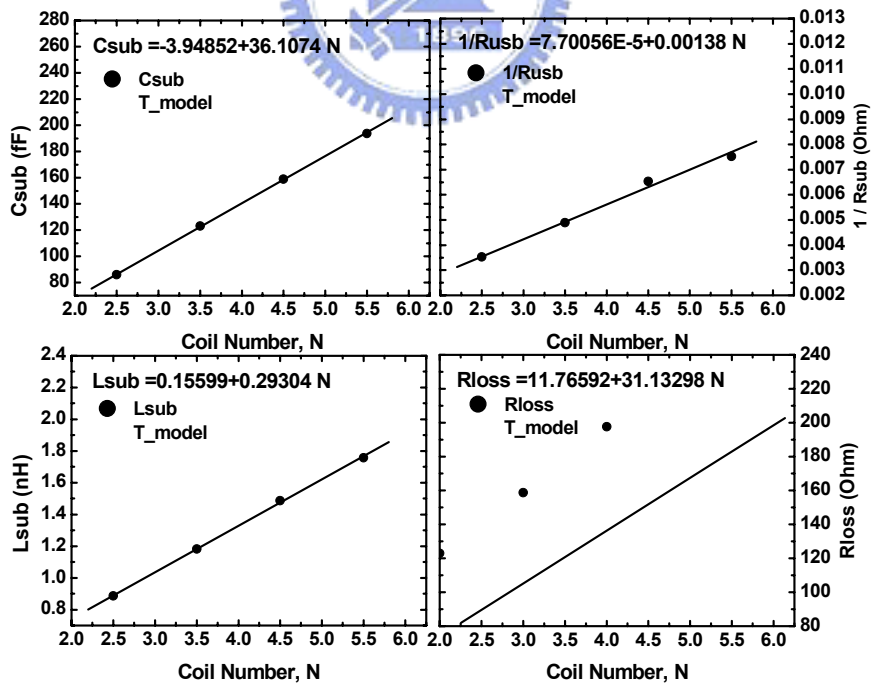


Figure 3.40 T-model RLC network parameters versus coil numbers, lossy substrate RLC network parameters (a)  $C_{sub}$  (b)  $1/R_{sub}$ , (c)  $L_{sub}$  and (d)  $R_{loss}$



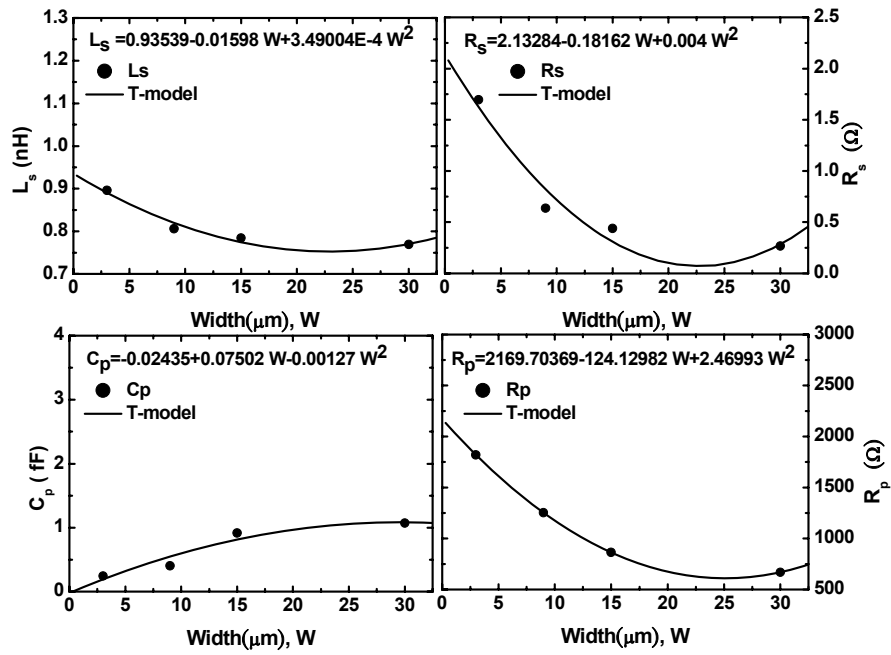


Figure 3.41 T-model RLC network parameters versus width, spiral coil's RLC network parameters (a)  $L_s$  (b)  $R_s$ , (c)  $C_p$  and (d)  $R_p$

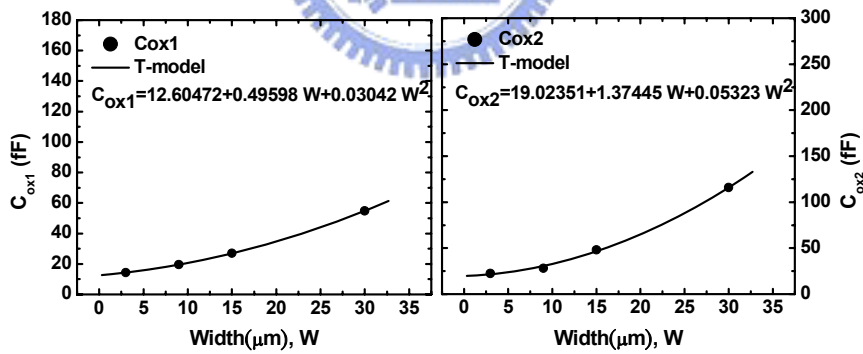


Figure 3.42 T-model RLC network parameters versus width, lo spiral coil's RLC network parameters (a)  $C_{ox1}$  (b)  $C_{ox2}$ , (c)  $L_p$

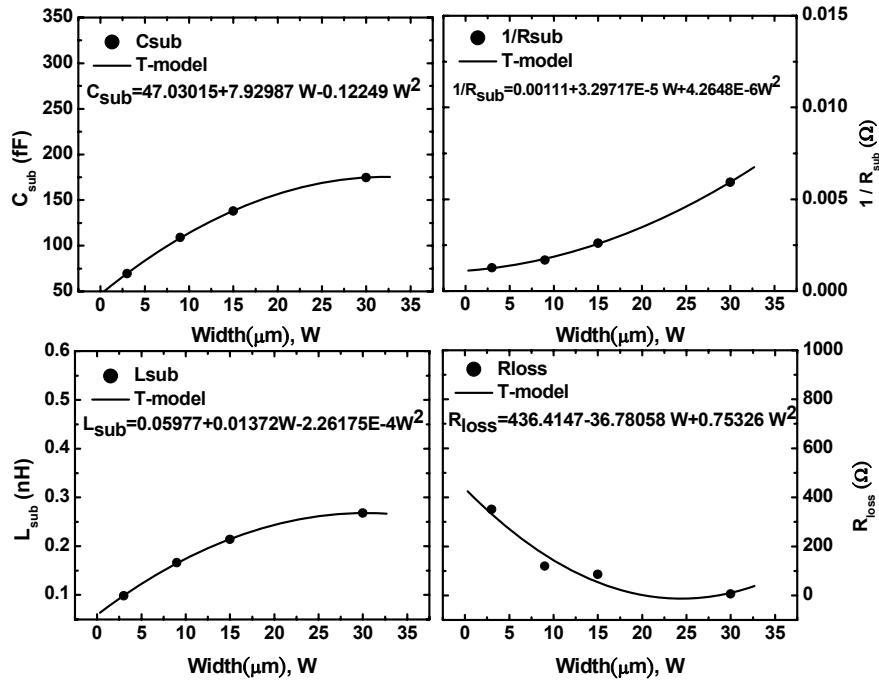
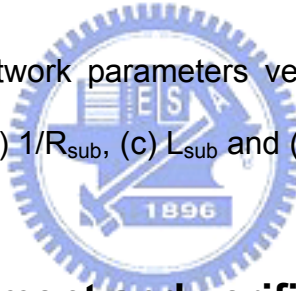


Figure 3.43 T-model RLC network parameters versus width, lossy substrate RLC network parameters (a)  $C_{sub}$  (b)  $1/R_{sub}$ , (c)  $L_{sub}$  and (d)  $R_{loss}$



### 3. 4 T-model enhancement and verification

In this section, we will consider  $\text{Mag}(S_{21})$ ,  $\text{phase}(S_{11})$ ,  $\text{Mag}(S_{11})$ , and  $\text{phase}(S_{11})$  for larger coil numbers ( $N=4.5, 5.5$ ) deviation beyond resonance with  $f_{SR} = 6.9, 5.1\text{GHz}$ . In this portion, we discuss in accordance with substrate loss, for example, eddy current effect. The 3D eddy current is identified as the key element essential to accurately simulate broadband characteristics for a large coil number ( $N=4.5, 5.5$ ). we will introduce our concept in this section.

### 3.4.1 Enhancement over the simple T-model

In the electromagnetic field, inductors allow the storage of magnetic energy. Figure 3.44 shows the electric and magnetic substrate loss of spiral inductors. The magnetic field extends around the windings and into the substrate. In figure 3.34, its direction is Z-axis. Faraday's Law states that this time-varying magnetic field will induce an electric field in the substrate.

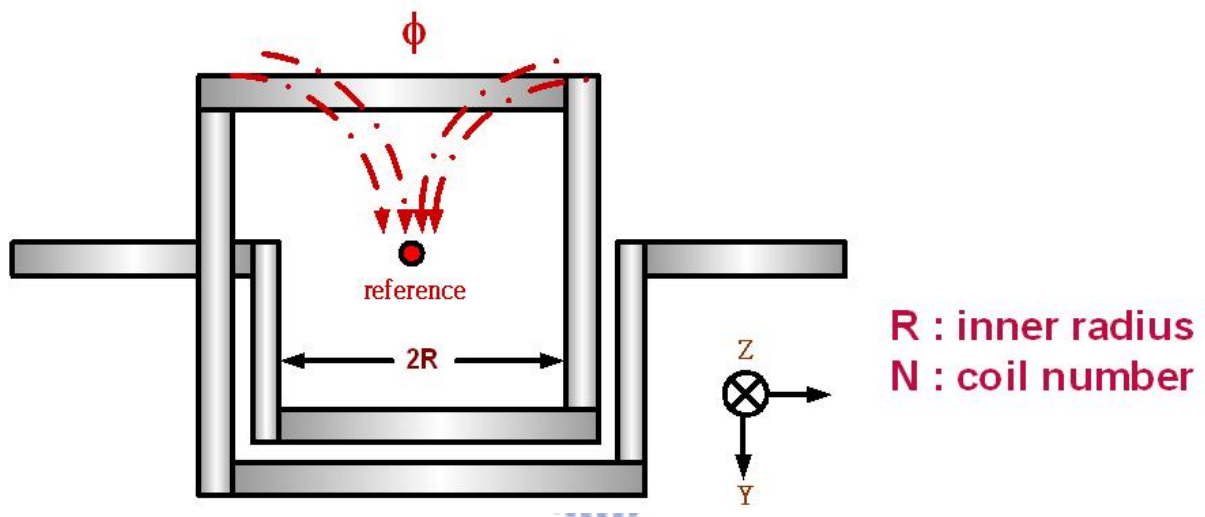


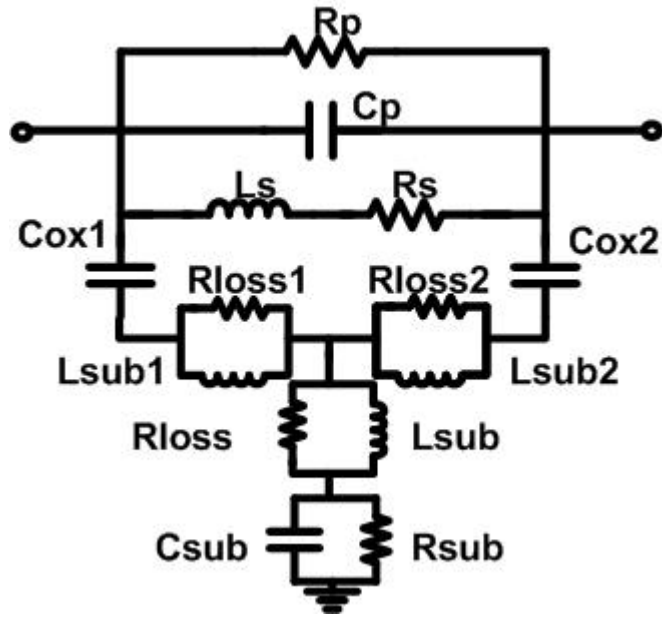
Figure 3.44 Magnetic field in the single-end spiral inductor

Because time-varying magnetic field induces an electric field in the substrate, the field will force an image current to flow in the substrate in opposite direction of the current in the winding directly. While a larger coil number generates time-varying magnetic field, eddy current effect is induced more serious. We begin to study above physical phenomenon. In this section, an improved T-model is devised to enhance the broadband accuracy beyond resonance. The early resonance suffered by larger spiral coils generally reveals lower  $f_{SR}$ , maybe far below 20GHz. So it brings a challenge to most of lump element models and even to EM simulators to achieve

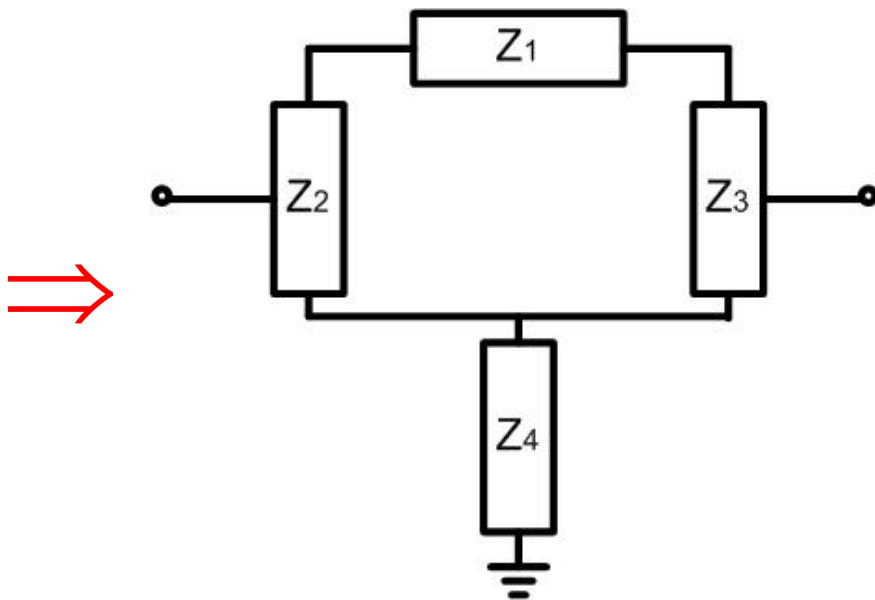
precise matching with measurement beyond resonance. Moreover, in above research through 3D EM simulation (Ansoft HFSS i.e. please see section 3.1.2) we identify that substrate eddy current effect is actually a 3D coupling behavior rather than a simplified planar feature. Figure 3.13 shows above mention. The 3D eddy current effect plays a major role in frequency response beyond resonance for the on-chip inductors.

### **3.4.2 Equivalent circuit analysis and Model parameter extraction flow**

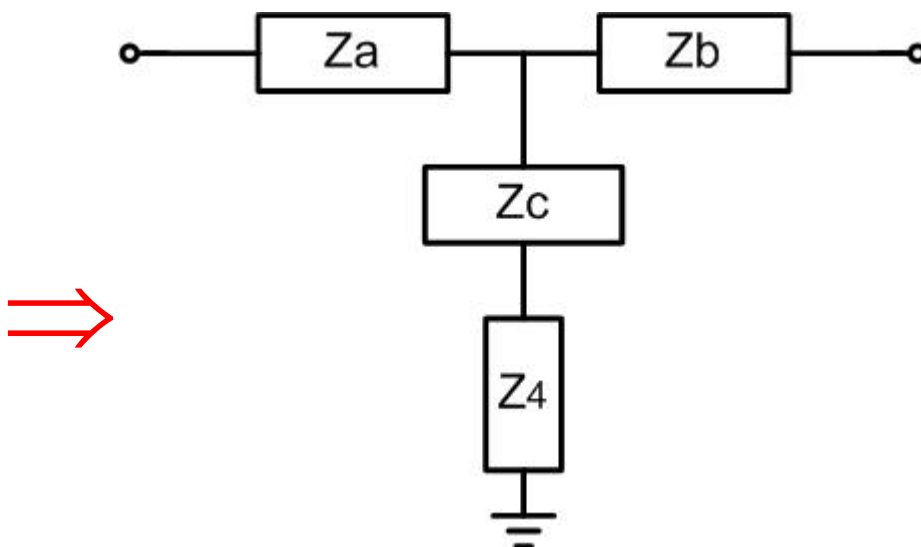
In improve T-model, major three branches of parallel RL elements are deployed to emulate the 3D eddy circuit effect. All the equivalent circuit elements are kept constants independent of frequencies and can be expressed by a closed form derived from circuit analysis. Figure 3.45 illustrates the circuit schematics of the improved T-model for on-chip inductors. The major enhancement over our research is the deployment of three branches of parallel RL elements using a T-shape configuration to simulate the 3D eddy current.



(a)



(b)



(c)

Figure 3.45 Improved T-model (a) equivalent circuit schematics, (b) and (c) schematic block diagram for circuit analysis

We design improved T-model idea that comes from 3D EM simulation by Ansoft HFSS. We identify that substrate eddy current effect is actually 3D coupling behavior rather than a simplified planar feature. From figure 3.45, two branches of parallel RL in series with  $C_{ox1}$  and  $C_{ox2}$  account for the eddy current component normal to the substrate plane and the other RL element in series with substrate RC network represents the eddy current in the plane. Two RLC networks of four physical elements for each are linked through  $C_{ox1}$  and  $C_{ox2}$  in series with parallel RL to account for the EM coupling between the single-end spiral inductors and lossy substrate underneath. Figure 3.45 (b) indicates the block diagrams derived by circuit analysis to extract the physical circuit elements.  $Z_1$  represents the RLC network for spiral inductor and  $Z_4$  represents the lossy substrate.  $Z_2$  and  $Z_3$  consisting of  $C_{ox1}$ ,  $C_{ox2}$  and parallel RL network for normal component of eddy current effect as the coupling path between  $Z_1$  and  $Z_4$ . We use circuit analysis theory Y-parameter transformed to Z-parameter from 2-port measurement. Figure 3.46 indicates all the physical elements composing the model extracted.

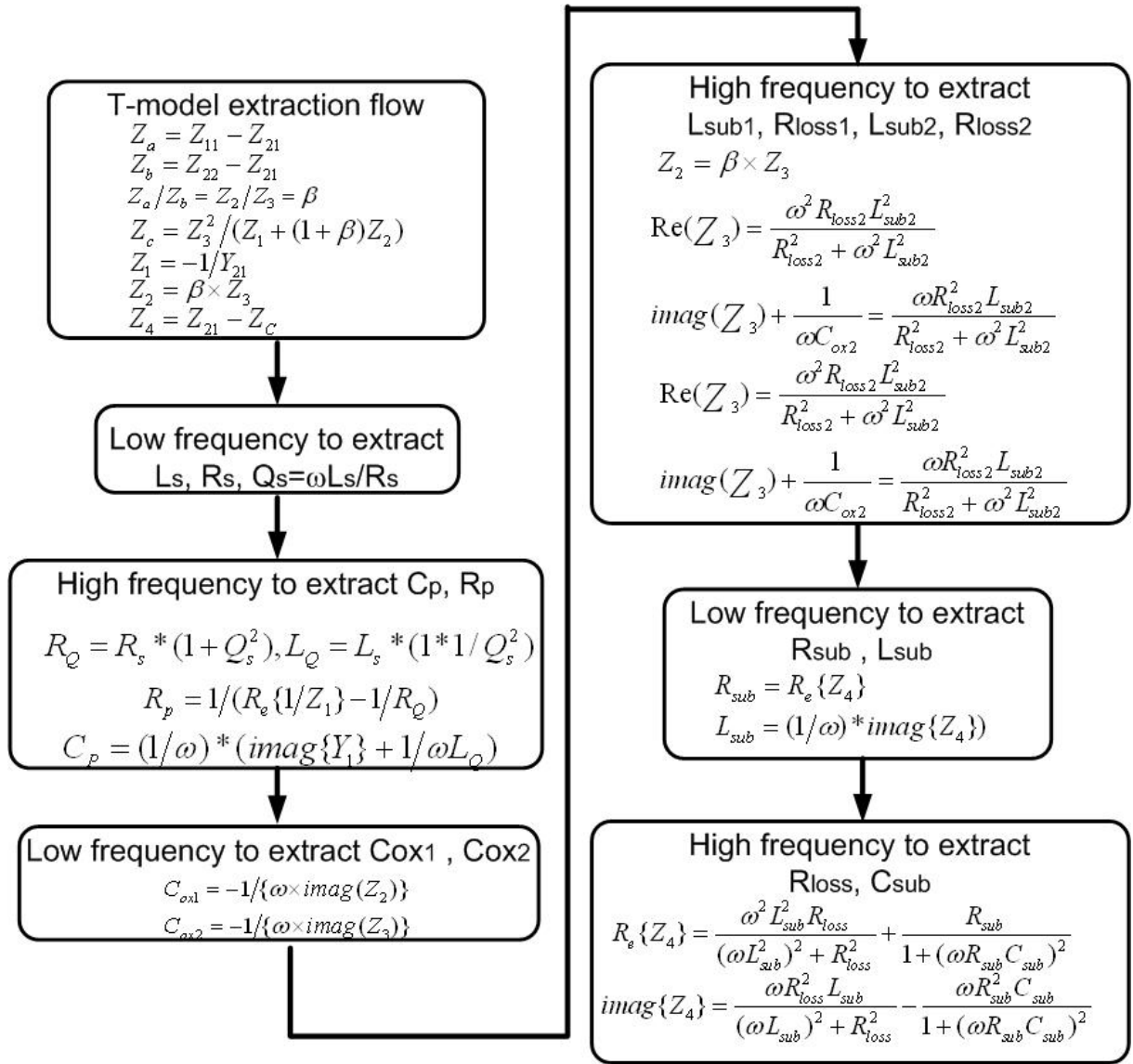


Figure 3.46 Improved T-model parameter formulas and extraction flow chart

The details of extraction for the lump circuit elements in two primary RLC networks. Regarding the extraction of new elements added in this improved T-model. We extract  $C_{ox1}$  and  $C_{ox2}$  from  $Z_2$  and  $Z_3$  under very low frequency provided that  $\omega L_{sub1} // R_{loss1}$  and  $\omega L_{sub2} // R_{loss2}$  are negligibly small impedances compared to  $1/\omega C_{ox1}$  and  $1/\omega C_{ox2}$ , respectively. After extracting  $C_{ox1}$  and  $C_{ox2}$ , four new elements ( $L_{sub1}, L_{sub2}, R_{loss1}, R_{loss2}$ ) can be extracted easily from  $Z_2$  and  $Z_3$ .

### 3.4.3 Conductor loss and substrate loss effect

In this section, skin effect caused by eddy current in the coil metal arising from magnetic field coupling through the substrate return path. In pervious section, conductor loss and substrate loss have the same physical mechanisms. Due to the non-zero resistivity of the metal layers there are ohmic losses in the metal traces as well as eddy current losses. The eddy currents in the metal traces arise from the magnetic fields generated by the device that penetrate the metal layers. These magnetic fields induce currents that give rise to a non-uniform current distribution along the width and thickness of conductors pushing current to the outer skin of the conductors. These effects are also known as skin and proximity effects. So in our research model, we have already included these effects. In T-model,  $R_p$  represent conductor loss due to eddy current arising from magnetic field coupling through substrate return path. In improved T-model, the major enhancement is the deployment of three branches of paralld RL elements using a T-shape configuration to emulate the 3D eddy current effect. However, electromagnetically induced substrate currents flow in the substrate and are a source of loss.

### 3.4.4 Varying substrate resistivity effect

Regarding substrate resistivity effect on inductors' frequency response and performance, EM simulation using ADS Momentum with extensive calibration is conducted to accurately predict the broadband characteristics under wide range of substrate resistivities ( $\rho_{si} = 0.05 \sim 1K\Omega -cm$ ). Three operation models such as TEM,



slow-wave, and eddy current are presented. The improved T-model parameters manifest themselves physics-base through relevant correlation with  $\rho_{si}$  over three operation modes. In this section, we will use ADS Momentum simulation with extensive calibration conducted to predict the broadband characteristics under varying  $\rho_{si}$ . Figure 3.47 indicate good math between ADS Momentum, measurement, and T-model in terms of  $S_{11}$ ,  $S_{21}$ ,  $L(\omega)$ ,  $R_e(Z_{in}(\omega))$ , and  $Q(\omega)$  fro inductors on standard substrate of  $\rho_{si} = 10\Omega -cm$ . We find one reference to discuss above mention. It divide to three operation modes, such as TEM, slow wave, and eddy current corresponding to wide range of  $\rho_{si}$  ( $0.05 \sim 1K\Omega -cm$ ).

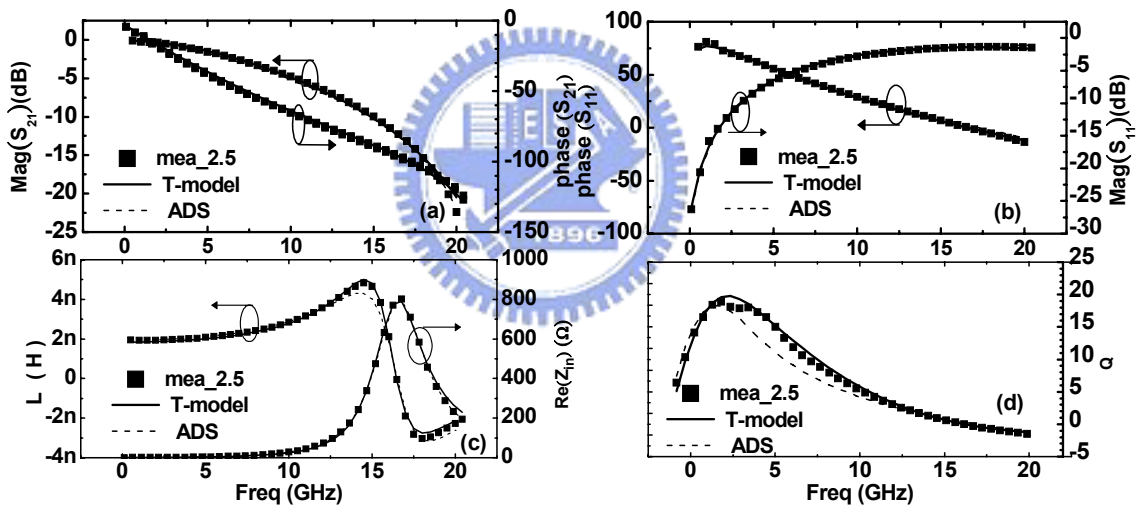


Figure 3.47 Comparison between ADS momentum simulation, measurement, and improved T-model for on-chip inductor (a)  $S_{11}$  (mag, phase) (b)  $S_{21}$  (mag, phase) (c)  $L(\omega)$ ,  $R_e(Z_{in}(\omega))$  (d)  $Q(\omega)$

Figure 3.48 (a)-(d) show  $Q_m$ ,  $f_m$ ,  $f_{Lmax}$ , and  $f_{SR}$  as function of  $\rho_{si}$ .  $Q_m$  is the maximum Q and  $f_m$  is the frequency responsible for  $Q_m$ .  $f_{Lmax}$  is the frequency corresponding to maximum L. Interesting result is identified in region of  $\rho_{si} = 0.05 \sim 10$

$\Omega$ –cm. where  $f_{SR}$  drops monotonically with reducing  $\rho_{si}$  while  $Q_m$  reveals a hump due to initial increase and then drop with further reduction of  $\rho_{si}$ . The drop of  $f_{SR}$  and increase of  $Q_m$  suggest that the spiral coil is getting into resonator mode, i.e. slow-wave model. As for high resistivity region of  $\rho_{si} > 10 \Omega$ –cm,  $f_{SR}$  saturates at maximum while  $Q_m$  increases continuously with  $\rho_{si}$ . This region is so called TEM model or inductor model, which favors inductor operation with high Q attributed to suppressed resonance in substrate of dielectric property. Regarding the very low resistivity of  $\rho_{si} < 0.5 \Omega$ –cm,  $f_{SR}$  saturates at minimum and  $Q_m$  drops drastically. The spiral coil is driven into eddy current model or skin effect mode where  $\rho_{si}$  is so small that the skin depth is thinner than the substrate thickness and becomes the limiting factor. In the following, improved T-model parameters are extracted from the simulated S-parameters under various  $\rho_{si}$  to verify if the model parameters can reflect the physical properties responsible for the three modes of operation.

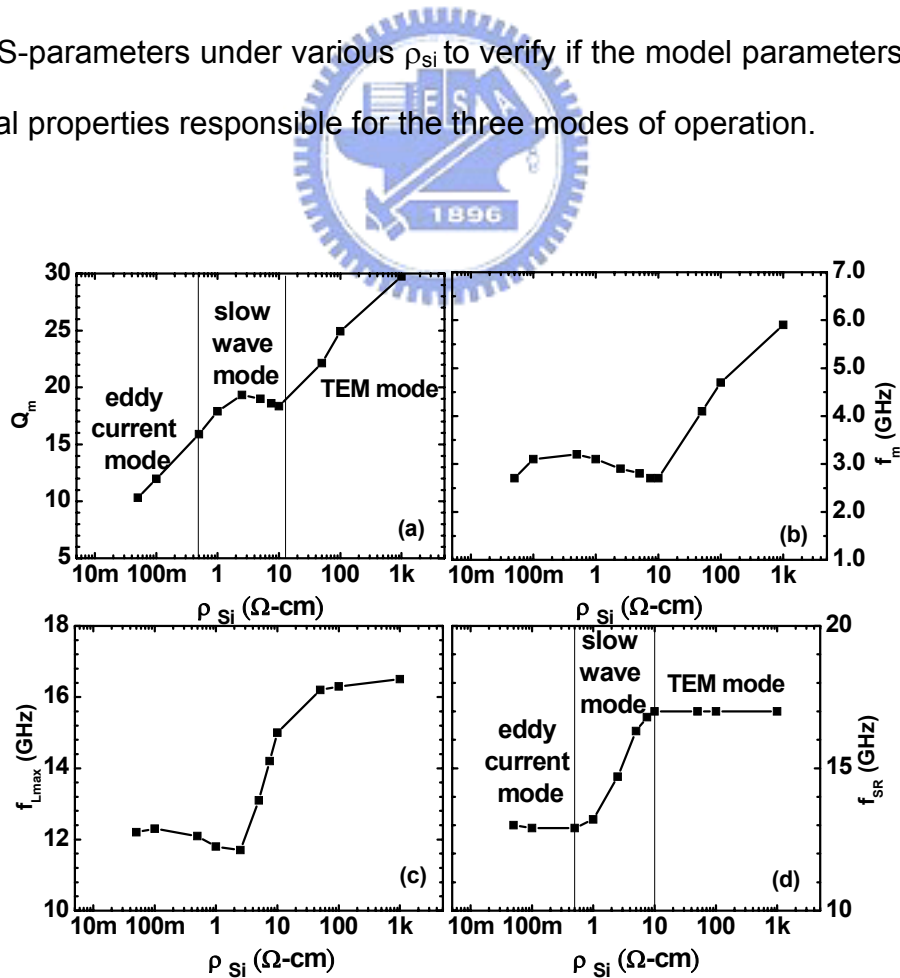


Figure 3.48 (a)  $Q_m$  (b)  $f_m$  (c)  $f_{Lmax}$  (d)  $f_{SR}$  under varying  $\rho_{si}$  (0.01 ~ 1K  $\Omega$ –cm) predicted

by ADS Momentum simulation

Figure 3.49 indicate how the resistive elements ( $R_p$ ,  $R_{sub}$ ,  $R_{loss}$ ,  $R_{loss1}$ ,  $R_{loss2}$ ) and inductive elements ( $L_{sub}$ ,  $L_{sub1}$ ,  $L_{sub2}$ ) vary with varying  $\rho_{si}$ . Quite interestingly,  $R_p$  just follows exactly the same trend as that of  $Q_m$  vs.  $\rho_{si}$  with a hump in slow-wave model while the others show monotonic increase with  $\rho_{si}$  in slow-wave and TEM modes and near saturation in eddy current mode. Regarding the capacitive elements ( $C_p$ ,  $C_{sub}$ ,  $C_{ox1}$ ,  $C_{ox2}$ ) in figure 3.48 (c)-(d), all four capacitances demonstrate monotonic increase with reduction of  $\rho_{si}$  in slow-wave mode, saturation in TEM mode while different behaviors in eddy current mode. The larger capacitances associated with lower  $\rho_{si}$ . Concerning the RLC model parameter effect in determining  $Q_m$  and  $f_{SR}$  over the wide range of  $\rho_{si}$ , figure 3.50 reveal a monotonic increase of  $Q_m$  due to increase of  $R_p$  while hump appears for other resistive or inductive elements such as  $R_{sub}$ ,  $R_{loss}$  and  $L_{sub}$  corresponding to the region of slow-wave mode. The result supports an important point that  $R_p$ , a new element introduced in our T-model is the key parameter to explicitly guide substrate engineering for on-Si-chip inductor to achieve maximum  $Q_m$ . Figure 3.51 present the capacitances' ( $C_p$ ,  $C_{sub}$ ,  $C_{ox1}$ ,  $C_{ox2}$ ) effect on  $f_{SR}$  where monotonic increase of  $f_{SR}$  with lowering capacitance is demonstrated for all four capacitances.

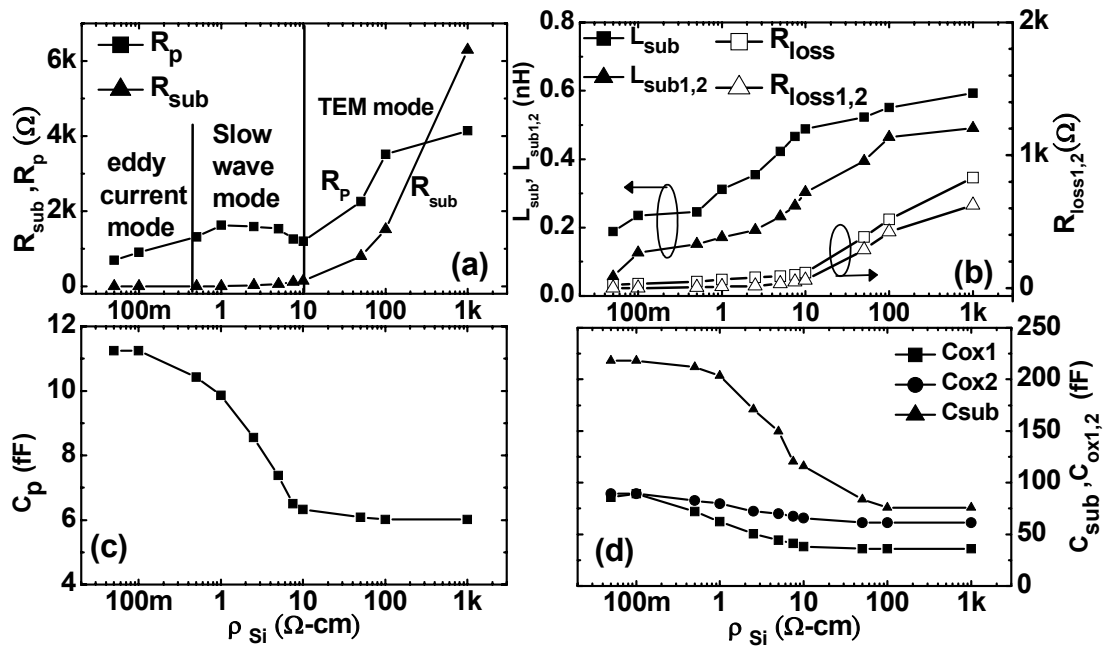


Figure 3.49 Improved T-model parameters under varying  $\rho_{Si}$  (a)  $R_{sub}$ ,  $R_p$  (b)  $L_{sub}$ ,  $L_{sub1,2}$ ,

$R_{loss}$ ,  $R_{loss1,2}$  (c)  $C_p$  (d)  $C_{ox1,2}$   $C_{sub}$

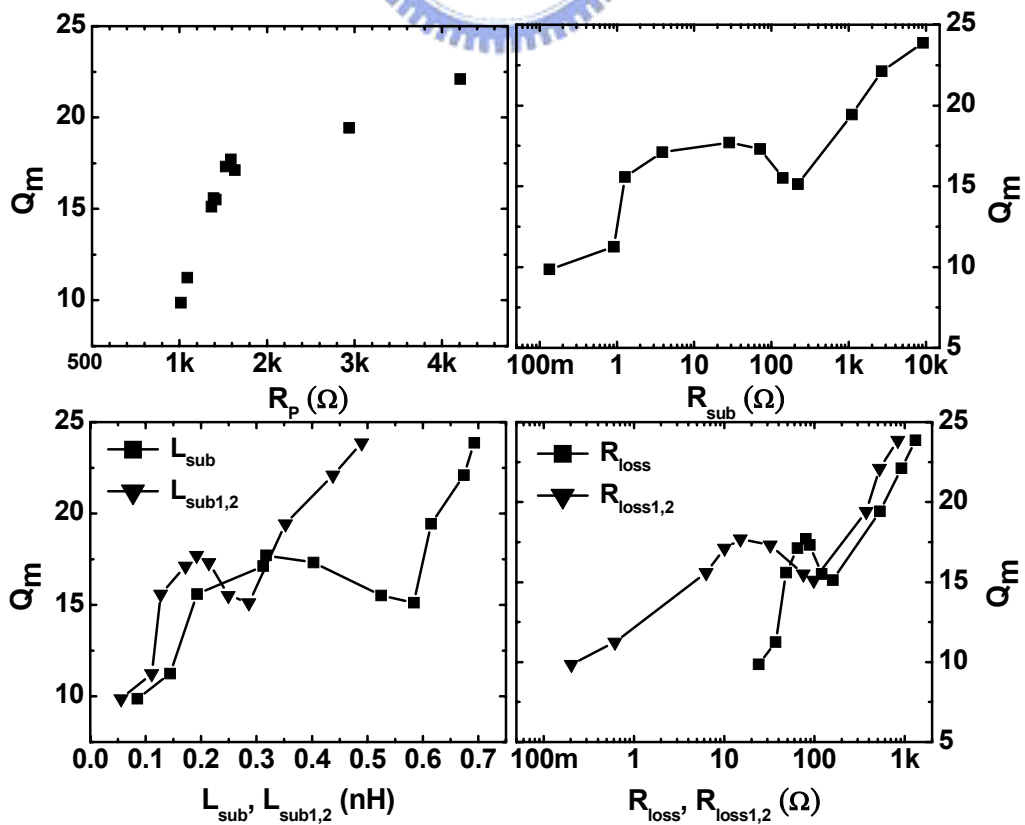
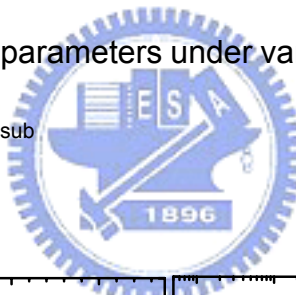


Figure 3.50  $Q_m$  vs. Improved T-model parameters under varying  $\rho_{si}$  (a)  $R_p$  (b)  $R_{sub}$ , (c)  $L_{sub}$ ,  $L_{sub1,2}$  (d)  $R_{loss}$ ,  $R_{loss1,2}$

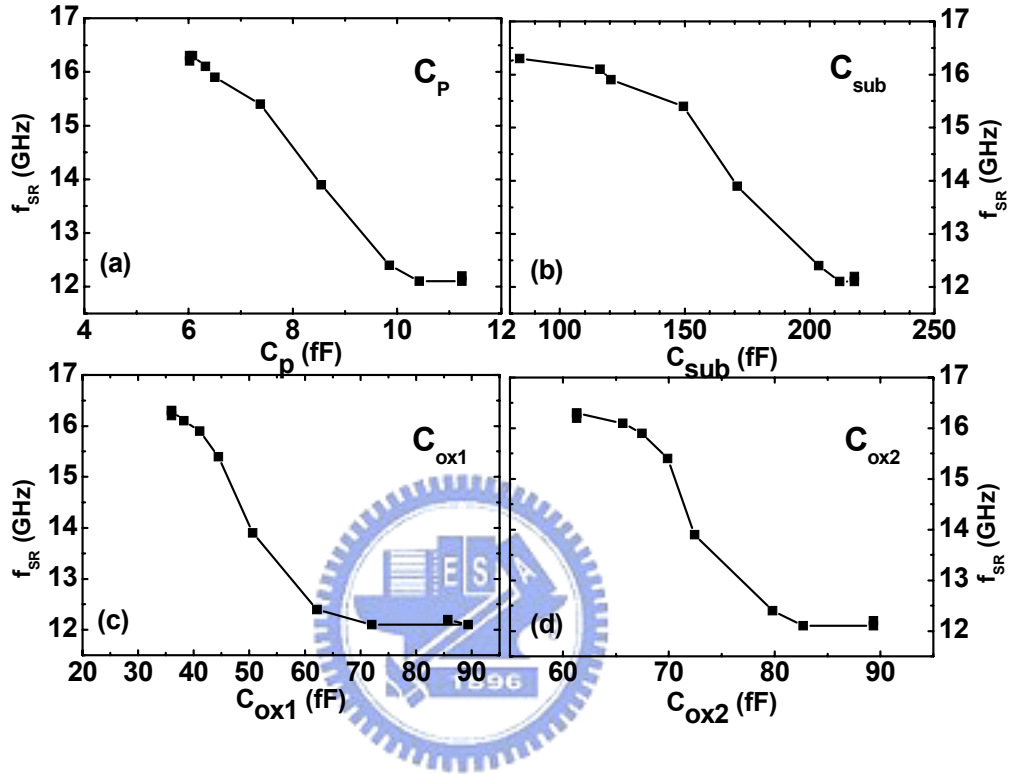


Figure 3.51  $f_{SR}$  vs. Improved T-model parameters under varying  $\rho_{si}$  (a)  $C_p$  (b)  $C_{sub}$ , (c)  $C_{ox1}$  (d)  $C_{ox2}$

### 3.4.5 Broadband accuracy

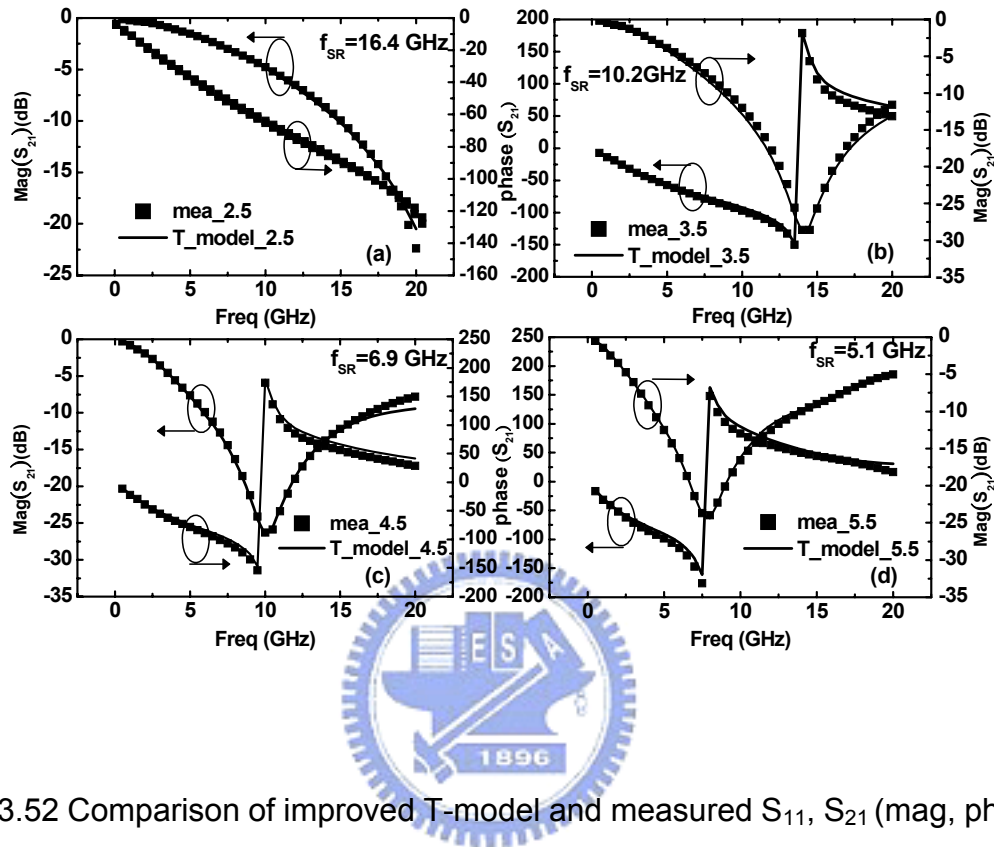


Figure 3.52 Comparison of improved T-model and measured  $S_{11}$ ,  $S_{21}$  (mag, phase) for inductors. Coil numbers (a)  $N=2.5$  (b)  $N=3.5$  (c)  $N=4.5$  (d)  $N=5.5$

The improved T-model has been verified by comparison with measurement in terms of S-parameters ( $S_{11}$ ,  $S_{21}$ ),  $L(\omega)$ ,  $R_e(Z_{in}(\omega))$ , and  $Q(\omega)$  over up to 20GHz. Figure 3.52 (a) ~ (d) indicate the comparison for magnitude and phase of  $S_{11}$  and  $S_{21}$  between the model and measurement. According to figure 3.52, match is achieved for all coil numbers even beyond resonance, which happened at  $f_{SR} \ll 20\text{GHz}$  for larger coil number ( $N=3.5, 4.5, 5.5$ ). It is an obvious improvement over the original T-model and even better match is achieved as compared to EM simulation (figure 3.47). All three parameters are frequency dependent that is critically related to the spiral conductor loss and  $S_i$  substrate loss. Figure 3.53 (a) ~ (d) can accurately fit to the

measured  $L(\omega)$ , and  $\text{Re}(Z_{in}(\omega))$  by the improved T-model for all inductors operating up to 20 GHz. Besides, the model can exactly capture the full band behavior of  $\text{Re}(Z_{in}(\omega))$  even beyond resonance such as the dramatic increase prior to resonance, peak at resonance, and the curve drop after the peak. And  $Q(\omega)$  is the most important parameter governing RF IC performance. Figure 3.53 (d) shows the excellent match with the measured  $Q(\omega)$  over broadband of 20 GHz.

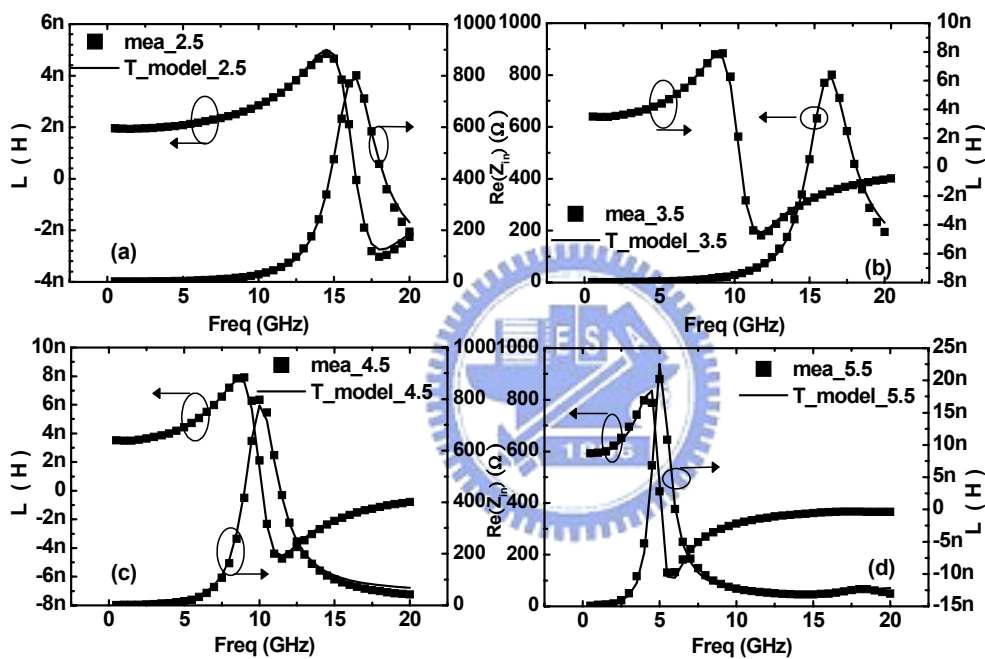


Figure 3.53 Comparison of improved T-model and measured  $L(\omega)$ ,  $\text{Re}(Z_{in}(\omega))$  for inductors. Coil numbers (a)  $N=2.5$  (b)  $N=3.5$  (c)  $N=4.5$  (d)  $N=5.5$

### 3.4.6 Scalability

Another important feature is the good scalability w.r.t dimension for all model parameters. Figure 3.54 (a) ~ (d) illustrates present good match with a linear function of coil numbers for each model parameter. These parameters represent the spiral coil's RLC network. Figure 3.55 (a) ~ (d) illustrates also present good match with a linear function of coil numbers that have been involved model parameters,  $C_{sub}$ ,  $1/R_{sub}$ ,  $L_{sub1}$ ,  $L_{sub2}$ ,  $R_{loss}$ ,  $R_{loss1}$ ,  $R_{loss2}$ . These parameters have proven scalability and these also suggests that T-model can be used for pre-layout simulation and optimization.

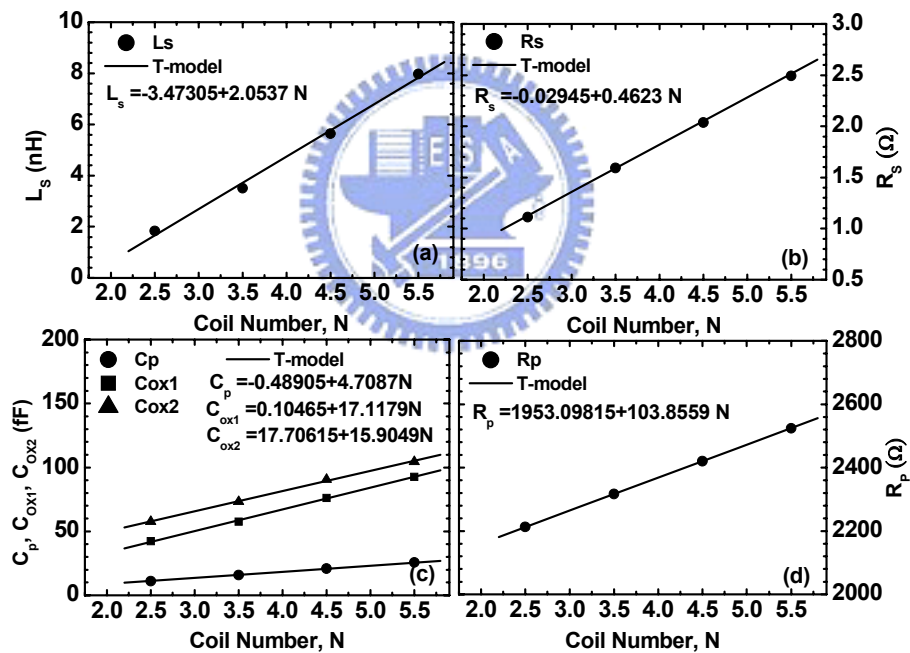


Figure 3.54 Improved T-model parameters vs. coil number (a)  $L_s$ ,  $C_p$ ,  $C_{ox1,2}$  (b)  $R_s$ ,  $R_p$  (c)  $C_{sub}$ ,  $L_{sub}$ ,  $L_{sub1,2}$  (d)  $1/R_{sub}$ ,  $R_{loss}$ ,  $R_{loss1,2}$



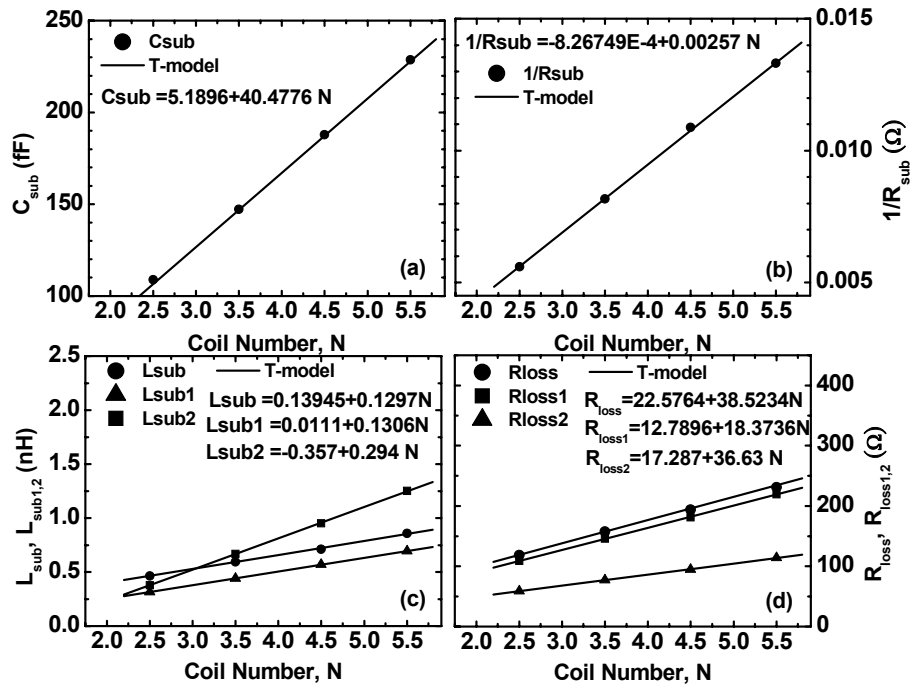
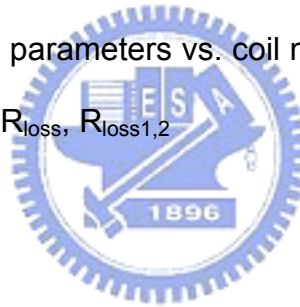


Figure 3.55 Improved T-model parameters vs. coil number (a)  $L_s, C_p, C_{ox1,2}$  (b)  $R_s, R_p$  (c)  $C_{sub}, L_{sub}, L_{sub1,2}$  (d)  $1/R_{sub}, R_{loss}, R_{loss1,2}$



# Chapter 4

## Symmetric Inductor Model Development and Verification

### 4.1 Symmetric inductor design and fabrication - Motivation

Inductor is a critical device for RF circuits such as voltage-controlled oscillators (VCO), Impedance matching networks and RF amplifiers. Its characteristics generally crucially affect the overall circuit performance. In recent years, for RFIC design, the passive devices of symmetric structures such as symmetric/differential inductors and varactors are increasingly popular, e.g. the requirements for VCO design to reduce the phase noise. The differential excitation (i.e., voltages and currents of two signals are 180 degree out of phase but with the same magnitude) has become an important operation mode in high-performance mixed-signal and RF circuits. It has the advantage of better immunity to environmental noise. The inductor with symmetrical geometry (differential inductor) is designed for this kind of circuit applications, which are of special concern for matching, common mode rejection, and noise immunity, etc.

#### 4.1.1 New symmetric inductor design strategy

The conventional differential inductor is not really symmetrical in geometry. In figure 4.1, we have to use the top metal to crossover the second to top metal at the intersection. The two signals would no longer be 180 degree out of phase after they flew through the intersection since they have passed different paths and materials. For certain applications, circuit designer has to use a differential inductor with center-tap but the center-tap of the conventional differential inductor that we defined is

not the real center. We cannot even know where the exact center is.

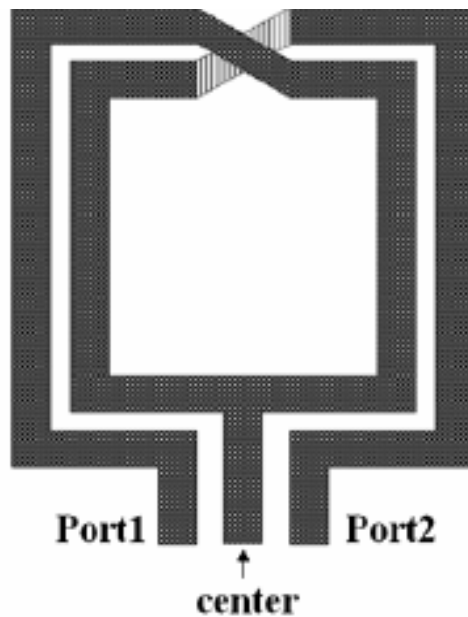


Figure 4.1 Top view of a conventional differential inductor.



To overcome the mentioned drawbacks suffered by the conventional symmetric inductors, a new symmetric inductor of improved geometry design was proposed in this work. Figure 4.2 illustrates the new symmetrical inductor we proposed. Its layout is fully symmetrical in geometry and electricity and the center tap as defined is no doubt to be the real center. The objectives of this work are two folds. The first one is to fabricate a fully symmetrical inductor with exactly identical characteristics at two ports to be suitable for RF circuit design and optimization. The second one is to develop an accurate de-embedding method for intrinsic device parameter extraction. For the mentioned purpose, a two-port inductor of fully symmetric structure as proposed was fabricated using tsmc 0.13um RF CMOS process to realize Q value equality at two ports.

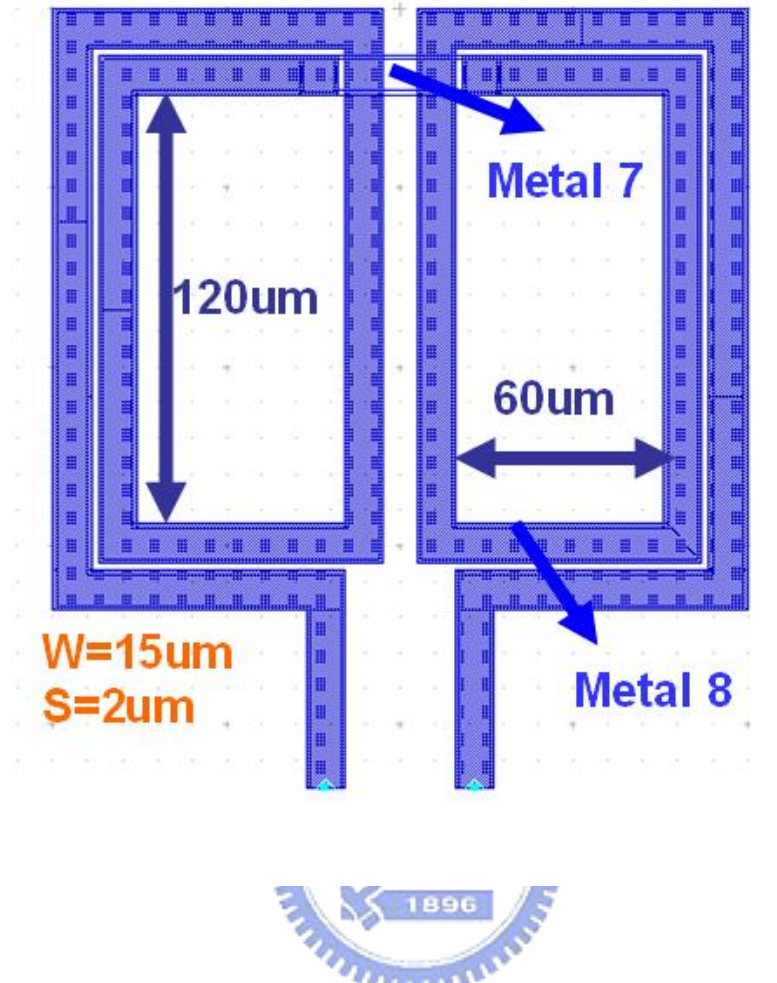


Figure 4.2 Top view of a fully symmetrical inductor

In this work, 0.13  $\mu\text{m}$  RF CMOS process was adopted to fabricate fully symmetrical inductors. Totally, eight layers of metal by Cu are available and the top metal (M8) thickness is 3  $\mu\text{m}$ . The proposed new symmetric inductor as shown in figure 4.2 can solve the asymmetry problem suffered by conventional symmetric inductors. However, through EM simulation, we find that the fully symmetrical inductors will suffer worse quality factor as compared with the conventional ones. It is because that signal currents associated with port 1 and port 2 flow in opposite directions, and hence, sufficient separation between two adjacent spiral coils is required to reduce the negative mutual magnetic coupling between the two inductors.

Assisted by EM simulation, layout geometry modification and optimization can be done to reduce the mentioned negative mutual magnetic coupling. As stated previously, a pair of asymmetric inductors must be spaced far enough apart to limit unwanted coupling (both magnetic and electric) between the inductor pair. This is one of the reasons responsible for chip area increase. Corresponding to the coil area increase, its parasitic capacitance and series resistance also increase. Due to the mentioned reasons, we can estimate the degradation of key performance parameters such as  $f_{SR}$  and  $Q$  (quality factor). In the following section, we will discuss how to do the layout optimization through EM simulation for fully symmetric inductors.

#### 4.1.2 EM simulation for layout optimization

The fully symmetric spiral inductor in figure 4.2 is designed for differential excitation (i.e., voltages and currents at port1 and port2 are 180 degree out of phase) and to ensure identical impedance at port1 and port2. When driven differentially, the voltages on adjacent conduction strips are anti-phase. To overcome the mentioned performance degradation potentially suffered by new symmetric inductor, taper structure of varying strip width is adopted for the proposed inductor. First, we discuss its theory. ADS Momentum simulation with extensive calibration is conducted to predict the broadband characteristics (Refer to chapter 3). Varying metal strip width will lead to the trade-off between the maximum  $Q$ , i.e.  $Q_{max}$  and the corresponding frequency,  $f_{max}$ . EM simulation results shown in figure 4.3 indicate that metal strip width increase from 5  $\mu\text{m}$  to 15  $\mu\text{m}$  leads to  $Q_{max}$  increase from 22 to around 25 while  $f_{max}$  decrease from 5.4 GHz to 3.7 GHz. The simulation reveals a compromised point at around 8  $\mu\text{m}$ , i.e. between 7  $\mu\text{m}$  and 9  $\mu\text{m}$  and suggests that optimization can be done through the taper structure with narrower metal strip in inner coils and wider one

in the outer coils.

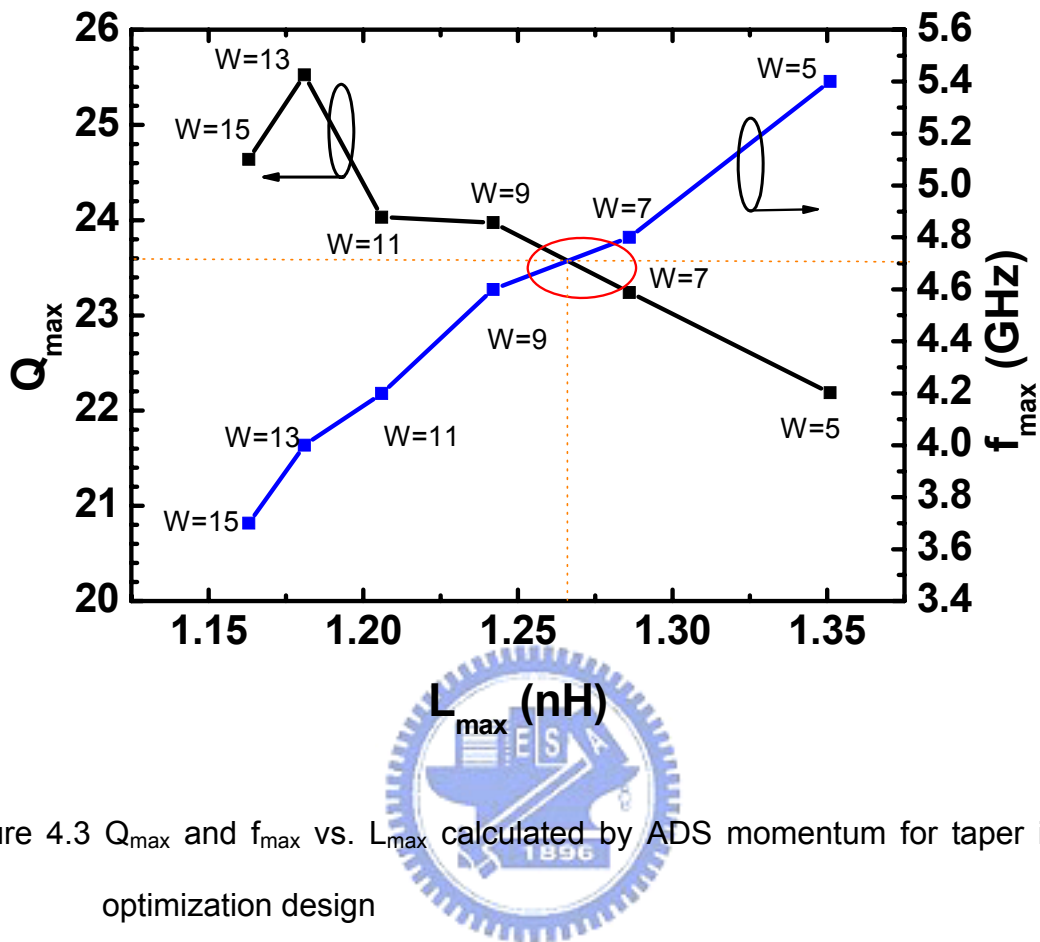


Figure 4.3  $Q_{max}$  and  $f_{max}$  vs.  $L_{max}$  calculated by ADS momentum for taper inductor optimization design

Following previous description, further analysis is done on the simulation results in terms of width effect on inductance corresponding to  $Q_{max}$ , given by  $L_{max}$ . The increase of  $L_{max}$  with decreasing metal strip width suggests that the inductance is primarily determined by the magnetic flux outside of the metal wires and enclosed by coils. The simulation results also suggests that the variation in the wire cross-section dimensions has little contribution to the magnetic flux and subsequently the inductance. Another important point is that the narrower metal strip, the higher  $f_{max}$ . It accounts for the smaller area covered by the spiral coils and then the smaller coupling capacitance. The optimization target for inductor design is to enhance  $Q$  and maintain the self-resonance frequency ( $f_{SR}$ ) as high as possible. Taper structure with gradual

variation of metal strip width is proposed to increase the inductance, reduce the coupling capacitance, and minimize increase of resistance simultaneously. In this way, the optimization target of high Q and sufficiently large  $f_{SR}$  can be achieved. Figure 4.4 depicts the taper and fully symmetric inductor of our design for fabrication and for verification through EM simulation (ADS momentum).

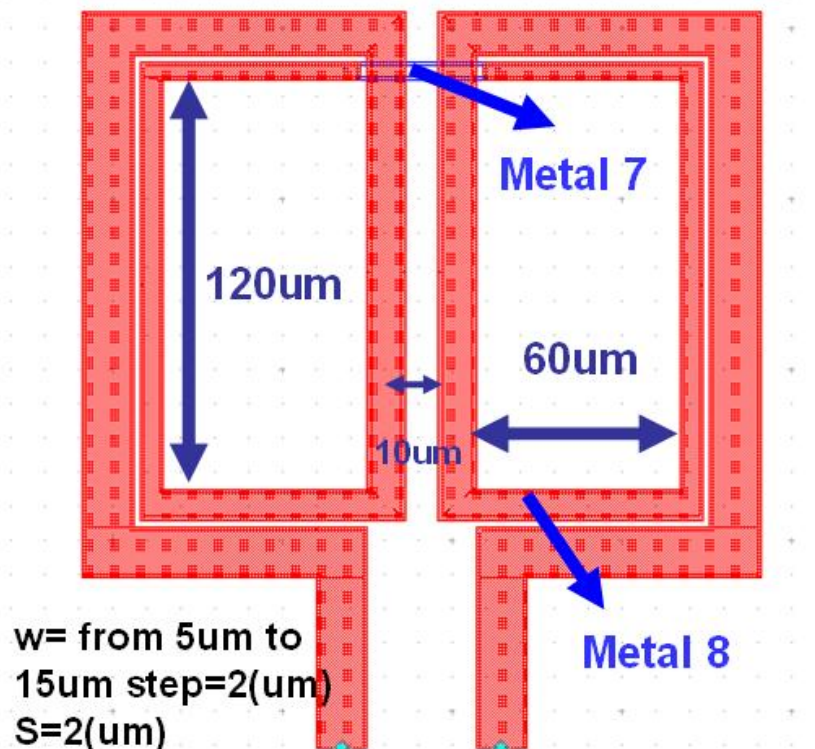


Figure 4.4 Fully taper symmetry inductor layout

### 4.1.3 Layout parameter and geometry analysis

#### – taper structure

Fully taper symmetric inductor of rectangular coils were fabricated by 0.13  $\mu\text{m}$  back end process with eight layers of Cu and low-k inter-metal dielectric (FSG,  $K=3.8$ ).

The top metal of  $3\mu\text{m}$  Cu was used to implement the spiral coils of varying strip widths as shown in figure 4.4. The inner radiuses of the rectangular coil at both sides are  $60\ \mu\text{m}$  along x-axis and  $120\mu\text{m}$  along y-axis. The metal strip width of each segment varies from the narrowest one,  $5\mu\text{m}$  at inner coils to the widest one,  $15\mu\text{m}$  at outer coils. The segment number is seven to given coil number of 1.75 and the width variation step is  $2\mu\text{m}$ . The physical inductance values at sufficiently low frequency are around  $0.6 \sim 1.86\ \text{nH}$  corresponding to inner radiuses  $R= 30 \sim 90\ \mu\text{m}$ . S-parameter were measured by using Agilent network vector analyzer up to 20 GHz and new de-embedding as mentioned has been carefully done to extract the truly intrinsic characteristics for model parameter extraction and scalable model build up.

#### 4.1.4 Comparison with conventional symmetric inductors

The conventional symmetric inductors is realized by joining groups of coupled metal lines from one side of an axis of symmetry to the other using a number of cross-over and cross-under connections. This connection method may cause port 1 and port 2 to be not equivalent, especially for  $S_{11}$  and  $S_{22}$ . This style of winding was generally applied to monolithic transformers for coupling both primary and secondary coils but this kind of layout suffers some inconvenience for metal connection from port 3 to other components. The fully symmetric inductor of new layout design was proposed and fabricated to solve the mentioned weakness. Verification will be done by checking the equivalence of  $S_{11}$  and  $S_{22}$ , particularly the phase portion. The improved symmetry is one of major reasons why we adopted this new structure. (refer to figure 4.4). One major advantage provided by the new symmetric inductor is the easy extension from 2-port to 3-port scheme for applications of differentially driven circuit design. The inductor quality factor (Q) can be significantly enhanced through



operation mode of differential excitation as compared to the conventional single end scheme.

For a symmetric inductor designed for differential excitation, the voltage and current at port -1 and port-2 are  $180^\circ$  out of phase. The symmetric inductor excited differentially can realize a substantially higher Q. It has been recognized that the quality factor an inductor is higher when driven differentially than subject to single-ended excitation. The mechanism responsible for Q enhancement is due to the reduced substrate loss under balanced excitation. A natural field of applications of such kind of inductors is the tank circuit of differential VCOs where the center tap is used for biasing and the capacitances are connected across the symmetric terminals. Previous work reported that use of differentially driven symmetric inductor can reduce the total VCO area by 35% compared to a design using two conventional spiral inductors. an additional benefit is the improved electrical performance due to the increased tank impedance caused by higher Q. Accordingly, a larger output voltage swing and a reduced phased noise can be achieved.

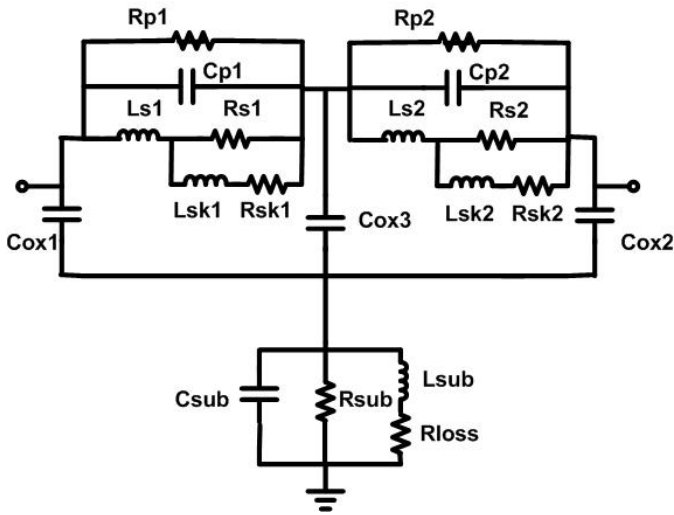
## 4.2 Symmetric inductor model development

For computer-aided design (CAD) purposes, a lumped-element equivalent or SPICE-compatible model is needed to predict the large signal performance of an RF circuit correctly. The lump element sub-circuit in the scalable RF model is developed. In this section, a new symmetric inductor model has been developed to accurately simulate the broadband characteristics of on-Si-chip symmetrical inductors, up to 20GHz. Good match with the measured S-parameter,  $L(\omega)$ ,  $\text{Re}(Z_{in}(\omega))$ , and  $Q(\omega)$  proves the proposed 2T-model. Besides, in order to quantify the improvement in Q factor of the differentially driven symmetric design, we also built differential model in

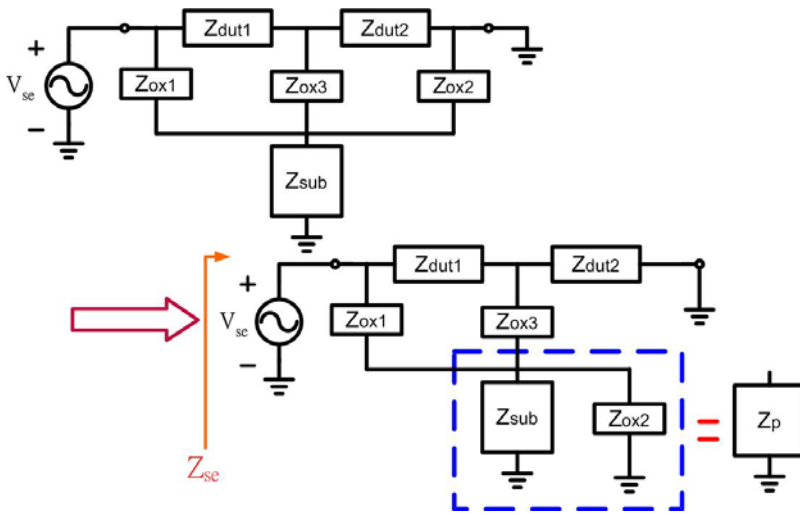
2T-model. The broadband feature and scalability have been justified by good match with a linear function of inner radius for all model parameters employed in the RLC network. A parameter extraction flow is established through equivalent circuit analysis to enable automatic parameter extraction and optimization. In next section, we will discuss them in detail.

### 4.2.1 Model parameter extraction flow

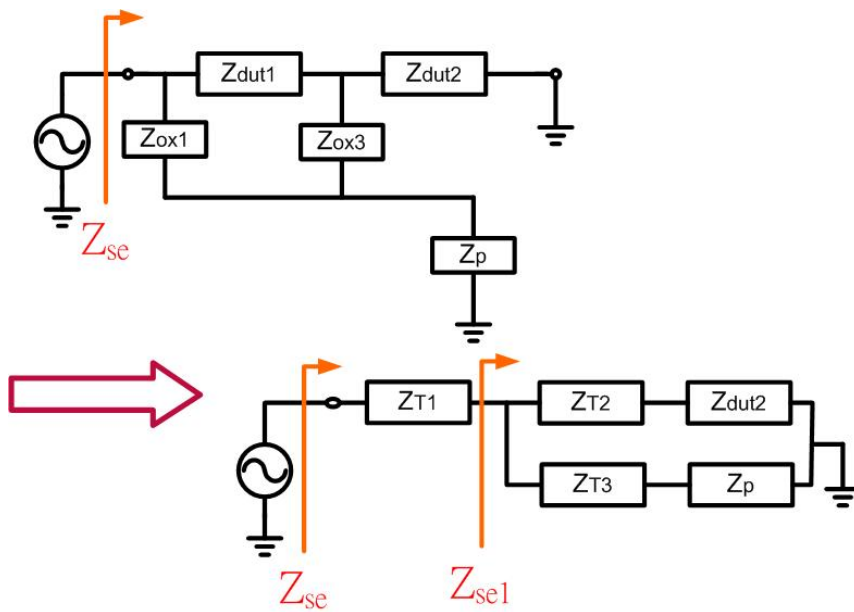
In this section, we extend the parameter extraction flow from previously T-model for spiral inductors to 2T model for symmetric inductors. All the unknown R, L, C parameters will be extracted from the analytical equations derived through equivalent circuit analysis as shown in figure 4.37. The analytical equations are composed of Z-parameters and Y-parameters listed in the first block of extraction flow illustrated in figure 4.38, which can be easily transformed from the measured S-parameters after appropriate de-embedding developed for this fully symmetric inductor. Under the condition that the number of unknown elements is larger than the number of equations, approximation valid under very low or very high frequency is generally made to remove some unknown elements and extract the remaining ones as the first step. Then we can extract the others at the second step and go for optimization. According to the necessary approximation, the extracted R,L,C parameters in the first procedure of flow (figure 4.38) are generally not exactly the correct solutions but all unknown parameters must be given the initial guess for further optimization through best fitting to the measured S-parameters,  $L(\omega)$ ,  $\text{Re}(Z_{in}(\omega))$ , and  $Q(\omega)$ .



(a)



(b)



(c)

Figure 4.5 2T model for fully taper symmetric inductor (a) equivalent circuit schematics (b) intermediate stage (c) final stage of block diagram for circuit analysis

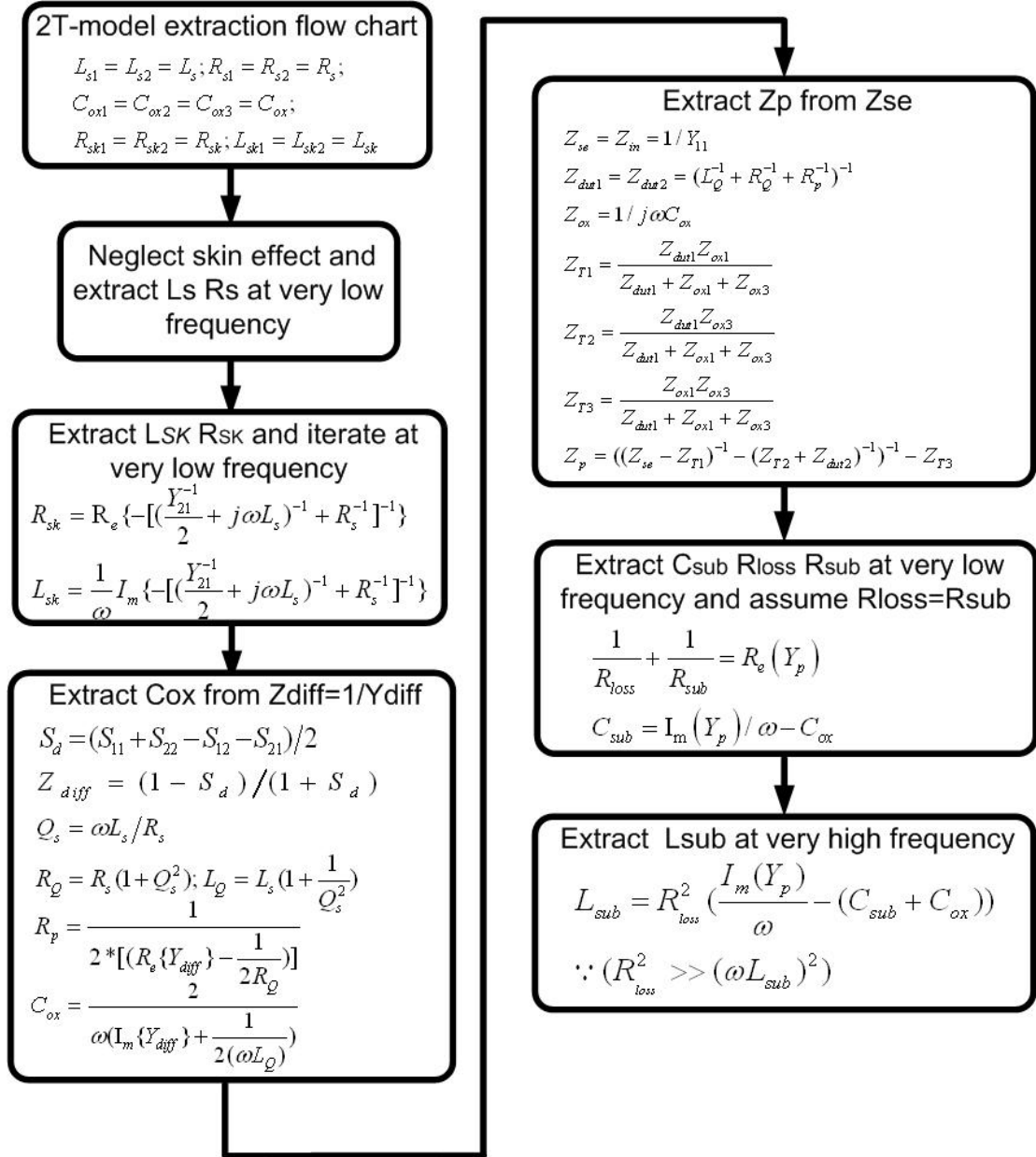


Figure 4.6. 2T-model parameter derivation formulas and extraction flow chart.

As a result, all the physical elements composing the model can be extracted through the flow shown in figure 4.38. Attributed to the symmetric nature, all the elements appearing at both sides are assumed equal to simplify the problem, i.e.

$L_s=L_{s1}=L_{s2}$ ,  $R_s=R_{s1}=R_{s2}$ ,  $L_{sk}=L_{sk1}=L_{sk2}$ ,  $R_{sk}=R_{sk1}=R_{sk2}$  and  $C_{ox}=C_{ox1}=C_{ox2}=C_{ox3}$ . At the first step, skin effect incorporated elements  $R_{sk}$  and  $L_{sk}$  are neglected, then  $R_s$  and  $L_s$  representing the physical inductor under very low frequency can be extracted. After extraction of  $L_s$  and  $R_s$ , the measured Y-parameters ( $Y_{21}$ ) and extracted ( $L_s$ ,  $R_s$ ) are adopted to extract  $L_{sk}$  and  $R_{sk}$ . The ideal quality factor free from conductor and substrate losses, denoted as  $Q_s$  is given by  $Q_s= L_s/R_s$ . After that,  $R_p$  and  $C_{ox}$  can be extracted by close forms as a function of ( $L_s$ ,  $R_s$ ,  $Q_s$ ) and measured  $Y_{diff}=1/Z_{diff}$  (equivalent impedance of differential mode).  $R_p$  is a new element introduced in our 2T-model and it represents conductor loss and Q degradation before resonance ( $\omega < \omega_{SR}$ ).  $C_{ox}$  is one major element to determine self-resonance frequency ( $\omega_{SR}$ ) and can be derived by the equation shown in the flow chart. Then,  $C_{sub}$ ,  $R_{sub}$  and  $R_{loss}$  can be extracted easily from  $Z_{sub}$  under very low frequency and the assumption of  $R_{sub}=R_{loss}$  for initial guess. To the end,  $L_{sub}$  is extracted under very high frequency for initial guess and then ( $R_{sub}$ ,  $R_{loss}$ ,  $L_{sub}$ ,  $C_{sub}$ ) are iterated to obtain the optimized parameters. In table I, the initial guess and optimized value of each parameter corresponding to different radiuses are listed. Herein, the substrate parameters such as  $R_{sub}$ ,  $L_{sub}$ , and  $R_{loss}$  reveal obviously bigger error in the initial guess. The error generally came from the assumption and approximation to simplify the equations for extraction. However, few iterations were required to reach optimization.

<b>R=30</b>	<b>Initial guess</b>	<b>Optimize</b>	<b>Error (%)</b>
$L_s$ ( nH )	0.302	0.249	-21.285%
$R_s$ ( $\Omega$ )	0.458	0.507	9.665%
$L_{sk}$ ( nH )	0.1	0.127	21.260%
$R_{sk}$ ( $\Omega$ )	0.34	0.22	-54.545%
$C_{ox}$ ( fF )	15.11	15.04	-0.465%
$C_{sub}$ ( fF )	14.94	12.682	-17.805%
$R_{sub}$ ( $\Omega$ )	78.865	394.625	80.015%
$R_p$ ( $\Omega$ )	757	773.59	2.145%
$L_{sub}$ (nH)	0.028	0.101	72.277%
$R_{loss}$ ( $\Omega$ )	78.865	76.664	-2.871%

<b>R=60</b>	<b>Initial guess</b>	<b>Optimize</b>	<b>Error (%)</b>
$L_s$ ( nH )	0.568	0.569	0.176%
$R_s$ ( $\Omega$ )	0.52	0.62	16.129%
$L_{sk}$ ( nH )	0.127	0.111	-14.414%
$R_{sk}$ ( $\Omega$ )	0.413	0.324	-27.469%
$C_{ox}$ ( fF )	31.09	34.7	10.403%
$C_{sub}$ ( fF )	30.8	35.458	13.137%
$R_{sub}$ ( $\Omega$ )	41.875	188.635	77.801%
$R_p$ ( $\Omega$ )	828	829.973	0.238%
$L_{sub}$ (nH)	0.0898	0.151	40.530%
$R_{loss}$ ( $\Omega$ )	41.875	60.8	31.127%

<b>R=90</b>	<b>Initial guess</b>	<b>Optimize</b>	<b>Error (%)</b>
<b>L<sub>s</sub> ( nH )</b>	<b>0.975</b>	<b>0.912</b>	<b>-6.908%</b>
<b>R<sub>s</sub> ( Ω )</b>	<b>0.7</b>	<b>0.797</b>	<b>12.171%</b>
<b>L<sub>sk</sub> ( nH )</b>	<b>0.08</b>	<b>0.083</b>	<b>3.614%</b>
<b>R<sub>sk</sub> ( Ω )</b>	<b>0.51</b>	<b>0.437</b>	<b>-16.705%</b>
<b>C<sub>ox</sub>( fF )</b>	<b>43.86</b>	<b>53.326</b>	<b>17.751%</b>
<b>C<sub>sub</sub> ( fF )</b>	<b>45.3</b>	<b>52.55</b>	<b>13.796%</b>
<b>R<sub>sub</sub> (Ω)</b>	<b>24.445</b>	<b>125.98</b>	<b>80.596%</b>
<b>R<sub>p</sub> ( Ω )</b>	<b>913</b>	<b>902.212</b>	<b>-1.196%</b>
<b>L<sub>sub</sub> (nH)</b>	<b>0.12</b>	<b>0.206</b>	<b>41.748%</b>
<b>R<sub>loss</sub> (Ω)</b>	<b>24.445</b>	<b>33.665</b>	<b>27.387%</b>

Table I Comparison with initial guess and optimize and error percentage



## 4.2.2 Broadband accuracy

The 2T-model has been verified by comparison with measurement in terms of S-parameters ( $S_{11}$ ,  $S_{21}$ ),  $Z_{dout1}$ ,  $Z_{dout2}$ ,  $L(\omega)$ ,  $R_e(Z_{in}(\omega))$ , and  $Q(\omega)$  over frequency up to 20 GHz. For differential excitation, the 2T-model has also been verified by comparison with measurement in terms of  $S_d(\omega)$ ,  $L_d(\omega)$ ,  $R_e(Z_d(\omega))$ , and  $Q_d(\omega)$ . Figure 4.39 (a) ~ (d) indicate  $S_{11}$  and  $S_{21}$  in terms of magnitude and phase from measurement and simulation by 2T model. Good agreement is achieved between measurement and 2T-model simulation for all S-parameters. Figure 4.40 presents good match in respect of  $L(\omega)$  and  $R_e(Z_{in}(\omega))$ . It is even better match achieved as compared to 3D EM simulation by Ansoft HFSS (figure 4.23 ~ 4.29). Fig.4.40 (a) illustrates excellent fit to the measured  $L(\omega)$  by 2T model for all symmetric inductors of various R operating up

to 20 GHz. The transition from inductive to capacitive mode evoked by increasing frequency beyond  $f_{SR}$  is accurately reproduced by 2T model. Regarding  $\text{Re}(Z_{in}(\omega))$ , pretty good match between 2T model and measurement is shown in Fig.4.40 (b). 2T model can exactly capture the full band behavior of  $\text{Re}(Z_{in}(\omega))$  even beyond resonance such as dramatic increase prior to resonance, peak at resonance, and then sharp drop after the peak. Moreover, the 2T-model has a new feature created to simulate single-end and differential modes' performance by a unified model parameters. In this way, it can reduce circuit simulation time. Figure 4.41 (a) ~ (d) exhibits good fit to measurement in terms of  $S_d$ ,  $L_d$ , and  $\text{Re}(Z_d)$  corresponding to differential excitation mode. Comparison between the single-end excitation in figure 4.40 and differential mode in figure 4.41 reveals obviously higher  $f_{SR}$  for differential mode with delayed impedance sign change from inductive to capacitive mode. Figure 4.42(a)~(d) indicate the symmetric inductor coil impedance,  $Z_{dut1}$  and  $Z_{dut2}$  extracted from measurement after justified new de-embedding and calculated by 2T model using the optimized parameters. Good match is achieved between measurement and 2T model for both  $Z_{dut1}$  and  $Z_{dut2}$  in terms of real and imaginary parts for  $R=30$  and  $60 \text{ m}$  over full range of frequency up to 20GHz. As for the largest inductor with  $R=90 \text{ m}$ , good fit is maintained for  $\text{Re}(Z_{dut1})$  and  $\text{Re}(Z_{dut2})$  over 20GHz bandwidth but visibly larger deviation is identified for  $\text{Im}(Z_{dut1})$  and  $\text{Im}(Z_{dut2})$  at higher frequency, above 15GHz. Quality factors corresponding to single-end and differential modes defined as  $Q(\omega)$  and  $Q_d(\omega)$  are two of most important parameters for symmetric inductors in circuit applications. Figure 4.43 shows good match with the measured  $Q(\omega)$  and  $Q_d(\omega)$  by 2T model over broadband of 20 GHz. The good fit to the peak  $Q$  and capture of full band behavior for various  $R$  suggests the advantage of our 2T-model compared to the existing  $\pi$ -model or  $2\pi$ -model. Self-resonance frequencies  $f_{SR}$  are key parameters accompanying with  $Q(\omega)$  and  $Q_d(\omega)$  to quantify the useful



bandwidth. In 2T-model,  $f_{SR}$  can be accurately predicted by full equivalent circuit simulation. The extension verification proves the broadband accuracy of our 2T model and validate its applications for RF circuit simulation and design in which symmetric inductors will be adopted with single-end or differential configurations.

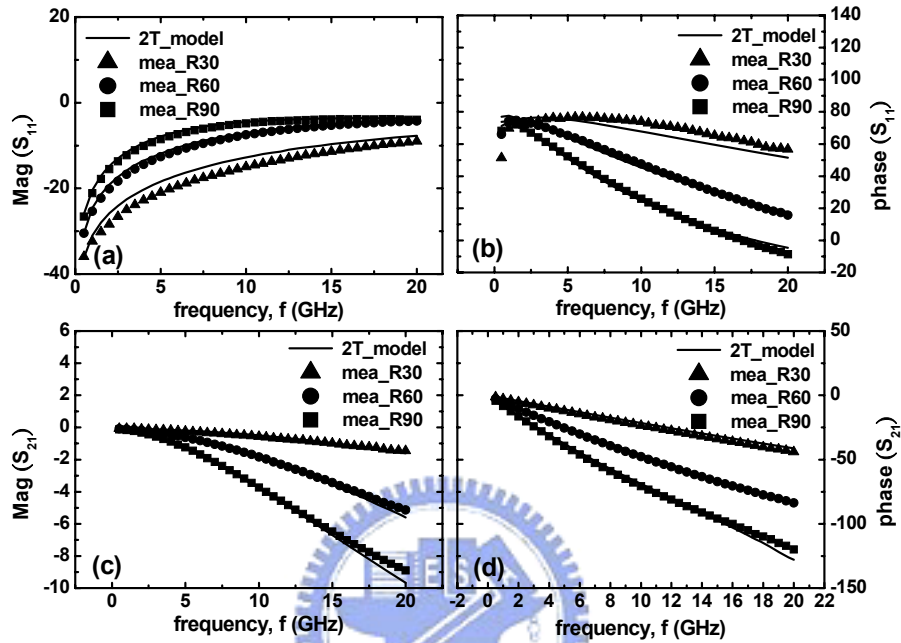


Figure 4.7. Comparison of 2T-model and measurement for R=30, 60, 90 μm (a) Mag (S<sub>11</sub>) (b) Phase (S<sub>11</sub>) (c) Mag (S<sub>21</sub>) (d) Phase (S<sub>21</sub>)

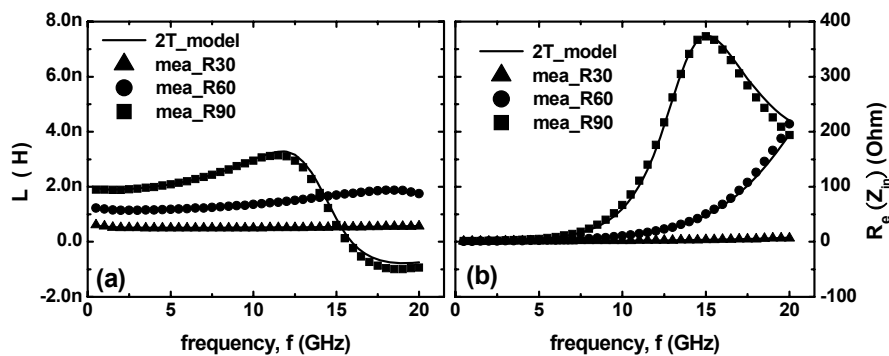


Figure 4.8. Comparison of 2T-model and measurement under single-ended excitation for R=30, 60, 90 m (a) L (ω) (b) Re(Z<sub>in</sub>(ω))

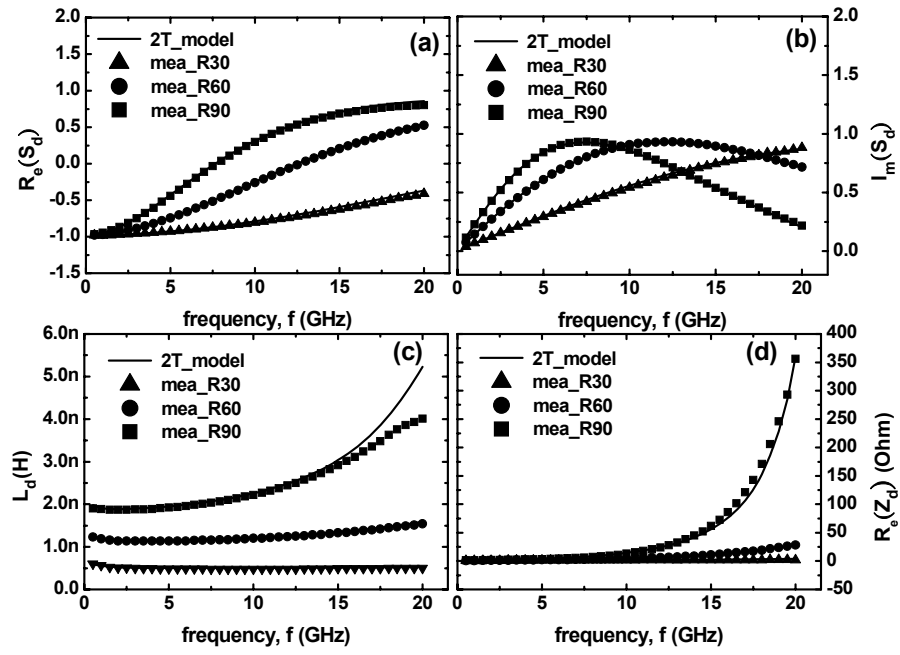


Figure 4.9. Comparison of 2T-model and measurement under differential excitation for  $R=30, 60, 90 \mu\text{m}$  (a)  $R_e(S_d)$  (b)  $I_m(S_d)$  (c)  $L_d(\omega)$  (d)  $R_e(Z_d(\omega))$

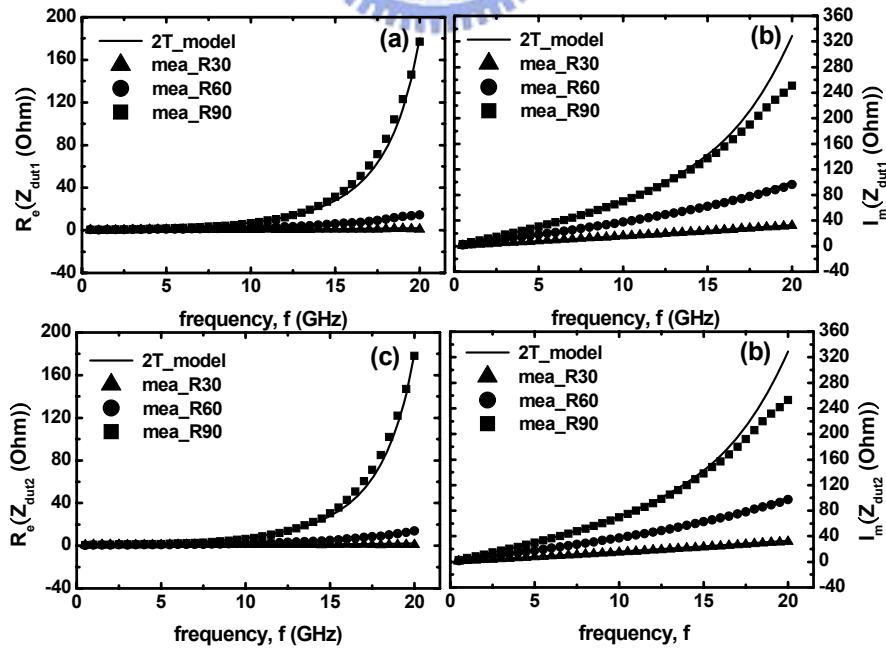


Figure 4.10. Comparison of 2T-model and measurement for  $R=30, 60, 90 \mu\text{m}$  (a)  $R_e(Z_{dut1}(\omega))$  (b)  $I_m(Z_{dut1}(\omega))$  (c)  $R_e(Z_{dut2}(\omega))$  (d)  $I_m(Z_{dut2}(\omega))$

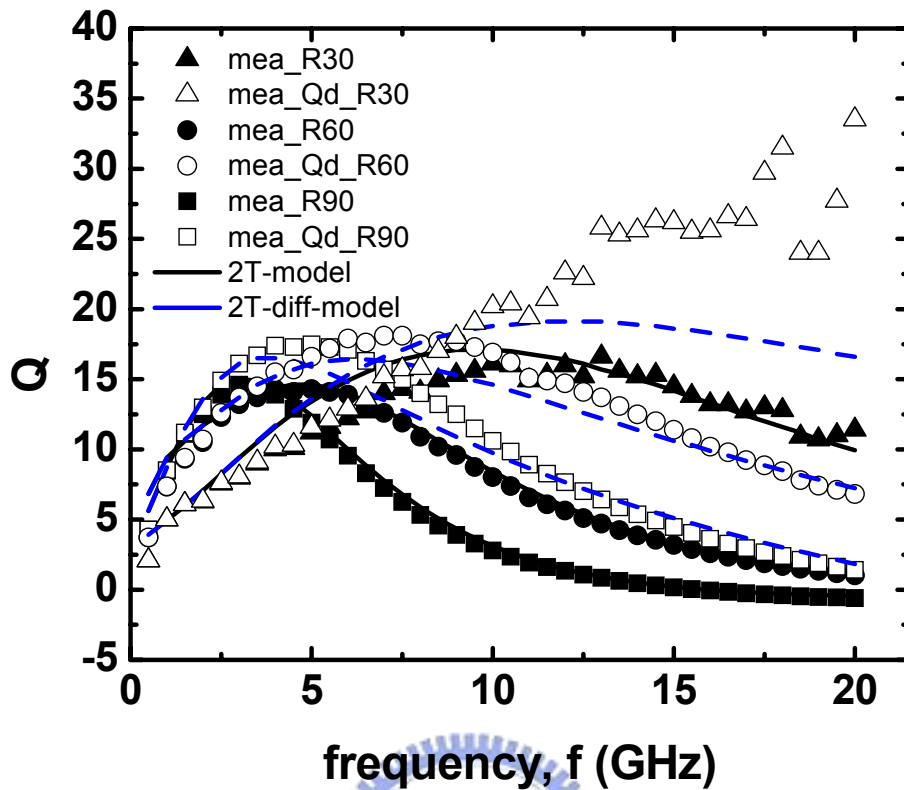


Figure 4.11. Comparison of  $Q(\omega)$  between 2T-model simulation and measurement for fully taper symmetry inductor with various radii:  $R=30, 60, 90 \mu\text{m}$

### 4.2.3 Model Scalability

Besides the broadband accuracy, another important feature realized by this 2T model is the good scalability w.r.t. geometry for all model parameters. Figure 4.44 and figure 4.45 present good match with a linear function of inner radius ( $R$ ) for each model parameter in the symmetric spiral coils' RLC network. Figure 4.46 reveal good fit with a linear function of  $R$  for substrate network involved model parameters,  $C_{\text{sub}}$ ,  $1/R_{\text{sub}}$ ,  $L_{\text{sub}}$ , and  $R_{\text{loss}}$ . The promisingly good scalability proven for full set model parameters suggests that this 2T model is useful in simulation for inductor layout optimization and design. The nature of easy link with standard circuit simulator makes

this 2T model useful in circuit element tuning and optimization for RF circuit design. It has emphasized the need for a powerful symmetry inductor to satisfy current circuit design trends. The development of an accurate and scalable equivalent circuit model for the symmetrical inductors named as 2T model has been demonstrated. The accuracy and continuity of both symmetrical inductance and quality factor for this scalable inductor model is closely examined and satisfyingly good agreement between the simulated and measured device characteristics has been realized. This 2T model can facilitate RF circuit design such as VCO, LNA, and mixer of differential circuit topology in which symmetric inductor become the key passive element to be adopted.

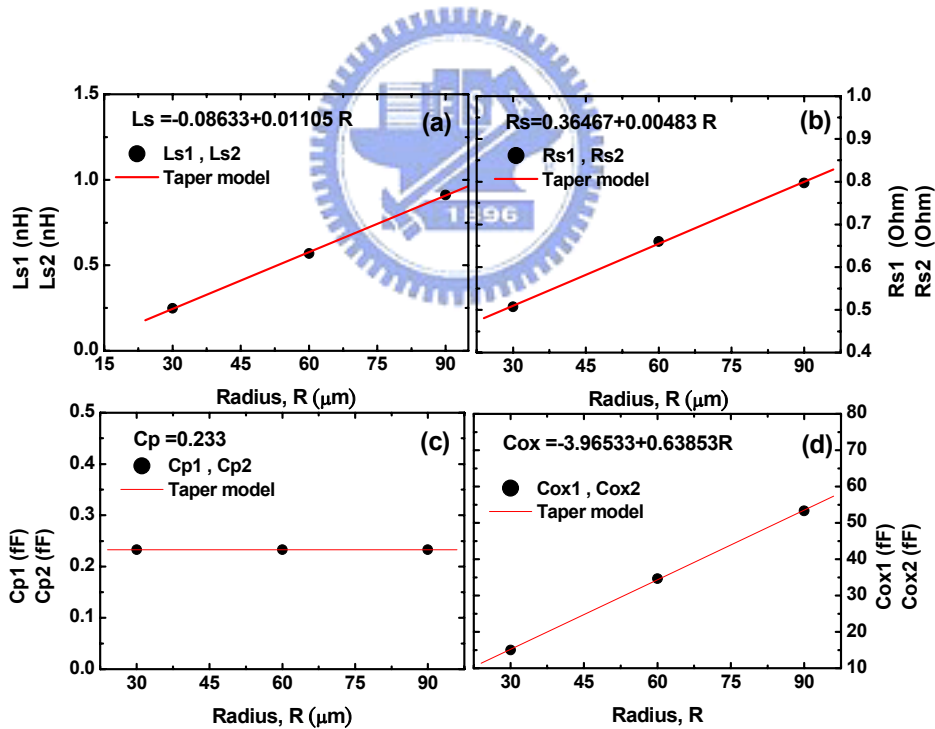


Figure 4.12. 2T-model RLC network parameters versus inner radius, fully taper symmetry coil's RLC network parameters (a)  $L_{s1,2}$  (b)  $R_{s1,2}$  (c)  $C_{p1,2}$  (d)  $C_{ox1,2,3}$

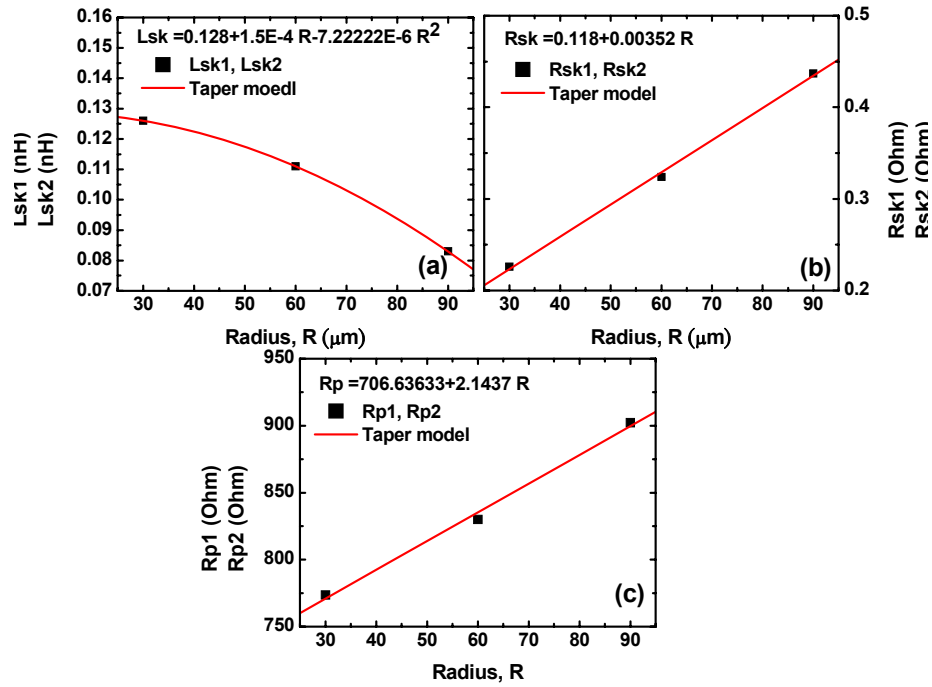


Figure 4.13. 2T-model RLC network parameters versus inner radius, fully taper symmetry coil's RLC network parameters (a)  $L_{sk1,2}$  (b)  $R_{sk1,2}$  (c)  $R_{p1,2}$

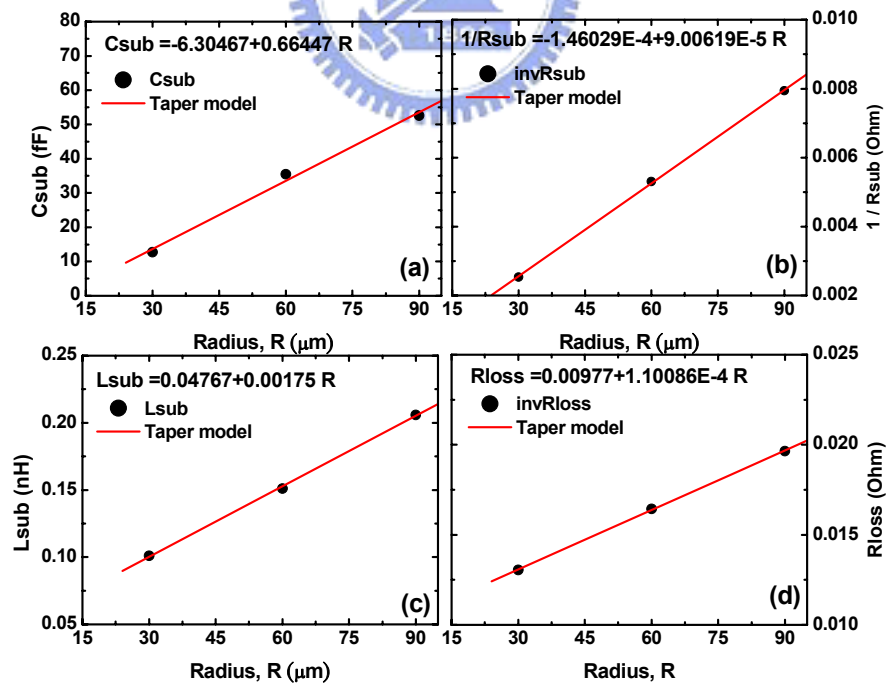


Figure 4.14. 2T-model RLC network parameters versus inner radius, lossy substrate RLC network parameters (a)  $C_{sub}$  (b)  $1/R_{sub}$  (c)  $L_{sub}$  (d)  $R_{loss}$

# Chapter 5

## Future work

Simple T-model and 2T model of broadband accuracy for spiral inductors and fully symmetric inductors on a silicon substrate have been presented. The proposed model containing a combination of RLC networks has been developed to accurately simulate on-chip inductors operating up to 20 GHz. Verification with measurement data from various structures has validated the proposed models. Our models show excellent agreement with measured data over the entire frequency range of interest. All model parameters are validated with good scalability with varying inductor geometries.

Moreover, substrate effect pertaining to on-chip is an important issue of major concern. Through EM simulation by Ansoft HFSS, they demonstrate that energy dissipation, which degrades Q, occurs predominately in the bulk silicon substrates of semiconducting property. Regarding the substrate effect, all model parameters manifest themselves the physical property associated with varying substrate resistivities. As a result, physics-based model parameters enable the developed models applicable for three operation modes (eddy current, slow wave, and TEM modes) under varying substrate resistivities.

In our research work, we design a new inductor structure, which can effectively reduce substrate parasitic effect through differentially driven operation. We name this new structure a fully taper symmetric inductor. A new de-embedding method has been developed accordingly to fit the new inductor structure of fully symmetric feature. We find that a symmetric inductor which is excited differentially can realize a substantial improvement in both Q factor and component bandwidth. Differentially excited

inductors can effectively reduce substrate parasitics that was demonstrated through both simulation and measurement. This leads to higher Q factor than for a single-end excitation when fabricated in silicon technology. This improvement in Q factor can translate directly into lower phase noise and greater output signal swing for the oscillator, especially for the higher frequencies applications. In addition, the proposed and fabricated new symmetric inductor can ensure port-1 equal to port-2. Then, it will help to improve the RF circuit performance considerably such as power consumption. A comprehensive extraction flow has been established through equivalent circuit analysis to enable automatic model parameter extraction and optimization. Moreover, our model can be easily implemented in SPICE-compatible simulator to improve accuracy in circuit simulation.

The future work emerging through this study can be summarized as follows. The first part is the implementation of T-model and 2T-model in Spice compatible circuit simulators to verify model accuracy in the design of RF circuits such as VCO, LNA, and mixer, etc. The second one is the further investigation of substrate resistivity effect subject to different inductor geometries such as metal strip width and space, coil radius, coil number, and coil shape, etc. Moreover, simple spiral of single coil set and symmetric inductor of two spiral coil sets will be covered. The third part is the extension of 2-port de-embedding method for spiral and symmetric inductors to 3-port de-embedding method for differential inductors or transformers. The last one is the extension of 2T model from application in fully symmetric inductor to that appropriate for stack symmetric inductors of elevated broadband and quality factor (higher  $f_{SR}$  and Q).

# References

- [1] C. P. Yue and S. S. Wong, "Physical modeling of spiral inductors on silicon," IEEE Trans. Electron Devices, vol. 47, no. 4, pp. 560-568, Apr. 2000.
- [2] M. Park, S. Lee, C. S. Kim, H. K. Yu, and K.S. Nam, "The detailed analysis of high Q CMOS-compatible microwave spiral inductors in silicon technology," IEEE Trans. Electron Devices, vol. 45, no. 10, pp. 1953-1959, Oct. 1998.
- [3] P. Arcioni, R. Castello, G. D. Astis, E. Sacchi, and F. S. Svelto, "Measurement and modeling of Si integrated inductors," IEEE Trans. Instrum. Meas., vol. 47, no. 11, pp. 1372-1378, Nov. 1998.
- [4] Y. Cao, R. A. Grove, X. Huang, N. D. Zamdmer, J.O. Plouchart, R. A. Wachnik, T.-J. King, and C. Hu, "Frequency-independent equivalent circuit model for on-chip spiral inductors," IEEE J. Solid-State Circuits, vol. 38, no. 5, pp. 419-426, May 2003.
- [5] M. Fujishima and J. Kino, "Accurate subcircuit model of an on-chip inductor with a new substrate network," in VLSI Symp. Tech. Dig., 2004, pp. 376-379.
- [6] J. Gil and H. Shin, "A simple wide-band on-chip inductor model for silicon-based RF ICs," IEEE Trans. Microw. Theory Techn., vol. 51, no. 12, pp. 2023-2028, Dec. 2003.
- [7] T. S. Horng, J. K. Jau, C. H. Huang, and F. Y. Han, "Synthesis of a super broadband model for on-chip spiral inductors," in IEEE RFIC Symp. Dig., 2004, pp. 453-456.
- [8] A. M. Niknejad and R. G. Meyer, "Analysis of eddy current losses over conductive substrate with applications to monolithic inductors and transformers," IEEE Trans. Microw. Theory Techn., vol. 49, no. 1, pp. 166-176, Jan. 2001.
- [9] A. Sutono, D. Heom Y.-J. E. Chen, and J. Laskar, "High-Q LTCC-based passive



- library for wireless system-on-package (SOP) module development, "IEEE Trans. Microw. Theory Techn., vol. 49, no.10, pp.1715-1724, Oct. 2001.
- [10] A. Sutono, D. Heo, E. Chen, K. Lim, and J. Laskar, "Compact implementation of component library in LTCC technology and its application to CMOS RF power amplifier design," in Proc. IEEE Conf. Electr. Perf. Electron. Packag., Oct. 23-25, 2000, pp. 288-291.
- [11] T. Kamgaing, T. Myers, M. Petras, and M. Miller, "Modeling of frequency dependent losses in two-port and three-port inductors on silicon," in IEEE MTT-S Int. Microw. Symp. Dig., 2002, pp. 153-156.
- [12] J.C. Guo and T. Y. Tan, "A broadband and scalable model for on-chip inductor incorporating substrate and conductor loss effects "IEEE Trans. Electron Devices, vol. 53, no. 3, pp.413-421, Mar.2006.
- [13] J.C. Guo and T. Y. Tan, "A broadband and scalable model for on-chip Inductor incorporating substrate and conductor loss effects," in IEEE RFIC Symp. Jun., 2005, pp. 486-489.
- [14] J.C. Guo and T. Y. Tan, "A broadband and scalable model for on-chip inductor appropriate for operation modes of varying substrate resistivities, " in IEEE RFIC Symp. Jun., 2006, pp. 486 - 489.